Alma Mater Studiorum - Università di Bologna

SCHOOL OF SCIENCE

Department of Industrial Chemistry "Toso Montanari"

Master Degree in

Industrial Chemistry

Class LM-71- Science and Technologies in Industrial Chemistry

Surface dynamic of copper nitroprusside as a cathode material: observation by XPS and SEM

CANDIDATE

Elisa Musella

SUPERVISOR

Illustrious Professor Marco Giorgetti

CO - SUPERVISOR

Illustrious Professor Reinhard Denecke

Second Session

Academic Year 2016-2017

ABSTRACT

Nowadays, rechargeable Li-ion batteries play an important role in portable consumer devices. The formation of surface films on electrodes in contact with non-aqueous electrolytes in lithium-ion batteries has a deep impact on battery performance. A basic understanding of such films is necessary for the improvement of power sources.

The surface chemistry and morphology of a cathode material, copper nitroprusside, have here been evaluated by X-ray Photoelectron Spectroscopy (XPS) and Scanning Electron Microscopy (SEM), and placed in relation to the performance of the electrodes.

Interface formation between the cathode and carbonate-based electrolytes has been followed and characterised. The variables have been: number of charge/discharge cycles and air contact. The species precipitating on the surface of the cathodes at ambient temperature have been determined to comprise a mixture of organic and inorganic compounds: LiF, Li_xPF_y, $Li_xPO_yF_z$, inorganic and organic carbonates.

Moreover a problematic due to UHV and X-ray exposure has been followed.

AKNOWLEDGEMENTS

I wish to express my gratitude for Prof. Giorgetti, my Italian supervisor. This thesis would not have been realised without his encouragement and support, and without him giving me the chance to go to Germany.

I also would like to thank Prof. Denecke for his generosity and kindness and his linguistic and scientific feedback throughout this work, and above all for welcoming me in his research group.

I wish to thank all my co-workers at the Wilhelm-Ostwald-Institut für Physikalische und Theoretische Chemie for many fruitful discussions and friendly atmosphere.

I would like also to thank Angelo Mullaliu for sharing and understanding my scientific and personal dilemmas during this thesis period; it has been invaluable to me.

I must also express my profound gratitude to my friends for providing me with unfailing support throughout my life. You stand with me no matter what. This accomplishment would not have been possible without you.

I take also the opportunity to value all the attempts that my boyfriend Leonardo has done during this hard period abroad for making me feel always his first thought and for putting me always back in the right path in discouragement moments.

Last but not the least, I would like to thank my family: my parents and grandparents for supporting me spiritually throughout writing this thesis and my life in general.

INDEX

LIST OF TABLES

LIST OF FIGURES

LIST OF SPECTRA

CHAPTER 1: INTRODUCTION

1.1 X-ray spectroscopies

Since the discovery of X-rays by Röntgen [1] over 100 years ago in his laboratory in Würzburg, X-rays have provided a non-destructive characterization of a large variety of materials. X-ray methods cover many techniques based on scattering, emission, and absorption properties of the X-ray radiation. [2]

In general, spectroscopic techniques are used in order to gather chemical information about surfaces. As shown in Fig. 1, a beam is incident on the surface and penetrates to some depth within the surface layer. A second beam exits from the sample and ultimately is analysed by a spectrometer. [3]

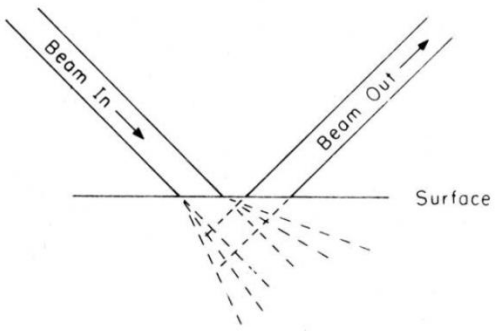

Figure 1: Relationship of probe and analysed beams in surface spectroscopy [3]

By varying the nature of the beams in and out, one can generate a large number of surface analytical techniques as seen in the Table 1. [3] The techniques that are shown in bold are the one used in this work.

When probing a surface with any beam, of course one must be concerned with the effect of the probe beam on the surface:

- Photons are the least destructive: in greater than 95% of the cases no decomposition of the surface occurs.
- Electrons are more destructive and the effect varies from insulator to conductors. Electron beams are particularly destructive for organic materials. In addition to chemical effects, electron beams cause serious sample charging for many insulators.
- Ion beams cause sputtering of all materials. [3]

Table 1: X-rays techniques

	Beam out		
Beam in	Photons	Electrons	Ions
Photons	Infrared spectroscopy Raman spectroscopy X-Ray Fluorescence Extended X-Ray Absorption Fine Structures	**X-Ray Photoelectron Spectroscopy** UV-Photoelectron Spectroscopy Proton-Induced Auger Electrons	Laser Mass Spectrometry
Electrons	Electron Microprobe Appearance-Potential Spectroscopy Catholuminescence	**Auger Electron Spectroscopy** Low-Energy electron Diffraction **Electron Microscopy** Electron-Impact Spectroscopy	Electron-Induced Ion Desorption
Ions	Ion Microprobe: X Rays Ion Induced X-Rays	Ion Neutralization Spectroscopy Ion-Induced Auger Electrons	Secondary-Ion Mass Spectrometry Low-Energy Ion Scattering Spectroscopy High Energy Ion Scattering Spectroscopy Ion-Microprobe: Ions

1.1.1. X ray photoelectron spectroscopy

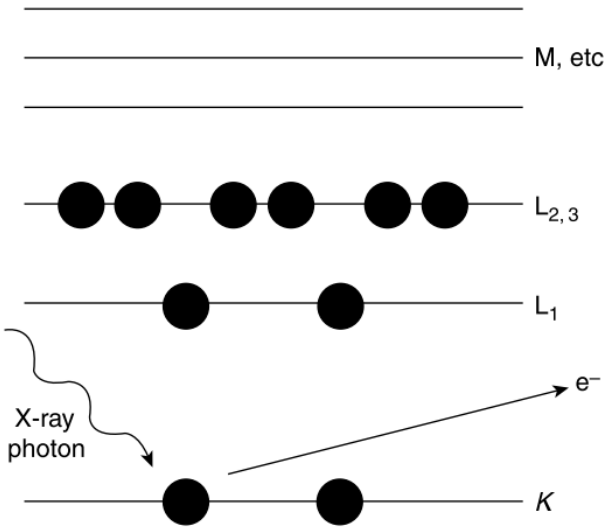

Figure 2: Schematic of x-ray photoelectron spectroscopy process**.** [4]

X-ray photoelectron spectroscopy (XPS) in a non-destructive technique in which incident photons excite the atoms in the samples to produce electrons. [4]

XPS is based on the photoelectric effect when an incident x-ray causes ejection of an electron from an atom. In this process, an incident x-ray photon of energy hν impinges on the atom causing ejection of an electron, usually from a core electron energy level (as

shown in Fig. 2). This primary photoelectron is detected in XPS. For the primary electron, which is bound to the atom with binding energy E_B (for solids referenced to the Fermi energy), to be detected in XPS, the electron must have sufficient kinetic energy to overcome, in addition to E_B, the overall attractive potential of the spectrometer described by its work function Φ_{SP}. Thus, the kinetic energy E_{kin} of this photoelectron is given by:

$$E_{kin} = h\nu - E_B - \Phi_{SP}$$

If the energy of the x-rays and the spectrometer work function are known, the measured kinetic energy can be used to determine the binding energy E_B from:

$$E_B = h\nu - E_{kin} - \Phi_{SP}$$

This E_B is characteristic for each energy level in the element and can be used to determine the element from which the electron originated.

The sensitivity of XPS towards certain elements is dependent on the intrinsic properties of the photoelectron lines observed. The parameter governing the relative intensities of these core-level peaks is the photoionization cross section σ. This parameter describes the relative efficiency of the photoionization process for each core electron as a function of element atomic number.

XPS is a surface-sensitive technique as opposed to bulk techniques because electrons cannot travel without interaction, so the depth from which the electron information is obtained is limited by "the escape depth" of the photo-emitted electrons. [4] Typical escape depth for XPS with the parameters used in this work is 20 Å. [3]

In this sense, XPS can firstly be applied as a simple qualitative tool to establish the presence or absence of elements on a surface. It is sensitive to all elements except H and He. The typical information that we can gather from an XPS measurement are: [5]

- oxidation state
- bounding information

1.1.1.1 Energy losses

As well as the generation of core photoelectron lines in XPS, certain outgoing photoelectrons undergo characteristic energy losses as they are ejected from the atom, ion or molecule. Such well-defined losses should not be confused with the general cascade of inelastic collisions or secondary electrons that occur once an electron has been ejected and give rise to a step-like background, but involve promotion of electrons within the atom to a higher energy level: the consequential loss of kinetic energy by the

photoelectron is observed in the XPS spectrum as a minor peak to the higher binding energy side of the characteristic core level. [6] Such phenomena include shake-up and shake off-satellites.

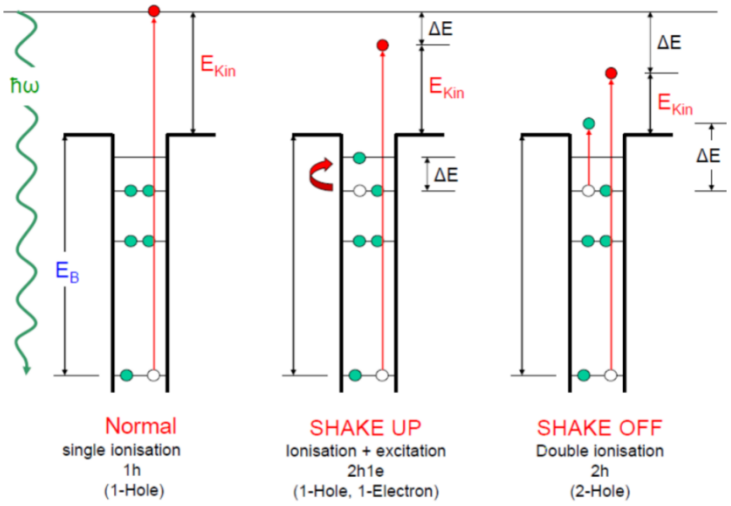

Figure 3: Examples of energy loss phenomena [7]

Figure 3 shows a schematic to describe the processes involved. Shake-up satellites occur when the outgoing electron interacts with a valence electron and promotes it to a higher energy level. The kinetic energy of the core electron is slightly reduced and consequently appears at slightly higher binding energy within the photoelectron spectrum as a characteristic satellite structure. A related occurrence is that of shake-off in which the valence electron is ejected completely from the atom. [6] Another phenomenon that may happen is multiplet splitting. Multiplet splitting of a photoelectron peak may occur in a compound that has unpaired electrons in the valence band and arises from different spin distributions in the electrons of the band structure. This manifests itself as a core line that appears as a multiplet rather than the expected simple core line structure. [6]

1.1.1.2 Quantitative XPS

XPS spectra also bear a relationship between photo-electron intensity and number of atoms sampled. Quantification of these data can be achieved with a precision to within ca 10%. For a homogeneous sample analysed in a fixed geometry, the relationship between XPS intensity and number of atoms is given by:

$$I_A = \int \sigma_A n_a K F_{\hbar\omega} exp^{\left(\frac{-z}{\lambda_A \cos\vartheta}\right)} dz$$

where I_A is the XPS intensity line of the substance A, σ_A is the cross section for excitation of a substance A, n_A is the density of the substance A, K is instrument factor

(comprehensive of acceptance angle, detection sensitivity, transmission function and illuminated area), $F_{\hbar\omega}$ is the photon flux, λ is the mean free path for measured line and ϑ is the emission angle. [7]

1.1.2. Auger Spectroscopy

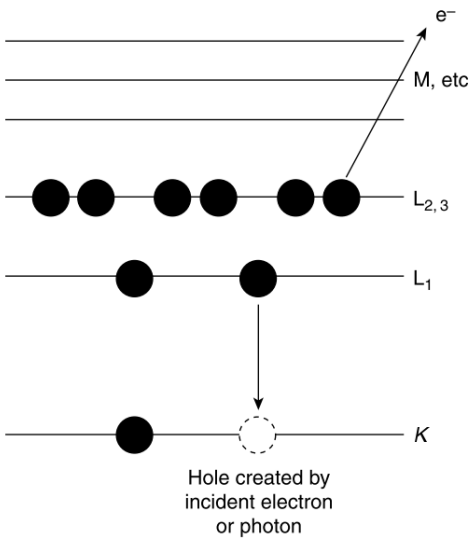

Figure 4: Schematic of the Auger electron emission process induced by creation of a K-level electron hole. [4]

An Auger electron spectroscopy (AES) spectrum is always recorded while measuring with XPS. AES is also based on an electron ejection process like XPS, but the electrons that are monitored in AES are secondary electrons. The secondary electrons called Auger electrons arise from a process shown schematically in Figure 4. The process occurs after primary electron emission when such a core-level hole exists. Incident electrons are usually used in AES to stimulate primary electron emission, although incident x-rays can also be used as in XPS. The presence of this core-level electron hole results in electron relaxation from an outer core level or a valence level to fill the core-level hole. When this relaxation occurs, the excess energy that is released stimulates ejection of a secondary or Auger electron from another core or valence electron energy level. The final state of the atom after Auger electron emission is thus doubly ionized; however this final doubly ionized state is more stable than the initial singly ionized state. The energy of the Auger electron is independent of the energy of the incident electron beam (or photon energy) and depends only on the energies of the three electron levels involved in the process. The kinetic energy of the Auger electron is given by the difference in energy between the primarily ionized core level and the level from which the electron comes that fills the

core-level vacancy minus the energy that it takes to remove the Auger electron from the singly ionized atom and the spectrometer work function Φ_{SP}. The Auger transition is identified by a three-letter label in which the first letter indicates the core level in which the initial electron vacancy resides, the second letter represents the electron level from which the electron comes that fills the initial vacancy, and the third letter indicates the electron level from which the ejected Auger electron comes. Thus, for a KLL Auger electron

$$E_{kin\_KL(1)L(2,3)} = E_k - E_{L(1)} - E^*_{L(2,3)} - \Phi_{SP}$$

where $E_{kin\_KL(1)L(2,3)}$ is the kinetic energy of the Auger electron, E_k is the energy of the K core level, $E_{L(1)}$ is the energy of the electron level from which the electron comes to fill the K-level core vacancy, and $E^*_{L(2,3)}$ is the binding energy of the $L_{(2,3)}$ level in the presence of a hole in the $L_{(1)}$ level. Any three subshells within an atom can be involved in the Auger process as long as the final state is significantly more stable than the initial state. [4]

1.1.3. SEM – Scanning electron microscopy

SEM is the most common and well-known electron microscopy method for imaging of surfaces. This technique is based on the interaction of a primary beam of electrons with energy typically in the range of 0.5–40 keV with a surface. This primary electron beam is first demagnified by a condenser lens and then focused onto the sample surface using a series of objective lenses. SEM must be done in vacuum so that the electrons can travel for distances required. Modern SEMs can achieve a lateral resolution of 1.5 nm at a primary electron voltage of only 1.5 keV. [4] In most SEM analyses, secondary electrons created near the position of the impinging primary beam are detected. However, surface images can also be obtained through collection of backscattered primary electrons.

SEM can also be used to obtain spectroscopic information by using the photons resulting from relaxation processes (in this case the relaxation process is fluorescence).

Wavelength dispersive x-ray analysis (WDX) is used in high-energy resolution instruments. EDS (Energy dispersive x-ray analysis) or WDX are based on the emission of x-rays with energies characteristic of the atom from which they originate in line of electron emission. Thus, these techniques can be used to provide elemental information about the sample. In the SEM, this process is stimulated by the incident primary beam of electrons. This process is also the basis of essentially the same technique but with higher

beam current and performed in a dedicated x-ray spectrometer for bulk analysis, known as electron microprobe analysis (EMA). SEM/EDS typically occurs in a volume of sample larger than that from which backscattered electrons are observed. Thus, SEM/EDS samples the surface to a greater depth than does SEM imaging. Signals typically result from the upper several microns of the near-surface region. Therefore, this technique, similar to electron probe micro analysis (EMA), is a bulk analysis rather than a surface analysis technique. [4]

1.2 Batteries

Development of novel and advanced rechargeable Li-ion batteries is one of the most important challenges of modern electrochemistry. [8] A battery is a device that converts chemical into electrical energy. A battery is composed of several electrochemical cells that are connected in series and/or in parallel in order to provide a certain voltage and capacity. The cell consists of a positive and a negative electrode separated by an electrolyte solution containing dissociated salts, which help ion transfer between the cathode and the anode. Once these electrodes are connected externally, the chemical reactions proceed at both electrodes, thereby liberating electrons and enabling the current to be tapped by the user. Among the various existing technologies (Fig. 5), Li-based batteries - because of their high energy density and design flexibility - currently outperform other systems, accounting for 63% of worldwide sales values in portable batteries. [9]

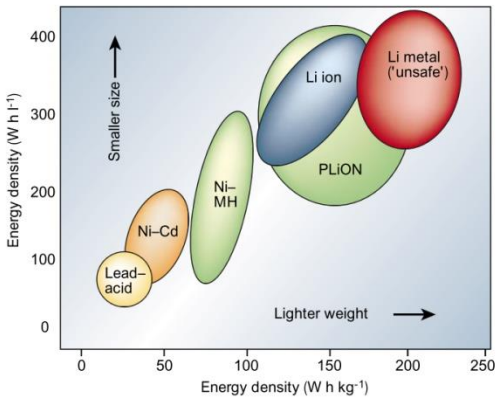

Figure 5: Comparison of the different battery technologies in terms of volumetric and gravimetric energy density.

1.1.1. Lithium Ion Batteries

Lithium cells are made of lithium metal as negative electrode, an active material as positive electrode, and a non-aqueous lithium-ion containing solution which helps ion transfer between the electrodes: the electrode material should undergo a reversible reaction with lithium ions, typically it is reduced during discharge, while oxidized in charge:

$$xLi^{+} + AM\ (s) + xe^{-} \underset{\text{charge}}{\overset{\text{discharge}}{\rightleftarrows}} LixAM\ (s)$$

Active material electrodes may have a porous framework that allows the rapid insertion and extraction of lithium ions with generally little lattice strain. Otherwise, a different lithium ion source may be adopted, since the usage of lithium metal can be dangerous. LixAM' can be opted for negative electrode, whereas the active material acts as a lithium ion sink, in a way that Li-ions are intercalated in both electrodes:

$$xLi^{+} + AM\ (s) + xe^{-} \underset{\text{charge}}{\overset{\text{discharge}}{\rightleftarrows}} LixAM\ (s)$$

This strategy is known as rocking chair philosophy [10] (Fig. 6), and was the first attempt to overcome the safety hazards related to Li, as an un-even growth upon Li metal takes place during alternated cycles of discharge/charge. Using two insertion hosts rather than one erase safety, even though a more positive cathode has to be found since the anode has a less negative potential [9].

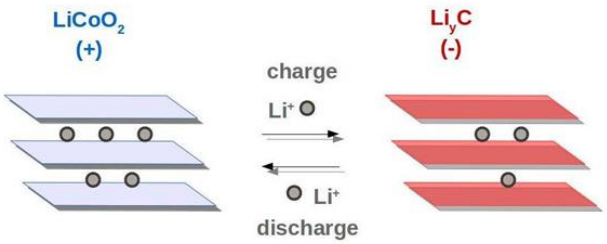

Figure 6: Schematic representation of a rocking chair cell

Commercial swing batteries consist of graphitic carbon as negative electrode and lithium cobalt dioxide as cathode. During discharge lithium is reversibly intercalated in the host material and electrons flow in the external circuit to balance the reaction. During charge the non-aqueous electrolyte mediate the transfer of Li-ions in the opposite direction [9].

The other key component of a battery is the electrolyte, which commonly is referred to a solution comprising the salts and solvents. The choice of the electrolyte is crucial, and it is based on criteria that differ depending on whether we are dealing with polymer or liquid-based Li-ion rechargeable batteries. [11]

There are a great number liquid solvents available, with different dielectric constants and viscosity, and it is possible to select specific solvents to favour the ionic conductivity. However, there are only a few Li-based salts or polymers to choose from. [9]

The most common salt used for Li-ion battery is $LiPF_6$. It is usually employed for its ionic conductivity, but it is thermally unstable, decomposing in LiF and PF_5 and generating HF if water is present.

$$P F_6^- \leftrightarrows P F_5 + F^-$$

In terms of cyclability, this means that the battery performance would decline.

The other option might be lithium imide salts, for instance lithium bis(triflouromethane sulfonyl) imide salt, denoted as LiTFSI, which is safer and more stable than $LiPF_6$. $LiPF_6$ has a higher conductivity and even a greater viscosity compared to LiTFSI, due to the PF_6^- anion coordination by solvent molecules. However, under the same conditions, the performances result better for LiTFSI than for $LiPF_6$ [12].

Concerning the liquid solvents, ethylene carbonate (EC) is usually present as solvent in the Li-ion solution, as it forms an electron insulating yet stable ion-conducting layer on the anode, which avoids degradation. This film is called solid electrode interface (SEI) and it is responsible for the stability of Li-ion batteries [9]. However, EC cannot be used alone, as it is solid at room temperature. It is commonly mixed with propylene carbonate (PC) and/or dimethyl carbonate (DMC), the former not compatible with graphitic compounds causing exfoliation (if SEI has not been formed yet) [13], the latter melting at 2°C, so not used alone as well in low temperature applications. Mixing EC with other carbonates makes not only the solvent mixture liquid, but optimal viscosity and ion-conductivity are also achieved.

Carbonates are considered optimal solvents for Li-ion batteries, since they are available at an affordable price, and can dissolve Li-salts enough to achieve a good conductivity,

although the electrolyte concentration should not overcome the value of 1-2 mol/L for viscosity issues. [14]

As far as concern electrochemical cells, interfaces play an important role: the electrode/electrolyte interface may be responsible for a poor cycling, as side reactions may occur.

By far, the most common active material used in the negative electrodes is graphite ($C_6 + xLi^+ + xe^- \leftrightarrows C_6Lix$). However, there are a variety of other kinds of carbons which have also been used. As positive electrode mostly transition metal oxides and phosphates have been employed, out of which $LiCoO_2$, $LiMn_2O_4$, and $LiFePO_4$ are the most common ones. [15]

During first charge of the Li-ion battery the electrolyte undergoes reduction at the negatively polarized graphite surface. This forms a passive layer comprising of inorganic and organic electrolyte decomposition products as shown in Fig 7. In an ideal case this layer prevents further electrolyte degradation by blocking the electron transport through it while concomitantly allowing Li-ions to pass through during cycling. This essential passive layer has been named solid electrolyte interphase (SEI) [16]. Some solvents such as cyclic alkyl carbonates form effective passive layers that ensure good cycling stability of the negative electrodes. [15]

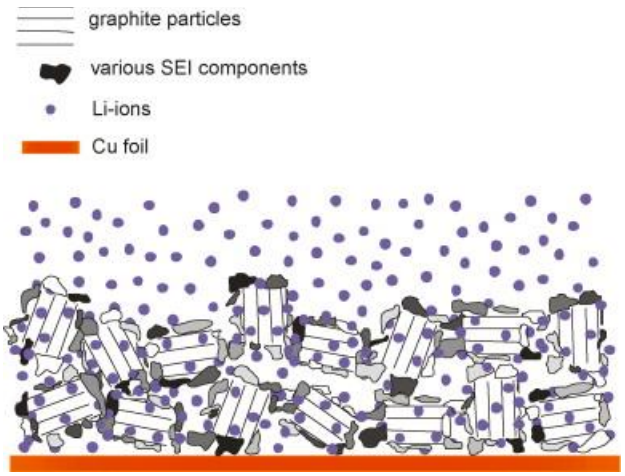

Figure 7: Sketch of a lithiated graphite composite electrode covered by inhomogeneous SEI. The SEI components shown in darker shades of grey are mainly inorganic while those shown in lighter shades of grey are organic.

All parameter and property of the SEI deeply affects battery performance. The composition, thickness, morphology, and compactness are a only some examples. Irreversible charge “loss” (ICL) in the very first cycle occurs due to solvent reduction and SEI formation and is hence a characteristic of SEI [17]. Damaging processes

occurring during storage (self-discharge) also depend on the ability of the SEI to passivate active material surface. [15] Hence, the life of a battery also depends on SEI [18]. SEI may also dissolve and/or evolve during cycling. Thus, effective and stable SEI is mandatory for good cycling life of the battery [19]. It becomes even more important during cycling at high rates and at deeper depth of discharge [20]. However the most important consequence of SEI is on the safety of the battery [21].

Some interface phenomena is occurring also on the cathode side of the cell, even though the validity of the SEI-layer concept is still somewhat tenuous in this "cathode" context. The implication is that Li^+ ions must also travel through an additional (solid electrolyte interphase (SEI)-type) layer between cathode and electrolyte – a process which could even prove rate-limiting if the surface species so formed were poor ion-conductors and Li^+-ion diffusion through the electrolyte and bulk electrode material were fast [22].

1.3 Blue Prussian Analogues

Transition metal hexacyanoferrates of the general formula $A_hM_k[Fe(CN)_6]_l \cdot H_2O$, in which:

- h, k, l, m are stoichiometric numbers,
- A is the alkali metal cation,
- M is transition metal ion,

represent an important class of mixed-valence compounds, of which Prussian blue or iron(III) hexacyanoferrate(II) (with A = K and M = Fe in the above generic formula) is the classical prototype. [23]

Prussian Blue is a ferric ferrocyanide with the formula $Fe^{III}_4[Fe^{II}(CN)_6]_3$ with iron(III) atom coordinated to nitrogen and iron(II) atom coordinated to carbon. [24] It was originally named Berliner blau and it was accidentally synthesized for the first time in 1704 by Heinrinch Diesbach and had applications not only as blue pigment and replacer of the much more expensive lapis lazuli, but also as antidote. It actually consists of an open-framework structure, which was useful for trapping irreversibly thallium (I) ion, which could replace the interstitial potassium ion deriving from the reactants [25]. This feature, known as ion exchange, is nowadays used for trapping caesium-137 from waste streams in the processing of nuclear fuels [23].

Prussian blue presents two different form: soluble and insoluble. This distinction is not referring to a real solubility, instead to a tendency to form a colloidal solution or not, due respectively to the absence or presence of vacancies and interstitial cavities. [23]

Prussian blue analogues (PBAs) are bimetallic cyanides with a three-dimensional lattice of repeating units of -NC-Fe-CN-M-NC-, where M denotes a transition metal, generally Mn, Co, Ni, Cu, Zn [25]. As iron is commonly present, these compounds are recognised as hexacyano ferrates, otherwise in case of absence of iron, they are just called hexacyano metallates. Many works have been written about PBAs, for instance regarding electrochemical detection of hydrogen peroxide. [26]

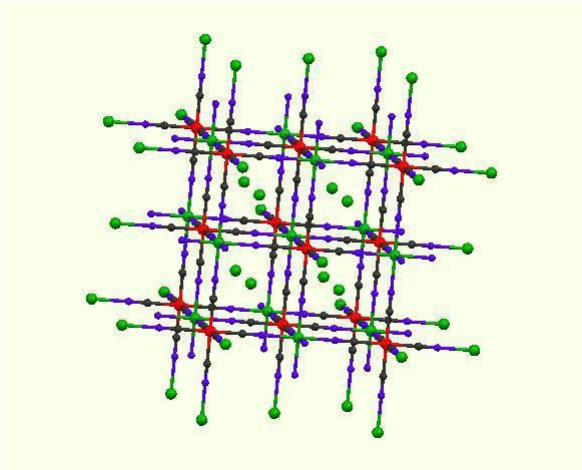

Figure 8: Structure of a metal hexacyano-ferrate

The cyano ligand is like a bridge between Fe and M, linking them in a precise way, the carbon bound to Fe, while the nitrogen to M (Fig.8) , whereas M is a divalent ion. Moreover, iron is usually present as Fe (III) in a low-spin state due to the strong-field ligands. A change in the M oxidation state from (+2) to (+3) provokes a contraction in the cell dimensions and it is compensated by interstitial ions [23]. Both Fe and M can be the redox centers, in a way that the overall capacity should be higher than electrodes with just one metal that can act as centers for a redox reaction. [27]

Through the three-dimensional lattice, Prussian blue analogues are also known for the flexibility due to the stretching of cyano ligands, which have the function of mediating a metal-to-metal charge transfer as well [28]. The C-end has the possibility to remove charge through a π-backbonding, and to place it on the N-end, making possible the

interaction between the generally 5 Å distant metals, and giving rise in this way to magnetic and optical properties [29].

Among PBAs properties, also electrochromism is encountered: $Co[Fe(CN)_6]$ can change its colour by gaining or loosing electrons, being violet in its oxidized state, while green in the reduced form. Furthermore, the colour of cobalt hexacyanoferrate is attributed not only to the oxidation state of Co, but also to its environment: different cations or presence of water alter its aspect [23].

Regarding the porous structure, the open framework is given by repeated vacancies of the octahedral building unit $[M(CN)_6]$. In these cavities both coordinated and weakly bonded water is present, which can be removed below 100°C without modifying the existing structure [29]. Additionally, these compounds can host both Li- ions due to the large interstices and channels, being so processed for battery use [30].

1.3.1 Copper nitroprusside

Copper ferricyanide $Cu[Fe(CN)_6]$ is a a Prussian blue analogue where Fe (II) is replaced by Cu(II). Also in this case, two forms are present, one soluble and one insoluble. The former has a face-centered cubic structure: Fe and Cu ions are octahedrally coordinated to –CN and –NC groups, respectively. The latter has a cubic framework, but 1/4 of the $Fe(CN)_6$ are vacant, so that water molecules can replace the empty nitrogen positions in order to complete the coordination of Cu. Thus, Cu atoms are present in this unit cell with three pseudo-square planar coordinated atoms (CuN_4O_2) and one octahedrally coordinated Cu atom (CuN_6), resulting in an average of $CuN_{4.5}O_{1.5}$ [27].

Copper hexacyanoferrate can be synthetized using a co-precipitation method: a Cu(II) and a ferricyanide solution are added at the same time under constant stirring, and the product can be collected by filtration. The synthesis takes place at room temperature.

Copper nitroprusside has a nitrosyl group replacing one of the cyano ligand. The nitrosyl group does not have the possibility to act like a linking brid, so that the resulting structure has a higher porosity. Moreover, there may be three redox centers, as not only copper and iron can change their oxidation state, but also nitrogen in the nitrosyl group. Actually, the nitrosyl group is a non-innocent ligand and may be present in three different forms within the crystal structure: NO^+, $NO\cdot$, NO^-.

Nitrosyl group could theoretically undergo a redox reaction, changing meanwhile its geometry:

$$NO^{+} \xrightarrow{e^-} NO\cdot \xrightarrow{e^-} NO^{-}$$

$$\text{Linear} \rightarrow \text{bent} \rightarrow \text{bent}$$

The resulting battery capacity would be increased due to the number of electroactive species, whereas the geometrical modification could be observed by IR spectroscopy, the linear -NO absorbing around 1940-1950 cm−1, the bent form at 1400-1700 cm−1. [31] [32] [33]

The hypothesis of a bending of nitrosyl group may be assisted by the case of sodium nitroprusside $Na_2[Fe(CN)_5(NO)]_2{\cdot}H_2O$: according to the published works, sodium nitroprusside has been found in two different structures, one having an isonitrosyl, the other one characterized by a bent -NO [34] [35].

In addition, copper nitroprusside could be present either in the hydrated form with two water molecules per unit formula, or anhydrous.

The hydrated structure is orthorhombic. The iron is coordinated to five cyanide ligands and one nitrosyl, the copper is surrounded by four equatorial cyanides and two axial water molecules. The axial -NO and -CN groups do not act as bridge ligands. Moreover, copper shows axial elongation according to bond lengths calculations due to its d9 electronic configuration and Jahn-Teller distortion (Figure 9a).

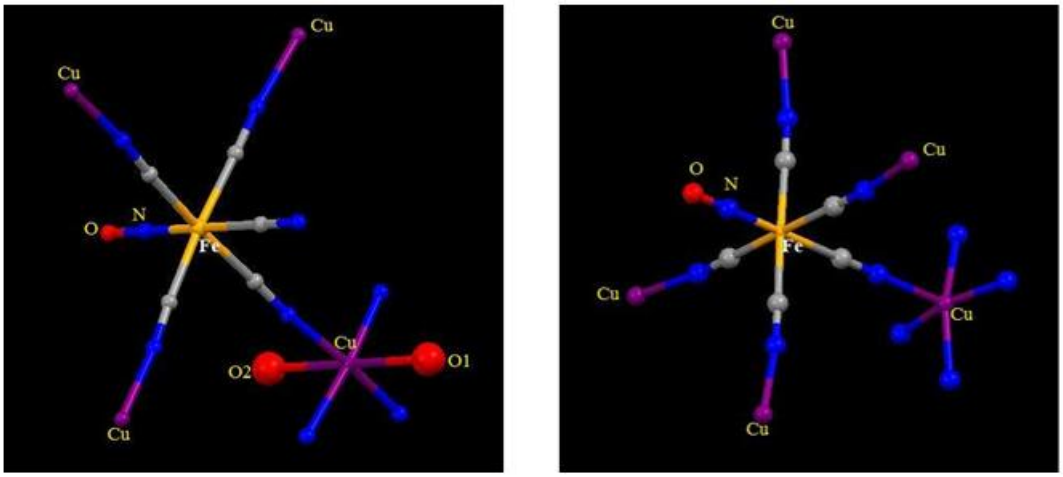

Figure 9: **a)** Structure of $Cu[Fe(CN)_5(NO)]{\cdot}2H_2O$ **b)** Structure of $Cu[Fe(CN)_5(NO)]$

The anhydrous structure is tetragonal. Copper loses two coordination positions because of elimination of water: for this reason the structure changes and copper coordinates not only to four equatorial cyanides, but also to an axial one, so that the coordination sphere resembles to an elongated pyramid of square base [36] (Figure 9b).

In the anhydrous structure the distance between the oxygen-end of nitrosyl and copper ion is reported to be 2.93 Å [36]: according to the model of hard spheres, this spacing corresponds to the Van der Waals interaction distance, the oxygen radius being 1,52 Å and the copper one 1,40 Å. This interspace suggests no chemical bond between oxygen and copper, and therefore that the nitrosyl group does not bridge the two metals. However, the atoms are close enough to allow a polarization of the -NO electron cloud by the copper ion, which results in an increase of the NO π-backdonation towards iron [36].

Copper nitroprusside has been processed as electrochemical sensor [37]; its use as cathode has been probed by the analytical group in a previous thesis. Electrochemical tests were performed both in coin cells and by using in situ cells: on one hand, coin cells allowed different formulations to be easily tested, on the other operando cycling led a deeper insight to insertion process and both chemical and physical changes. Results of several tests highlighted a modification of the material itself over the first cycles up to a stable active compound able to perform several cycles. Moreover, operando techniques report that structural rearrangement of the material takes place in the very first cycle, as well as electrochemical processes. [38]

CHAPTER 2: AIM OF THE WORK

The aim of the work was a better understanding of the surface chemistry of an electrode. For pursuing such purpose, the idea was to investigate the surface through XPS and SEM technique.

Several samples have been prepared and tested electrochemically in a previous work [38]. In the table 2, it is possible to see the complete set of sample analysed in this thesis.

Table 2: Set of sample available

Sample	Sample ID	Notes
Copper nitroprusside	AM1	Powder
Copper nitroprusside	AM4	Powder
Copper nitroprusside	AM1_F	Powder + CB + PTFE + VGCF_H
Copper nitroprusside	AM4_F	Powder + CB + PTFE + VGCF_H
Copper nitroprusside	AM1_E	Pristine – not cycled – only soaked on the electrolyte
Copper nitroprusside	AM4_E	Pristine – not cycled – only soaked on the electrolyte
Copper nitroprusside	AM11	Charged, beginning of the cycling
Copper nitroprusside	AM12	Charged, 180 cycles done
Copper nitroprusside	AM14	Discharged, 143 cycles done
Copper nitroprusside	AM16	Charged, 1000 cycles done
Copper nitroprusside	AM17	Discharged, 3 cycles done
Copper nitroprusside	AM15	Charged, several cycles done
Copper nitroprusside	AM41	Charged, 64 cycles done
Copper nitroprusside	AM47	Discharged, several cycles done
Copper nitroprusside	AM42	Charged, 114 cycles done
Copper nitroprusside	AM43	Discharged, 51 cycles done
Copper nitroprusside	AM44	Charged, 22 cycles done
Copper nitroprusside	AM45	Discharged, beginning of the cycling

Since it has been noticed that a structural rearrangement of the material happens during cycles, there was the interest to follow up the trend of the oxidation states in order to see if a changing on the redox center might cause the observed decrease of capacitance. It has been decided to achieve this kind of knowledge monitoring electrodes in different moments of their life, as shown again in table 2 - notes.

Nevertheless, due to the use of highly energetic photons for excitation of the sample, the risk of radiation damage exists. The highly energetic beam spot may lead to degradation of the SEI (solid electrolyte interphase) components [39] and of the sample itself and may alter their chemical nature. Another problem could also be related to the ambient of

the UHV. In order to have a deep insight on this kind of concerns, it has been settled to run some test on two “reference” samples, in order to validate this hypothesis.

Another important feature that has been possible to investigate is the decomposition of the electrolyte during cycle: the electrolyte was $LiPF_6$ in a mixture of carbonates. In particular it has been noticed that the F 1s peak is really useful for such a purpose.

Depth profiling is also been done in order to gain information on the bulk of the electrode.

SEM/EDS measurements have been recorded in order to gain morphological characteristics and to have a comparison in elemental analysis with XPS.

CHAPTER 3: EXPERIMENTAL PART

3.1 XPS measurement

The XPS measurements were recorded by VG Escalab 220i-XL spectrometer (figure 10) equipped with a model 220 analyser and a set of six channel electron multipliers with a multidetector dead time of 16 ns. An Al K_α (hν=1486.6 eV) radiation from an Aluminium-Magnesium twin anode source was used for all samples, along with pressures in the analysis chamber of 10^{-9}-10^{-8} mbar.

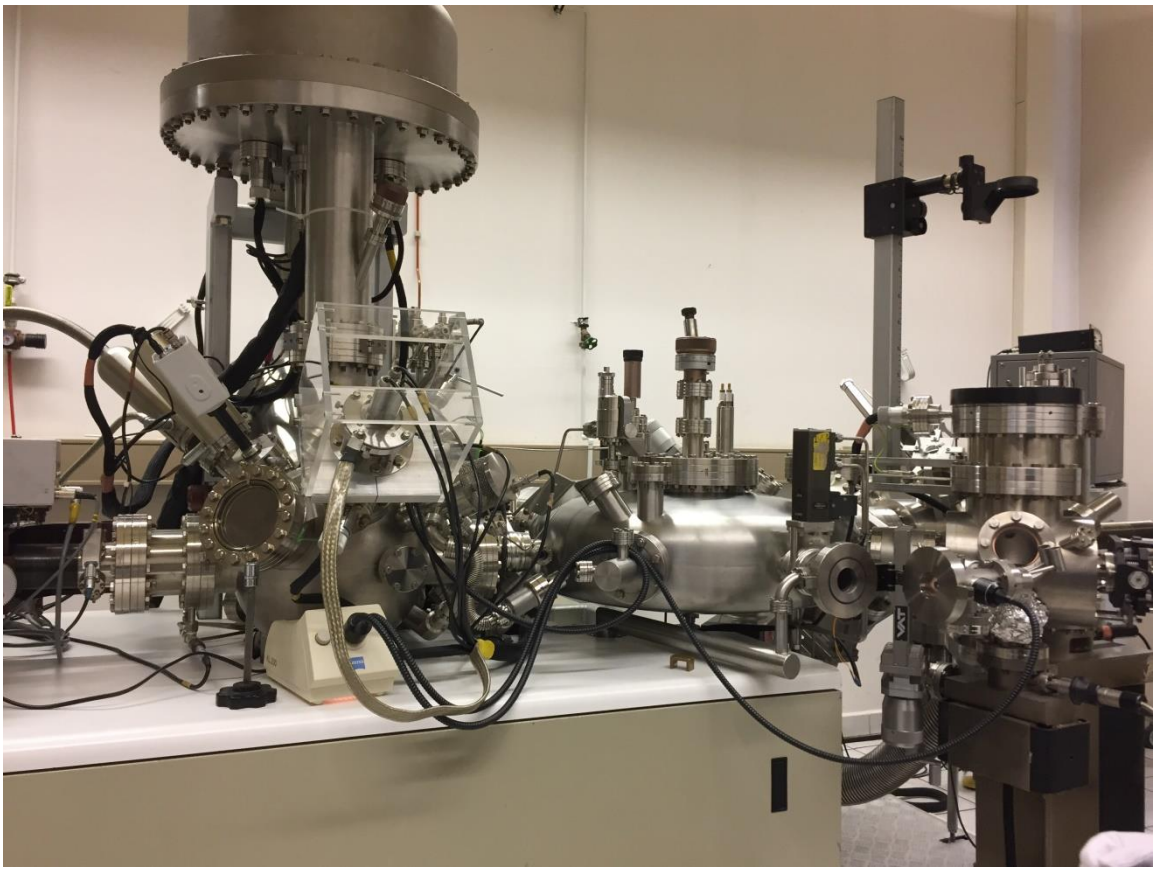

Figure 10: XPS apparatus

Some samples were measured while the Flood Gun was on with the purpose of suppressing differential charging on the samples.

Depth profiling of the sample surface can provide useful information on the morphological features of the surface. This can be achieved by Ar^+-ion etching (sputtering) of the surface, followed by XPS analysis.

In table 3, the acquisition parameters are summarised.

Table 3: Acquisition parameters for XPS measure

Parameters of acquisition	Survey spectra	Detailed spectra
Range	-5 – 1305 eV	Element depending
Pass Energy	50 eV	20 eV
Step width	0.5 eV	0.1 eV
Dwell time	100 ms	300 ms
Scans	1	4-6
Lens Mode	Large area - LAE	Large area – LAE

The spectra were analysed and fitted by UNIFIT 2017 (http://home.uni-leipzig.de/unifit/). A Shirley function has been chosen for the fitting of the background. Line synthesis of detailed spectra were conducted using Gaussian-Lorentzian curve.

3.2 SEM measurement

The morphology and the chemical compositions of the samples are investigated by FE-SEM LEO 1525 ZEISS instrument fitted with an EDS detector, working with an acceleration voltage of 20 kV.

3.3 Sample preparation

The analytical group of University of Bologna supplied a set of cathodes (table 2) removed from lithium ion coin cells.

The synthesis of the active material (copper nitroprusside) was based on a co-precipitation method from 20 mM solutions of $CuSO_4 \cdot 5H_2O$ and $Na_2[Fe(CN)_5(NO)] \cdot 2H_2O$ as discussed in a previous work [38]. The cathodes had the following formulation:

- 70% w/w active material
- 10% w/w PTFE (Teflon)
- 10% w/w CB (Carbon Black)
- 10% w/w VGCF_H (Vapor Grown Carbon Fiber)

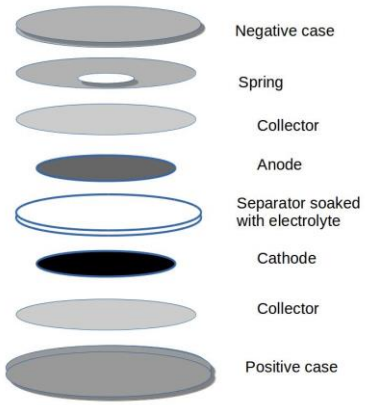

Figure 11: coin cell geometry

The coin cell geometry is shown in figure 11. Lithium metal foil was adopted as anode, $LiPF_6$ 1M in EC:PC:3DMC without additives as electrolyte.

3.4 XPS sample preparation

All the samples, except of AM16, were exposed to air for a period of at least 1 month. This allowing air species such as CO_2, water and similar contaminates the superficies. All the formulated samples were washed with acetone before being fixed on a sample holder with carbon tape as shown in figure 12 and inserted in the XPS machine.

AM16 was treated differently: the coin cell was disassembled in a LABmaster Pro Glove Box and the cathode fixed on the sample holder there and moved to the XPS analyser chamber taking care that no air got in contact with the cathode.

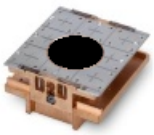

Figure 12: Sample mounted on the sample holder

3.5 SEM sample preparation

All the samples were fixed on a sample holder with carbon tape and inserted in the microscope.

CHAPTER 4: RESULTS AND DISCUSSION

In the following chapter all the results will be presented and explained. Firstly will be introduced how the transmission function was recorded in order to gain a more accurate quantitative analysis. After that a characterisation of the material will be reported. The next step is a deeper insight into the various problematic of the materials such as UHV and X ray stability, decomposition of the electrolyte, air contact modifications and the nitrogen issue.

4.1 Measuring the transmission function of the photoelectron spectrometer

Since all detailed spectra are recorded with 20 eV EP, it was necessary to measure the transmission function in this condition prior to the experiments.

The transmission function *T* of a particular spectrometer and spectrometer setting determines the fraction of photoelectrons from the sample reaching the detector as a function of their kinetic energies. Although *T* is a function only of E_{kin} for older spectrometers equipped with one x-ray anode and without lenses, for new instruments *T* depends on four essential setting parameters:

- Kinetic energy E_{kin} of photoelectrons.
- Pass energy EP.
- Lens mode *L*.
- X-ray source *Q*.

giving *T(E)* → *T(E*, EP, *L*, *Q)*. Therefore any investigation of the transmission function *T* of any spectrometer should account for all the spectrometer settings referred to above.

In order to find the unknown transmission function T of any spectrometer, Smith and Seah, Seah and Cumpson et al. recommend the adaptation of measured survey spectra M(E) for X = Au, Ag or Cu on reference spectra S(E) recorded for the Metrology Spectrometer II with $M_X(E)= T_X(E)\cdot S_X(E)$. The model function consists of seven parameters: $T = a_0+a_1\varepsilon+a_2\varepsilon^2+a_3\varepsilon^3+a_4\varepsilon^4+b_1E^{b2}$, where E is the kinetic energy and $\varepsilon = (E - 1000eV)/1000eV$. In the energy range 200-1500 eV a transmission function $T = a_0+b_1E^{b2}$ was found to give an appropriate approximation. [40]

4.1.1 Procedure

Precautions

- Cu is the reference material that has been chosen
- Polish the sample with first soap and then ultrasonic bath with ethanol
- Insert the sample on XPS
- Survey spectra for detecting C 1s content
- Sputter to get C → 0

Analysis

Detail and survey spectra are measured of a Cu foil with 20 eV pass energy with three different lens modes (LAE, LAX, SAE150). The transmission function of each is detected making a comparison with reference spectra. The other acquisition parameters are summarised in table 4.

Table 4: Acquisition parameter

Parameters of acquisition	Survey spectra	Detailed spectra
Range	-5 – 1305 eV	Element depending
Step width	1 eV	0.1 eV
Dwell time	300 ms	300 ms
Scans	2	3

4.1.2 Large area electronics – LAE

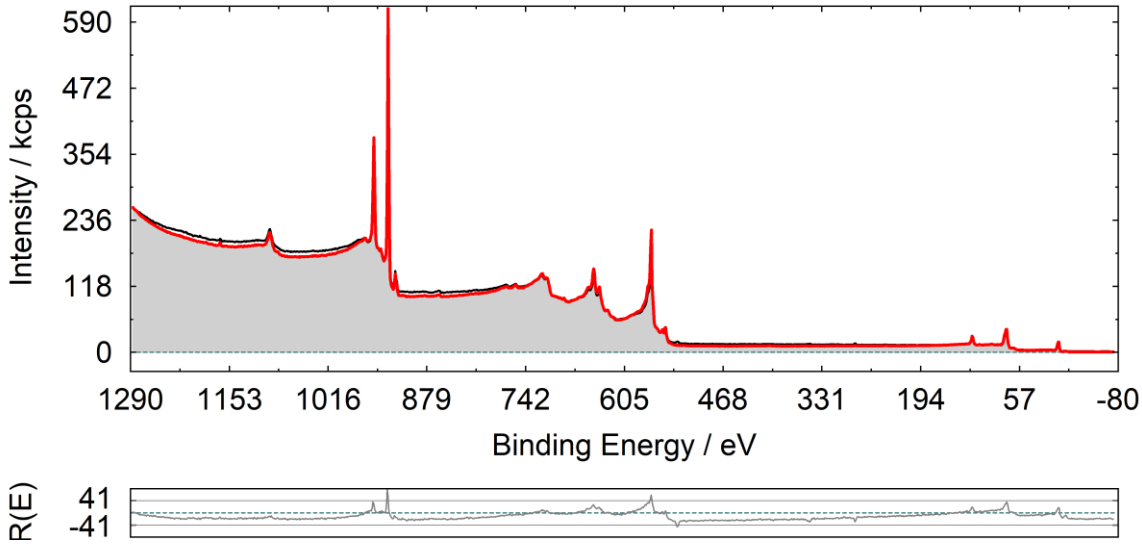

Spectrum 1: Survey Cu foil with LAE lens mode. The red line is the standard spectrum superimposed, the black like in the measured spectrum and the grey part is the area covered.

The survey is fitted with a reference Cu spectrum for comparison. The residuum seems to be quite high, but since a survey spectrum is fitted, it is acceptable.

As mentioned above, the transmission function is described by:

$$T = a_0+a_1\varepsilon+a_2\varepsilon^2+a_3\varepsilon^3+a_4\varepsilon^4+b_1E^{b2}$$

The value obtained for this lens mode are summarised in table 5.

Table 5: Parameter for LAE lens mode

Parameters	Value
$\mathbf{a_0}$	-0.3884
$\mathbf{a_1}$	0
$\mathbf{a_2}$	0
$\mathbf{a_3}$	0
$\mathbf{a_4}$	0
$\mathbf{b_1}$	42.5569
$\mathbf{b_2}$	-0.4955

In order to test the resulting transmission function, a relative quantification of two lines in the calibration sample were performed: Cu 3p (spectrum 2) and 2p (spectrum 3) were then recorded and fitted.

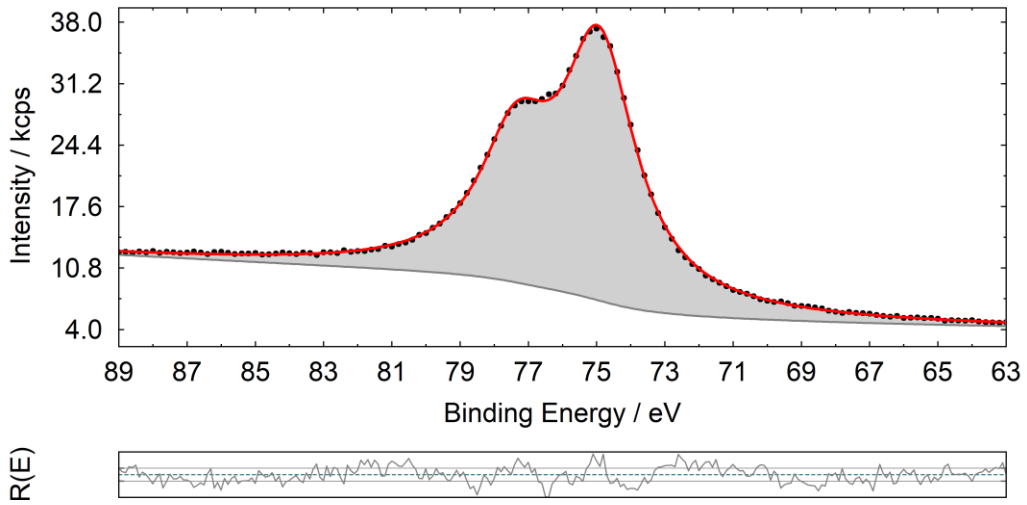

Spectrum 2: fitted Cu 3p signal from Cu foil

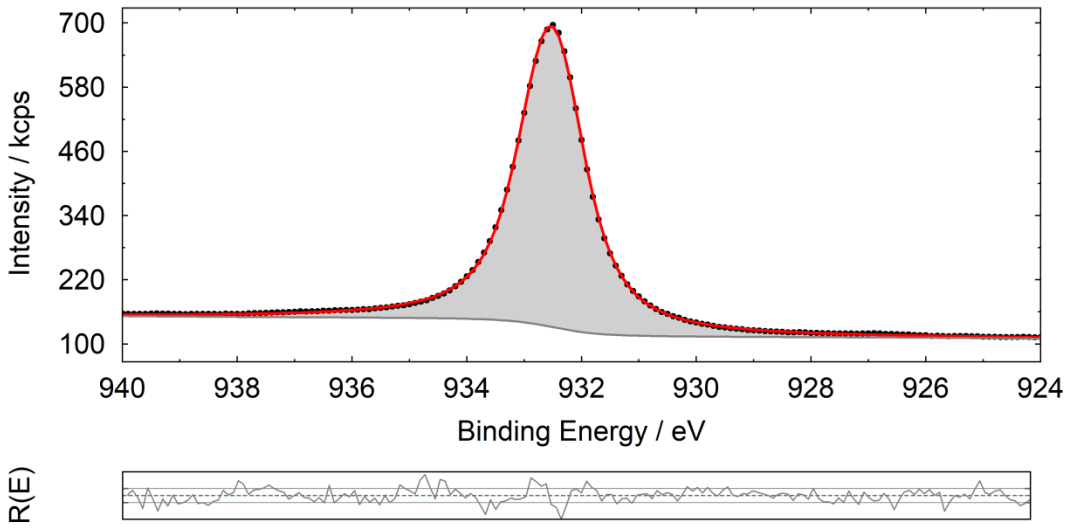

Spectrum 3: fitted Cu 2p3/2 signal from Cu foil

Orbitals 2p and 3p are fully occupied and considering the sensitivity factors, a ratio of 1:1 is expected.

Table 6: Quantification of Cu foil calibration sample for LAE lens mode

Peak name	E_B /eV	Area/cps·eV	Sens. Fact.	Norm. Area	Quant./at.%
Cu 3p Doublet 1	74.92	161212.09	44.337	3636.0624	48.71
Cu2p3/2 Peak 1	932.53	1074704.0	280.74	3828.0707	51.29

It is considered that in XPS an error approximatively between 5-10% occurs. The result shown in table 6 is on limit of confidence. In spectrum 4 it is possible to observe a comparison between the transmission function measured at three different pass energies.

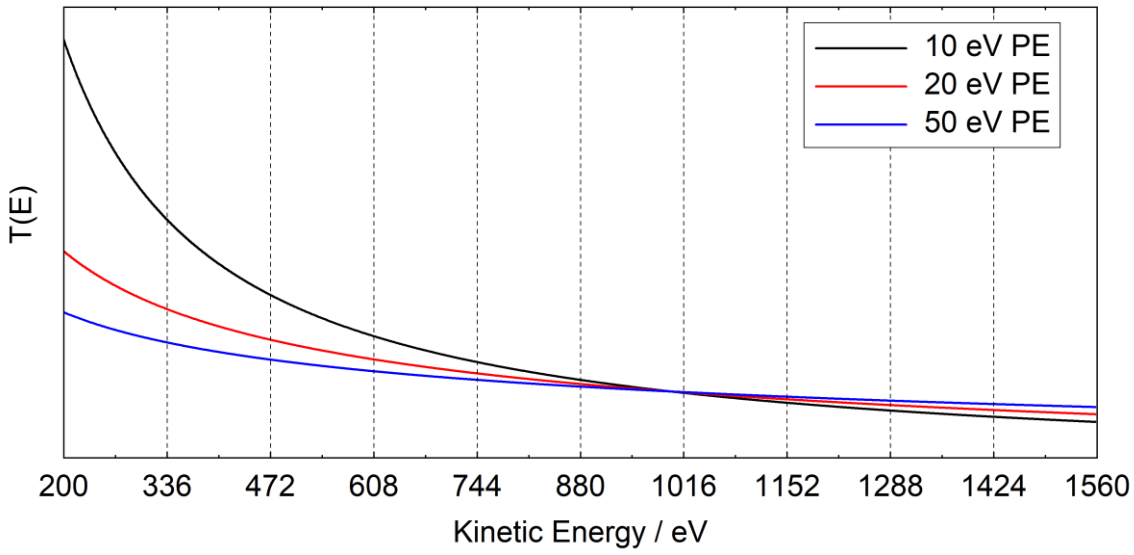

Spectrum 4: plot of transmission function for three different PE. The T(E) is set to 1 at 1000eV.

Definitively, if a transmission function at a PE different than the one that has been used for recording the spectra would have been used for quantification, an error on the quantification would have been committed.

4.1.3 Large area XL electronics – LAX

The procedure, the spectra and the results for LAX lens mode are similar to the ones reported for LAE. In table 7 the parameters of the transmission function $T = a_0+a_1\varepsilon+a_2\varepsilon^2+a_3\varepsilon^3+a_4\varepsilon^4+b_1E^{b2}$ are reported.

Table 7: Parameter for LAX lens mode

Parameters	Value
$\mathbf{a_0}$	-1.5942
$\mathbf{a_1}$	0
$\mathbf{a_2}$	0
$\mathbf{a_3}$	0
$\mathbf{a_4}$	0
$\mathbf{b_1}$	37.0364
$\mathbf{b_2}$	-0.3849

4.1.4 Small area electronics – SAE 150

The procedure for SAE 150 lens mode gives back as parameters for the transmission function $T = a_0+a_1\varepsilon+a_2\varepsilon^2+a_3\varepsilon^3+a_4\varepsilon^4+b_1E^{b2}$ what is shown in table 8.

Table 8: Parameter for SAE 150 lens mode

Parameters	Value
$\mathbf{a_0}$	1
$\mathbf{a_1}$	0
$\mathbf{a_2}$	0
$\mathbf{a_3}$	0
$\mathbf{a_4}$	0
$\mathbf{b_1}$	-2191130.3575
$\mathbf{b_2}$	-5

These parameters are leading to the quantification result in table 9.

Table 9: Quantification of Cu foil calibration sample for SAE 150 lens mode

Peak name	E_B /eV	Area/cps·eV	Sens. Fact.	Norm. Area	Quant./at.%
Cu 3p Doublet 1	74.91	16356.638	56.697	288.49213	39.61
Cu2p3/2 Peak 1	932.52	83872.081	190.72	439.76091	60.39

The results are not acceptable. Also freeing all the parameters of the polynomial, it is not possible to achieve a proper result probably due to the internal scattering. This approach cannot be used to measure the 20 eV PE for SAE150 mode, it is necessary to use a different one. This method will not be discussed since it's not useful to the aim of this work.

4.1.5 Spectrometers with internal scattering

In all spectrometers some internally scattered electrons, $I_s(E)$, are detected leading to a measured signal $I_m(E)$, given by $I_m(E) = I_i(E) + I_s(E)$.

Generally the scattered electrons arise at the outer hemisphere in concentric hemispherical analysers and at the mirror electrode in cylindrical mirror analysers.

The problem tends to be worst at low pass energies and, in the extreme case, $I_s(E)$ may be greater than $I_i(E)$. Unfortunately, the contribution of $I_s(E)$ varies through the spectrum and is not easy to subtract from $I_m(E)$. The presence of any significant level of scattering is seen through the ratio $I_m(E)/n_i(E)$ used to derive T(E) in Eqn T(E)α $I_m(E)/n_i(E)$ ($n_i(E)$ is the spectrum emitted). This ratio gives

$$\frac{I_m(E)}{n_i(E)} \propto \left(1 + \frac{I_s(E)}{I_i(E)}\right) T(E)$$

The scattering contribution, $I_s(E)$, at energies above and below peaks in an XPS spectrum is very much the same, however the value of it will rise markedly on the low energy side. Thus, whereas $I_m(E)/n_i(E)$ will change smoothly through this region if I_s is very small, a rising step will be observed if I_s is significant. If the rise in $n_i(E)$ is very large at energies just below a peak, the increase in height of the step will be of the order of $I_s(E)/I_i(E)$, where $I_i(E)$ is the spectral intensity at energies just above the peak. [41]

4.2 XPS measurement

4.2.1 Reference

For the assignment of the deconvoluted signals of the various peaks, the following references given in Tables 10 to 12 have been used.

Table 10: Reference table relative to $Na_2[Fe(CN)_5NO]$ for assignment of deconvoluted peaks for the active material [41]

Peaks	**Powder**	
	BE	**Assignment**
N 1s	397.2 eV	CN
	402.5	NO
Fe 2p ½	722.7	Doublet of Fe(III) complex
Fe 2p 3/2	709.5	Doublet of Fe(III) complex

Table 11: Reference table for assignment of deconvoluted peaks for the formulated cathode [42]

Peaks	**Cathode**	
	BE	**Assignment**
C 1s	284.5 eV	Graphite
	291 + 286 eV	PVdF
	285.1	Polymeric phase/PEO
	286.8	CO
	290.0	COOO
F 1s	687.6 eV	PVdF
	684.7 eV	LiF
	686 eV	$LiPF_6$
O 1s	531.6	Carbonates
	532.5	CO organic
	533.3	semiorganic carbonates (-OLi)
	531.5	Li_2CO_3

Table 12: Reference table for assignment of deconvoluted peaks for the electrolyte [43]**:**

Assignment	**Measured binding energy/eV**				
	C 1s	**F 1s**	**Li 1s**	**O 1s**	**P 2p**
Carbon black	284.5	-	-	-	-
Hydrocarbon	285.3	-	-	-	-
LiF	-	685.5	56-57	-	-
Li_2CO_3	290.2	-	56-57	532	-
PEO	286.7	-	-	533	-
$LiPF_6$	-	688	56-57	-	137.8
Li_xPF_y	-	687-688	56-57	-	136.5
$Li_xPO_yF_z$	-	-	56-57	534	134.5-135

For not mentioned signals, NIST XPS database (https://srdata.nist.gov/xps/main_search_menu.aspx) or the "identify lines" tool of the UNIFIT 2017 have been used.

4.2.2 Charge correction

Analysis of insulating materials by XPS often requires correction of the spectral energy scale due to specimen charging. A widely used method is to align the binding energy scale such that the C 1s line from adventitious carbon contamination is in the range 284.6–285.0 eV. In XPS analysis of polymers, it is common to adjust the energy scale such that the lowest binding energy C 1s contribution (hydrocarbon,–CH_x) is aligned to a similar constant value (usually 285.0 or 284.6 eV). [45]

The chemical shifts of functional groups in numerous polymers have been measured in this way. However, with the use of high-resolution XPS instruments, it has been demonstrated that there are small but measurable shifts between chemically similar hydrocarbon functionalities, such as aromatic and aliphatic carbons. In many cases, the alignment of one spectral component to a known binding energy value often relies on complex curve fitting of overlapping features, which can be confidently achieved only when the details of the material structure are known or assumed; for an unknown sample or mixture, this is more difficult. In some cases, the organic structure may not contain any hydrocarbon component. It has been proposed a method using a calibrated electron flood gun to pin the surface potential at a known value. In this procedure, the binding energy of a normally conductive sample is measured in both the grounded configuration and when it is insulated from the spectrometer and floating at the potential of the flooding electrons. The difference in the measured binding energy (grounded versus insulated) is applied to correct the energy scale of an adjacent insulating sample measured under the same conditions. [45]

In some cases only a portion of the sample is insulating with some discrete areas or layers of the sample being conducting or semi-conducting. In these cases a phenomenon known as differential charging can occur. Since the cathode material is a really complex system, as a matter of fact consisting in a mixture of conductive and insulating part, this phenomenon actually occurs. Peaks of F 1s (spectrum 5) and C 1s (spectrum 6) have been chosen as example to show this feature.

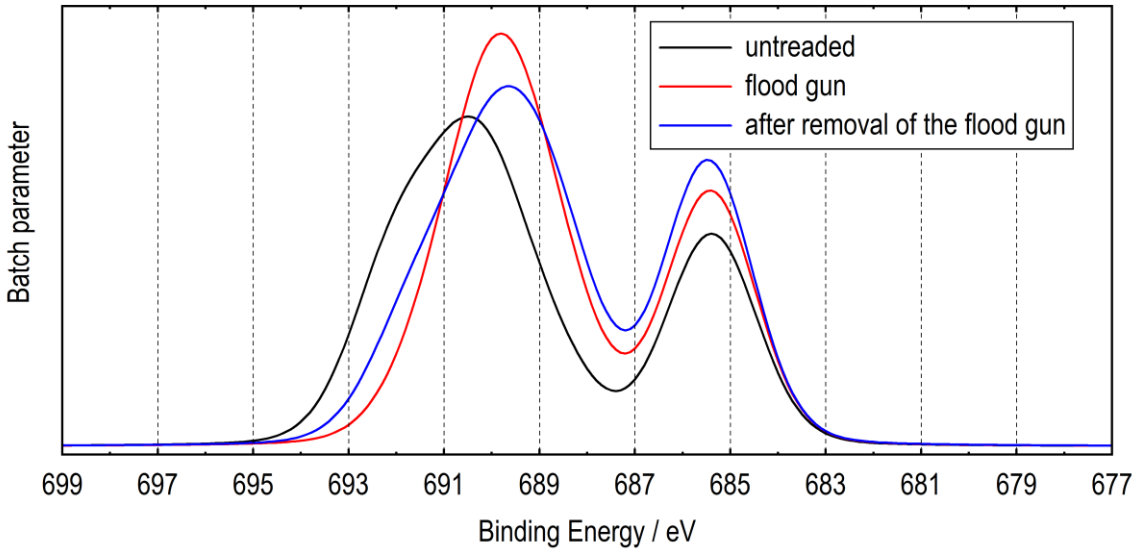

Spectrum 5: Sum curve of F1s from the sample named AM17. The black curve represents the sample itself, without any treatment. The red curve is measured while the flood gun was on and the blue on after the removal of the flood gun.

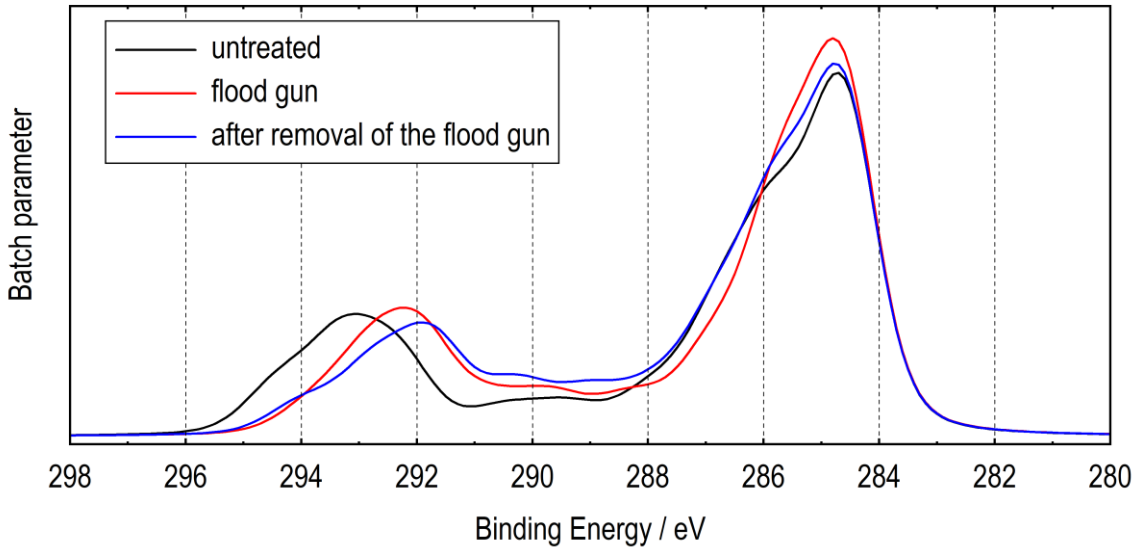

Spectrum 6: Sum curve of C1s from the sample named AM43. The black curve represents the sample itself, without any treatment. The red curve is measured while the flood gun was on and the blue on after the removal of the flood gun.

In both cases it's possible to observe that some parts of the spectra are moving and some other tends to gain intensity keeping the same BE. The simplest and more obvious example is the Teflon area: for F 1s PTFE is located between 688 and 695 eV, for C 1s between 292 and 296 eV. The shift is approximatively 1.5-2 eV. Since some peaks are shifting towards lower binding energy, it's easy to understand that the intensity gained is due to the overlapping of two or more peaks. Interestingly the removal of the flood gun does not establish the same curve as the untreated one. This is probably due to the fact that more time would have been required in order to go back to the equilibrium position.

Since this shift has been established, a charge correction would be needed. However, as it's not possible to apply an univocal charge correction to the sample, and different peaks under the same signal should be corrected with different values, no charge correction has been done in this work. In fact, the peak related to carbon black in the sample, that can be seen around 284.5 eV in spectrum 6, is in a fixed position and does not move with the flood gun.

Moreover, the binding energies of the active material change drastically between a pristine sample and a cycled one. N 1s peak can be used as example of this feature (spectrum 7).

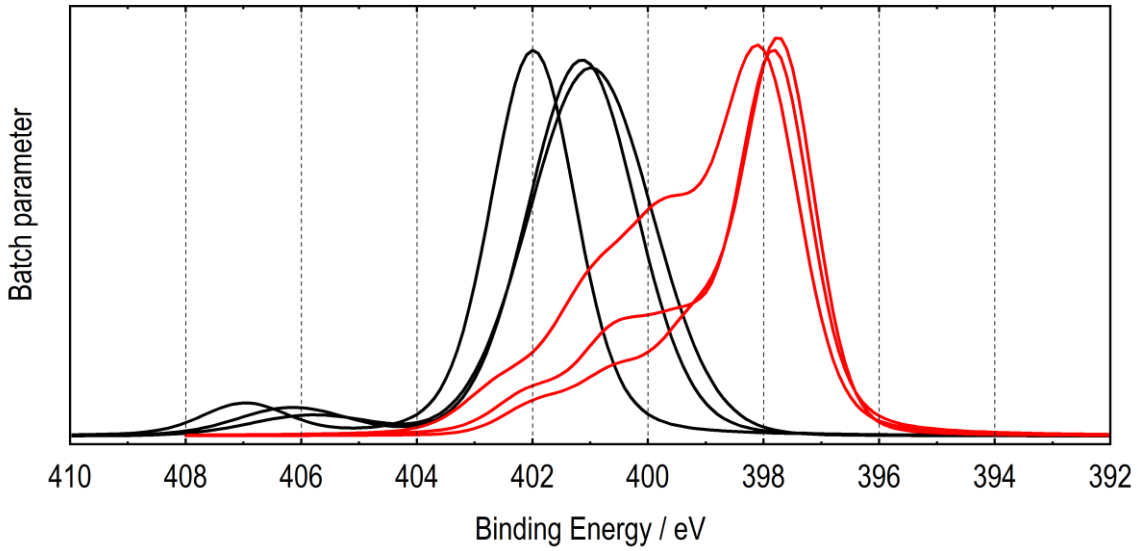

Spectrum 7: sum curves of N 1s from different AM1 samples. The black set belongs to pristine samples, the red set to cycled ones. The curves were normalized at the major peak to 1 in order to make them comparable on a graph.

The reference shown in table 10 indicates the BE for –CN group at around 397 eV and for –NO at 402, this in good agreement with the red curves. However the pristine materials (black curves) display a shift of around 4 eV toward higher BE.

The idea is that an irreversible rearrangement occurs during the first cycles so that the material becomes somehow more conductive. It's interesting to notice that small differences are visible also within the two sets. In particular the powder (black set of curves) is the more shifted towards higher energy – this is totally expected since the formulation of the material and the addition of the electrolyte are meant to make the material more conductive and feasible on battery purpose.

It's in any case quite easy to identify which peak is which. Checking the references from N 1s it's possible to calculate the shift that occur to any active material and choose among the deconvoluted peaks the one that you are looking for, verifying that the BE

gained with this calculated shift is the expected one. These features are valid for both AM1 and AM4 set of samples.

4.2.3 Characterisation

4.2.3.1 Powders

The two sets of samples come from two different powders named AM1 and AM4. The difference between them is that AM1 is anhydrous, with the formula $Cu_{0,8}[Fe_{1,2}(CN)_5(NO)] * 0,3\ H_2O$ and AM4 has hydration water ($Cu_{0,9}[Fe_{1,2}(CN)_5(NO)] * 1,6\ H_2O$). [38]

4.2.3.1.1 AM1

A survey spectrum has been recorded in order to get elemental information. (spectrum 8)

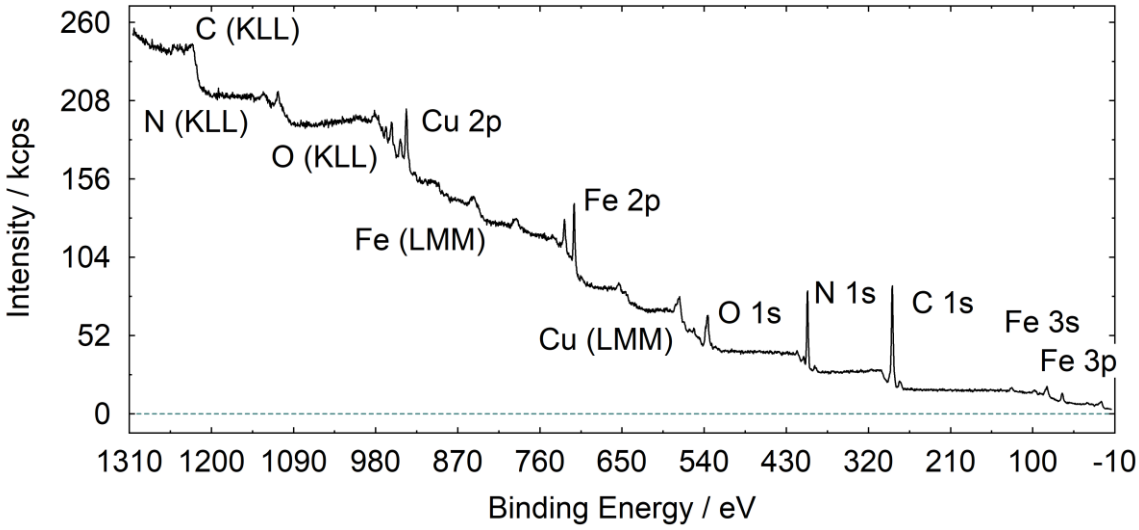

Spectrum 8: survey spectrum of AM1

All the expected elements are present and no impurities are detected.

Detailed spectra are recorded and fitted to gain information about the specimen and the oxidation states on the sample.

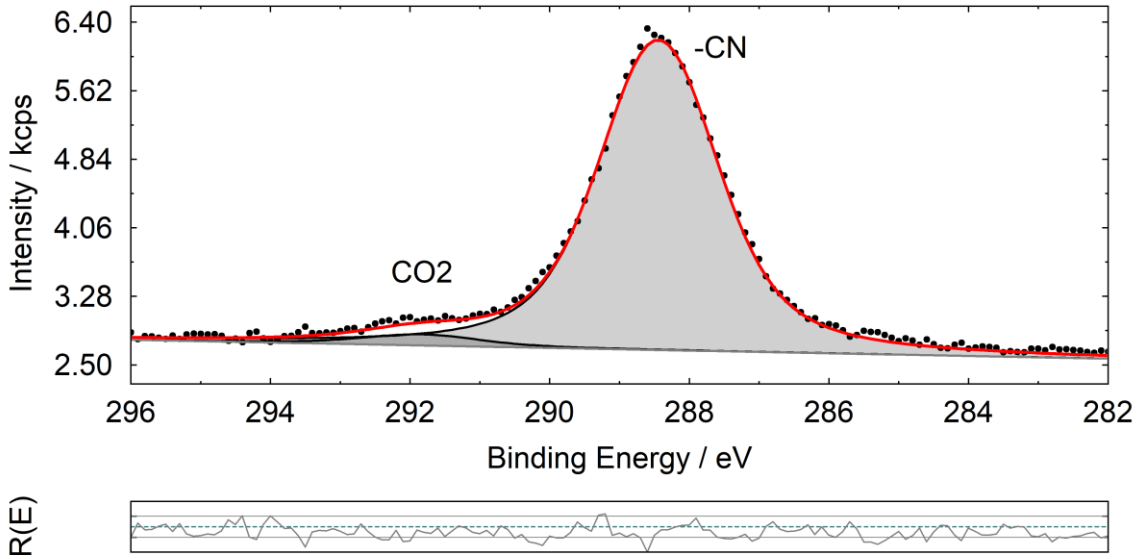

Spectrum 9: C 1s peak of AM1

From spectrum 9, C 1s is dominated by the contribution of –CN group and it seems that there is just a small impurity of CO_2. The –CN group was identified calculating the shift of N 1s respect to the reference and confirming that the resulted BE was consistent with –CN group in NIST database.

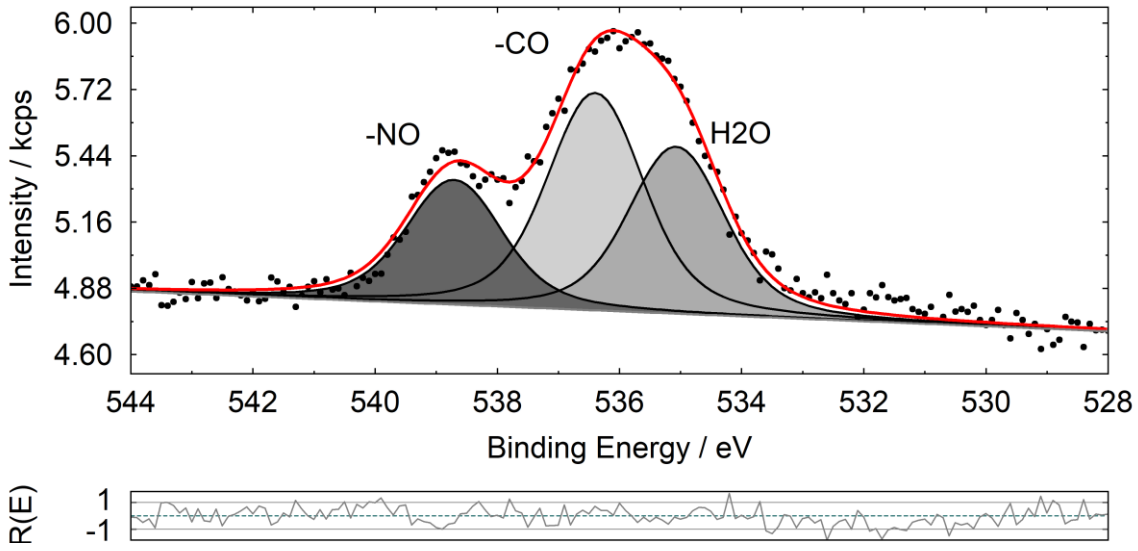

Spectrum 10: O 1s peak of AM1

From spectrum 10, O 1s shows the contribution of three main species: –NO group, –CO and H_2O. –NO group and water are expected from the material, –CO instead is an impurity coming from air, it's probably CO_2 considering C 1s peak.

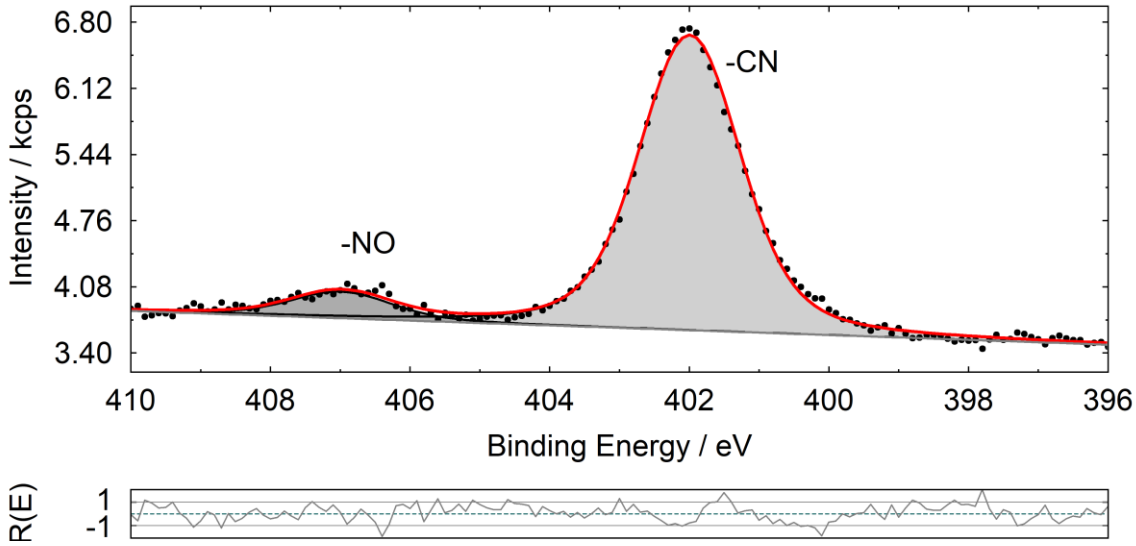

Spectrum 11: N 1s peak of AM1

From spectrum 11, N 1s displays the contribution of two expected species: –NO and –CN groups.

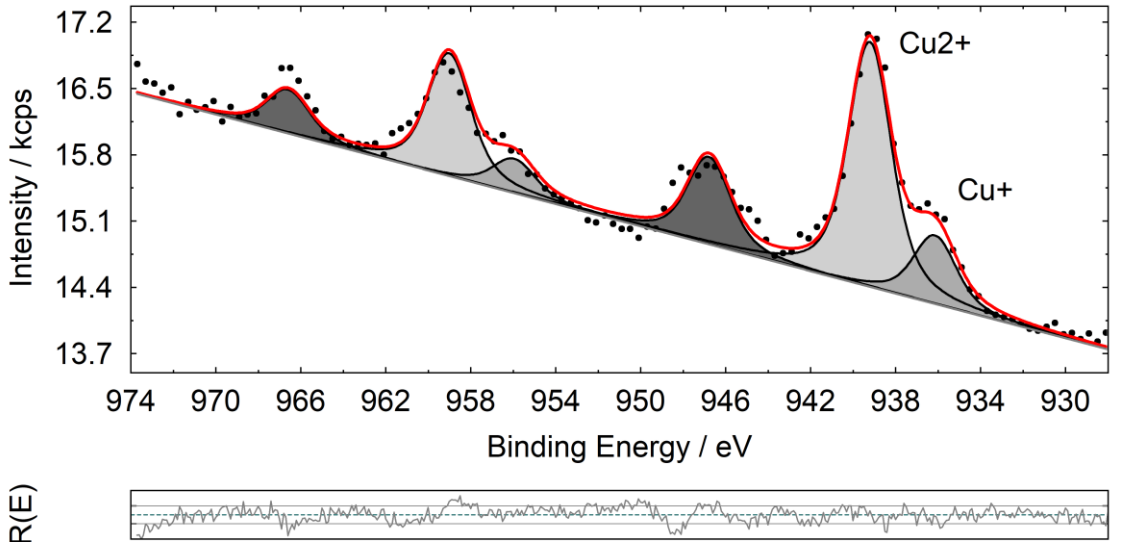

Spectrum 12: Cu 2p peaks of AM1

From spectrum 12, Cu 2p indicates the contribution of two main species and a satellite: Cu^{+} and Cu^{2+}. Only Cu^{2+} was expected and in fact it's the dominant species. The presence of Cu^{+} is probably due to a reduction process that the material goes through while exposed to UHV, process that will be discussed in section 4.2.4.1. Actually, it's also reported in literature that a certain quantity of Cu^{+} is present already on the pristine material. [46]

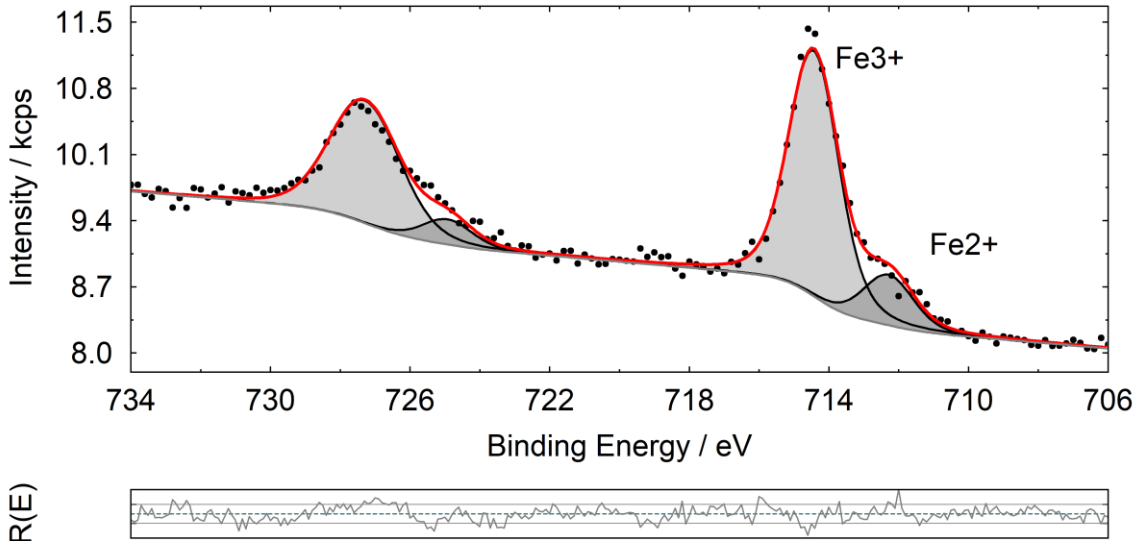

Spectrum 13: Fe 2p peaks of AM1

From spectrum 13, Fe 2p shows the contribution of two main species: Fe^{2+} and Fe^{3+}. Only Fe^{3+} was expected and in fact it's the dominant species. The presence of Fe^{2+} is probably due to same reduction process mentioned above for Cu 2p.

Also a quantitative analysis has been carried on and reported in table 13.

Table 13: Quantification of the specimen for AM1

Peak name	E_B /eV	Area/cps·eV	Sens. Fact.	Norm. Area	Quant./at.%	
C 1s CN	288.44	9090.7970	16.807	540.89349	57.74	59.8
C 1s CO2	291.84	325.05495	16.827	19.317463	2.06	
Cu 2p Cu2+	939.22	12031.054	533.17	22.564926	2.41	3.08
Cu 2p Cu+	936.15	3357.5431	532.36	6.3067968	0.67	
Cu 2p sat	946.79	4295.2390	535.64	0	0	
Fe 2p Fe 3+	714.43	8672.7208	312.63	27.740634	2.96	3.5
Fe 2p Fe2+	712.29	1592.5178	312.31	5.0990104	0.54	
N 1s CN	401.99	6296.4503	31.133	202.24361	21.59	23.53
N 1s NO	406.99	565.84697	31.152	18.164065	1.94	
O 1s CO	536.4	2120.4889	52.592	40.319611	4.3	10.08
O 1s H2O	535.07	1628.2305	52.554	30.982048	3.31	
O 1s NO	538.71	1216.9678	52.649	23.114737	2.47	

As far as concern the –CN peak it's easy to notice that the ratio between C 1s and N 1s is not 1:1, in fact it is 2.7:1. Actually the C 1s is not really reliable in XPS measurement since a lot of impurities can be absorbed on the surface and cannot be resolved with the fitting. I could for example assume that beneath the CN there might also be CO in the C 1s spectrum. The –CO peak instead seems to fit quite well: assuming a CO_2 specie, the ratio between C 1s and O 1s is 1:2.1. Also the ratio for –NO between O 1s and N 1s is acceptable, it's 1.3:1. The ratio between Fe and Cu is 1.1:1, a better ratio respect to 1.5 that was reported in the previous work. [38] Finally, also the ratio between N 1s and Fe

2p fits in an acceptable limit, 6.7:1. In this work all the contribution from satellites eventually coming from both iron and copper are not included in the quantification.

4.2.3.1.2 AM4

The survey and detailed spectra of AM4 are quite similar to the one reported for AM1. Only spectra with remarkable differences are reported here.

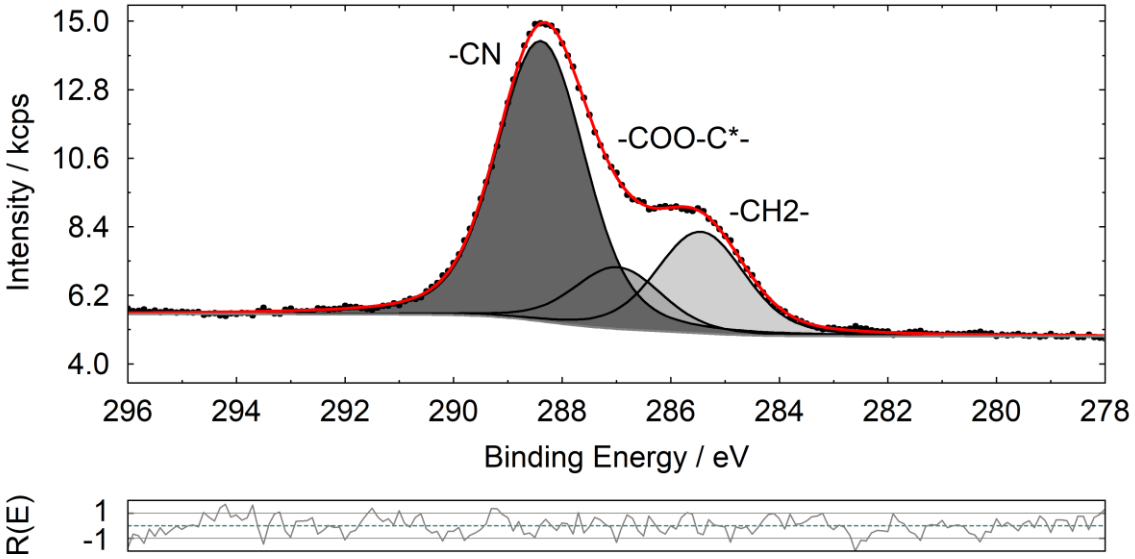

Spectrum 14: C 1s peak of AM4

From spectrum 14, C 1s is dominated by the contribution of –CN group again but more impurities are present: an aliphatic carbon and a CO species which probably have been absorbed on the surface.

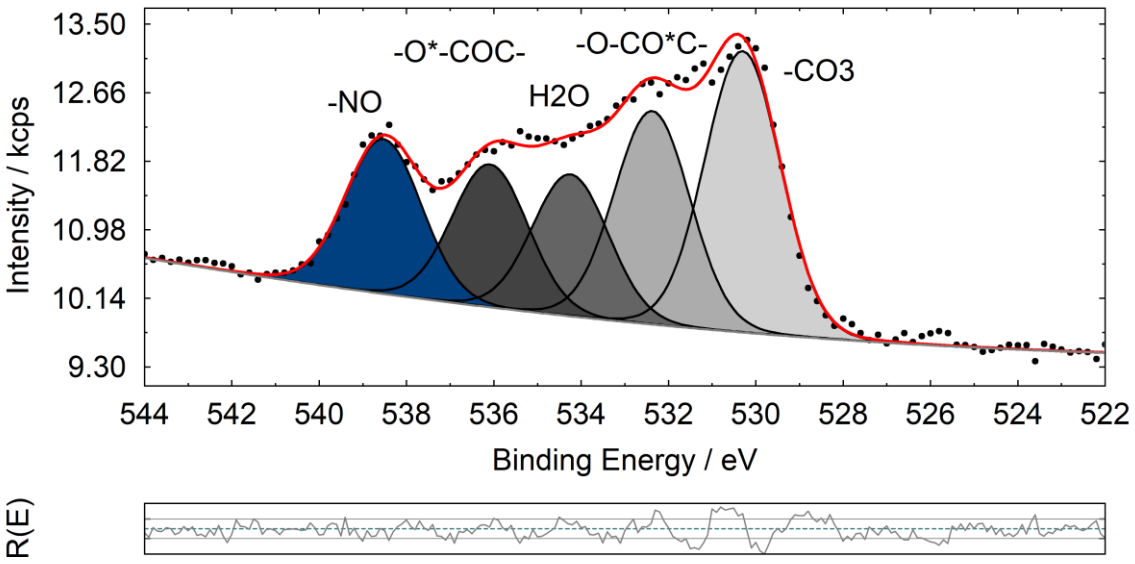

Spectrum 15: O 1s peak of AM4

From spectrum 15, five species are fitted under the peak of O 1s. Again –NO and water are present, but in this case more –CO signals seem to be absorbed on the surface from air.

Also for AM4 a quantitative analysis has been carried on and reported in table 14.

Table 14: Quantification of the specimen for AM4

Peak name	E_B /eV	Area/cps·eV	Sens. Fact.	Norm. Area	Quant./at.%	
C 1s CH2	285.45	7383.8402	17.826	414.21744	12.26	53.52
C 1s CO	286.98	4490.7956	17.829	251.88151	7.46	
C 1s CN	288.39	20368.960	17.84	1141.7578	33.8	
Cu 2p Cu +	935.71	9430.8190	425.63	22.156953	0.66	3.42
Cu 2p Cu 2+	938.95	39725.387	425.48	93.365393	2.76	
Cu 2p sat	946.62	16208.981	424.65	0	0	
Fe 2p Fe 3+	714.22	28282.514	286.06	98.868131	2.93	3.64
Fe 2p Fe 2+	711.72	6836.9519	284.56	24.026229	0.71	
N 1s CN	401.78	24467.860	31.979	765.12275	22.65	24.9
N 1s NO	406.82	2433.5414	31.978	76.100488	2.25	
O 1s -CO3	530.3	7607.3450	51.717	147.09563	4.35	14.52
O 1s -OCO*C-	532.37	5802.7070	51.726	112.18163	3.32	
O 1s H2O	534.25	3868.1895	51.685	74.841627	2.22	
O 1s -O*COC-	536.08	3869.0716	51.675	74.873182	2.22	
O 1s NO	538.53	4202.4137	51.683	81.311335	2.41	

As far as concern the –CN peak in this case a better result has been found: the ratio between C 1s and N 1is 1.5:1. The $–CO_x$ peak is difficult to interpret: considering all the –CO species under the same peak for C 1s and three different contributions for O 1s we gain a ratio of 1:1.33.

The ratio for –NO between O 1s and N 1s is really good, it's 1.1:1.

The ratio between Fe and Cu is 1.1:1, a better ratio respect to 1.3 that was reported in the previous work. [38]

Finally, also the ratio between N 1s and Fe2p fits in an acceptable limit, 6.8:1.

4.2.3.2 Formulated materials

The two powders, separately, have been mixed in a mortar with carbon black, PTFE and VGCF_H in order to obtain a pellet. These pellets are characterised in this section.

4.2.3.2.1 AM1_F

A survey spectrum has been recorded in order to get elemental information. (spectrum 16).

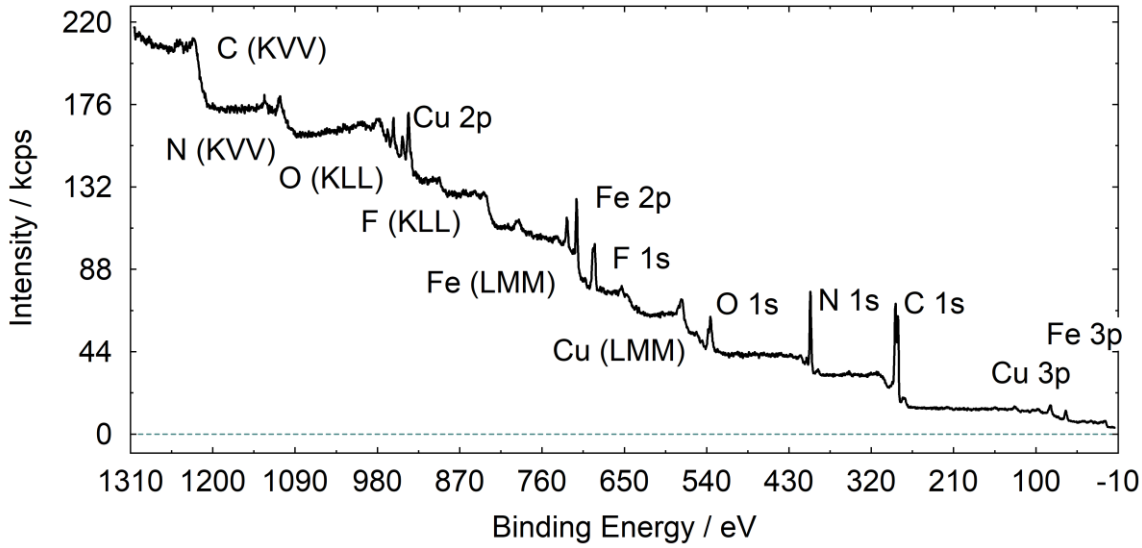

Spectrum 16: survey spectrum of AM1_F

Since PTFE has been added a F 1s peak was expected to appear.

Detailed spectra are recorded and fitted to gain information about the specimen and the oxidation states on the sample.

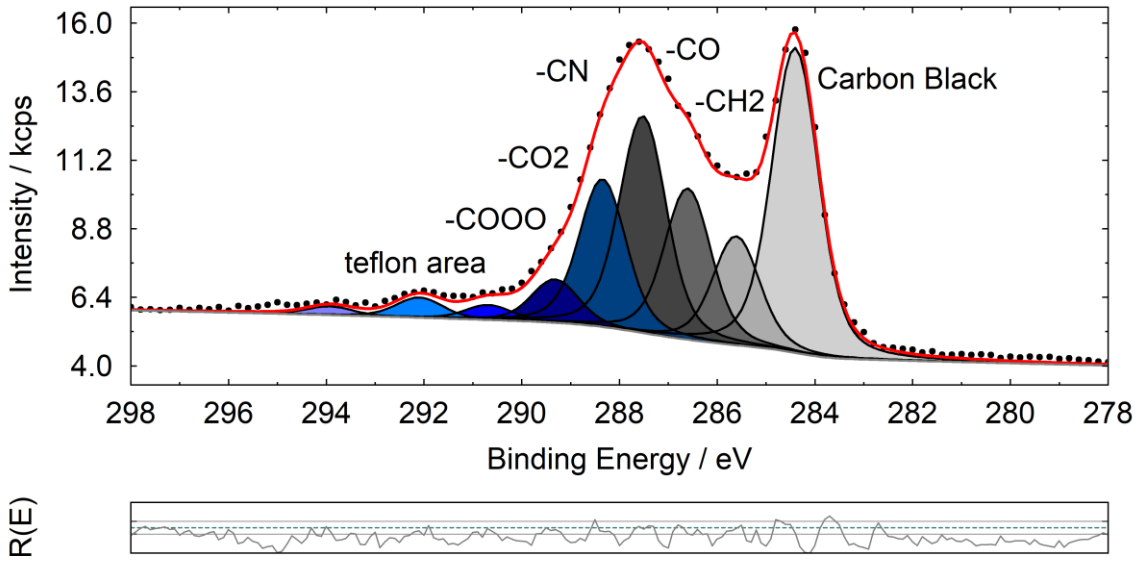

Spectrum 17: C 1s peak of AM1_F

Spectrum 17 shows a really complex system with 9 different species of carbon. Basically all the –CO and –CH peaks are possible for a sample containing CB and VGCF_H and as far as concern the Teflon area, since PTFE is known for undergoing dehydrofluorination process [47], -CF2- and -CFH- species or similar are likely present, as much as some terminal –CF3.

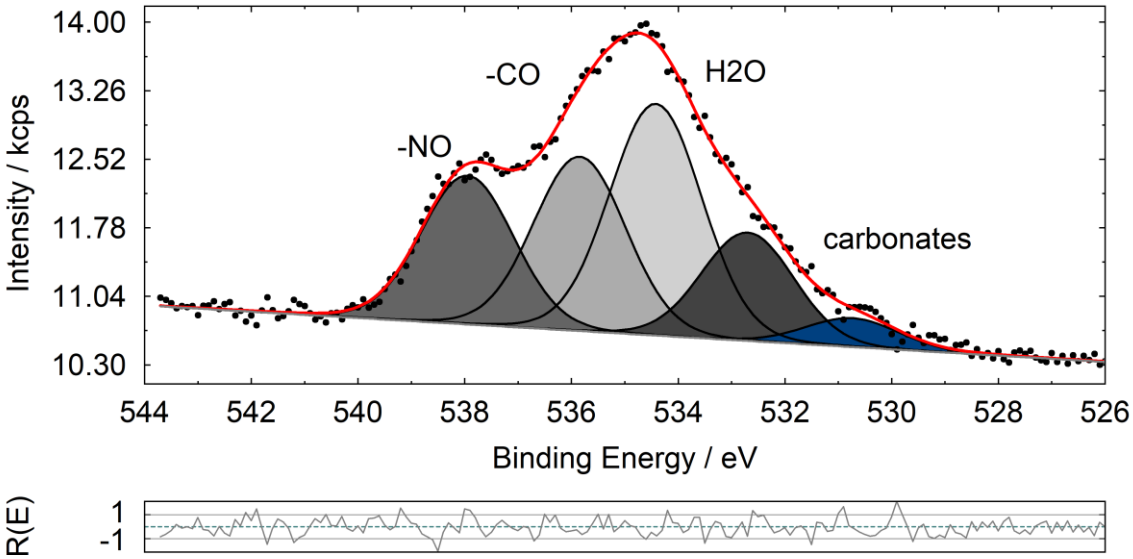

Spectrum 18: O 1s peak of AM1_F

Spectrum 18 displays again five peaks that can be recognised as above, different kind of –CO, water and –NO group.

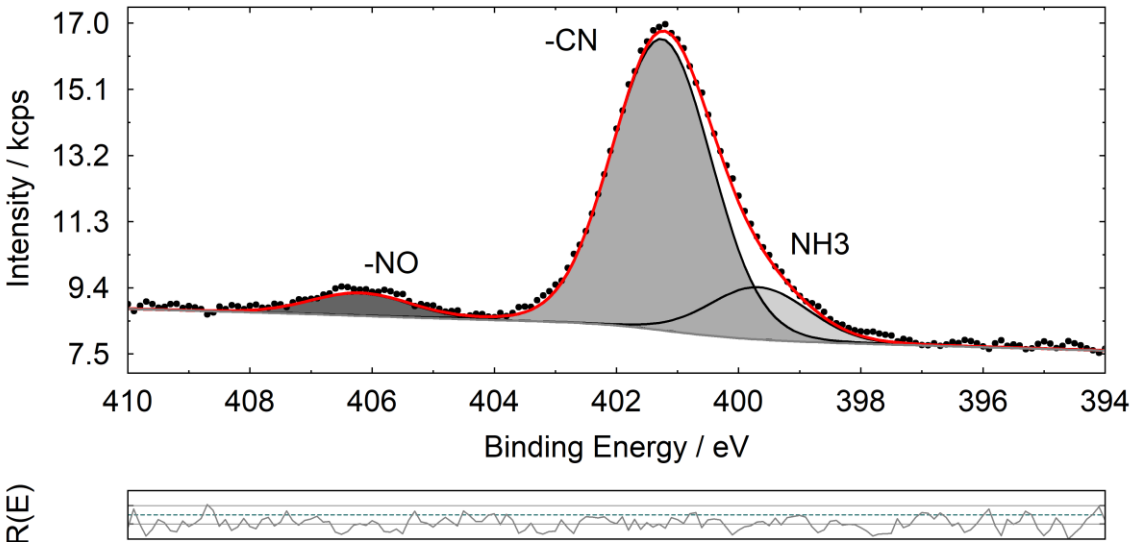

Spectrum 19: N 1s peak of AM1_F

In spectrum 19 three species appear: –NO and –CN groups, as expected, and probably a contribution of ammonia, maybe developed as result of the UHV aging.

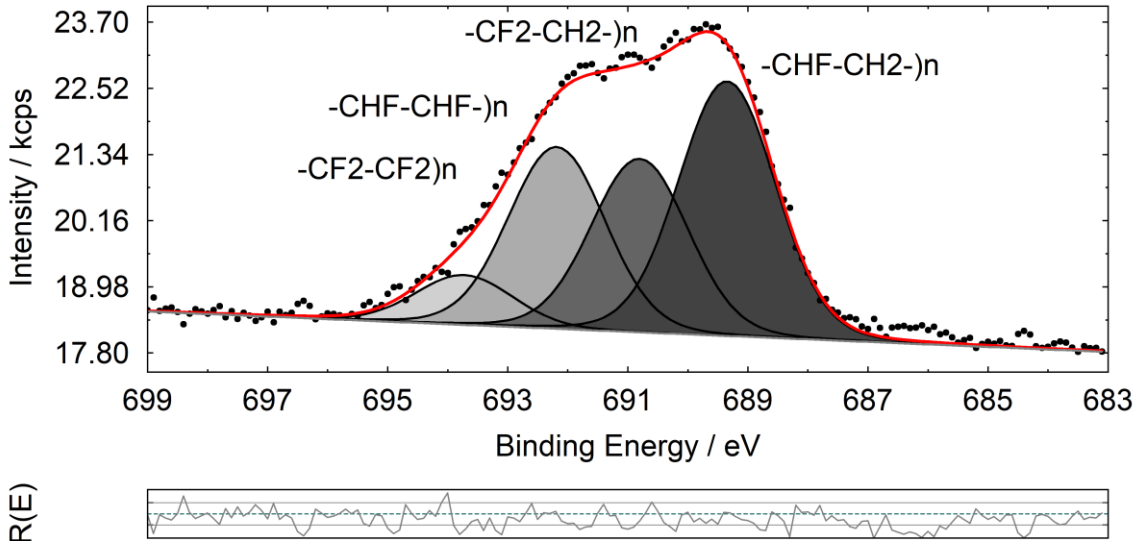

Spectrum 20: F 1s peak of AM1_F

Spectrum 20 has all the peaks that can be expected when PTFE is investigated in XPS, as mentioned above, considering the dehydrofluorination.

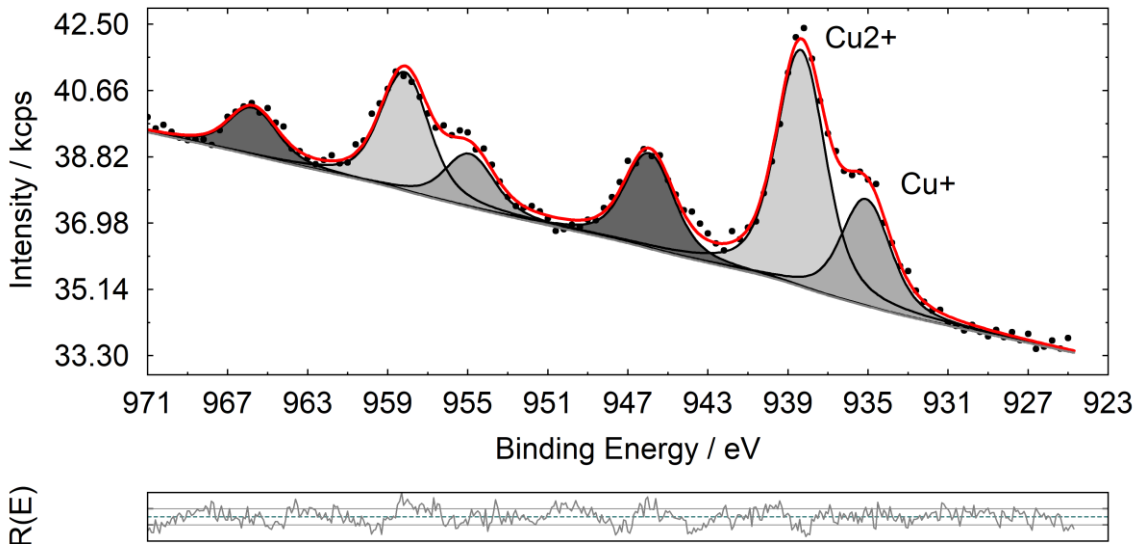

Spectrum 21: Cu 2p peaks of AM1_F

As far as concern the two spectra 21 and the following 22, it's possible to consider as valid the same consideration that has been done for the powders.

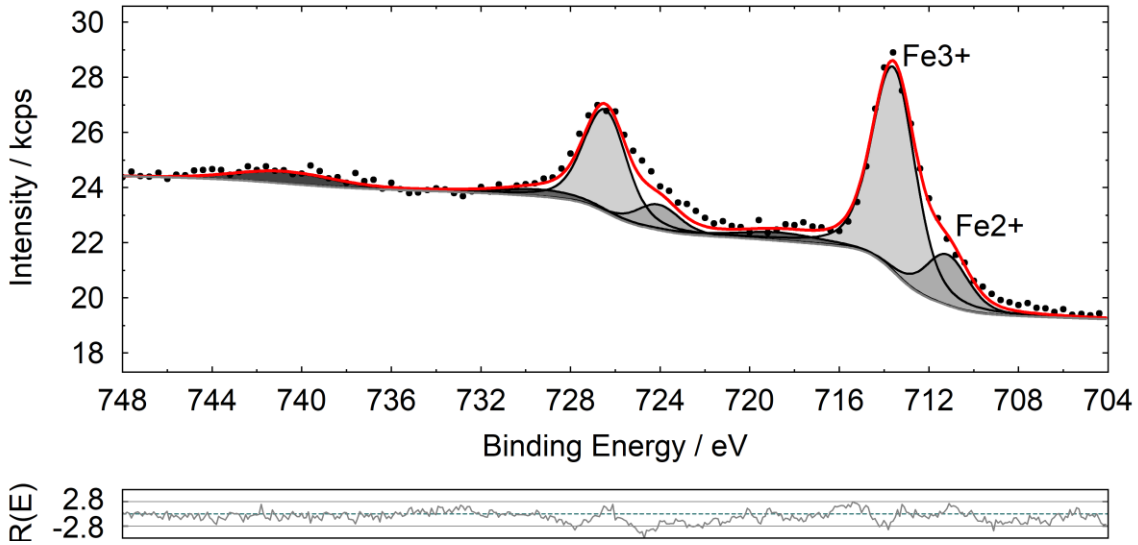

Spectrum 22: Fe 2p peaks of AM1_F

Also in this case, a quantification has been performed. The reults are shown in table 15.

Table 15: Quantification for AM1_F

Peak name	E_B /eV	Area/cps·eV	Sens. Fact.	Norm. Area	Quant./at.%	
C 1s CB	284.41	14629.048	17.844	819.83011	19.01	63.43
C 1s -CH2	285.61	5230.0355	17.846	293.06486	6.8	
C 1s CO	286.6	7254.3773	17.838	406.68109	9.43	
C 1s CN	287.52	10415.777	17.849	583.54964	13.53	
C 1s CO2	288.35	7097.3991	17.84	397.83627	9.22	
C 1s COOO	289.32	2080.8527	17.843	116.62011	2.7	
C 1s teflon area	290.68	717.56512	17.843	40.215497	0.93	
C 1s teflon area	292.09	971.31390	17.854	54.403153	1.26	
C 1s teflon area	293.92	420.18940	17.857	23.530794	0.55	
Cu 2p Cu2+	938.35	35967.920	425.57	84.516652	1.96	2.84
Cu 2p Cu+	935.1	16236.470	425.72	38.138579	0.88	
Cu 2p sat	945.93	14540.646	424.75	0	0	
F 1s -CF2-CF2)n	693.72	1857.9023	77.059	24.110127	0.56	7.41
F 1s -CF2-CFH-)n	692.18	6789.9973	77.148	88.012616	2.04	
F 1s -CHF-CHF-)n	690.8	6476.3101	77.119	83.978139	1.95	
F 1s -CHF-CH2-)n	689.35	9515.2992	77.156	123.32546	2.86	
Fe 2p Fe3+	713.56	30493.739	285.23	106.90667	2.48	3.1
Fe 2p Fe2+	711.19	7573.4564	285.10	26.564117	0.62	
Fe 2p sat	718.63	3498.9295	285.06	0	0	
Fe 2p sat	740.71	2326.2172	284.16	0	0	
N 1s NH3	399.66	3111.4094	31.996	97.243700	2.25	15.8
N 1s -CN	401.26	17366.999	31.996	542.78658	12.59	
N 1s -NO	406.19	1330.4253	31.978	41.604394	0.96	
O 1s H2O	534.42	5528.7314	51.685	106.96974	2.48	7.42
O 1s -CO	535.85	4171.2354	51.675	80.720569	1.87	
O 1s -NO	537.95	3564.4063	51.683	68.966708	1.6	
O 1s carbonates	532.7	2579.1401	51.696	49.890517	1.16	
O 1s carbonates	530.74	689.73951	51.686	13.344803	0.31	

As far as concern the –CN peak, the ratio between C 1s and N 1is 1.1:1. The $–CO_x$ peak is difficult to interpret, but in any case the quantification carries a big error since the quantity of oxygen seems to be really less in comparison to carbon.

The ratio for –NO between O 1s and N 1s is 1.6:1. The ratio between Fe and Cu is 1.1:1.

Moreover, also the ratio between N 1s and Fe2p fits is 4.4:1, less than expected.

The ratio in the Teflon area is 2.7:1 in favour of fluorine, this can be considered acceptable.

4.2.3.2.2 AM4_F

The survey and detailed spectra of AM4_F are quite similar to the one reported for AM1_F. No spectra are reported here as no remarkable differences have been noticed, just changing in atomic ratio. The quantitative analysis is presented in Table 16.

Table 16: Quantification of AM4_F

Peak name	E_B /eV	Area/cps·eV	Sens. Fact.	Norm. Area	Quant./at.%	
C 1s CB	284.39	9204.3384	17.844	515.82259	10.35	54.54
C 1s -CH2-	285.71	5681.8620	17.846	318.38294	6.39	
C 1s -CO	286.56	6637.4515	17.838	372.09617	7.47	
C 1s -CO2	287.63	7553.9250	17.849	423.21278	8.49	
C 1s -COOO	289.23	4324.6204	17.831	242.53381	4.87	
C 1s -CN	288.44	11370.903	17.84	637.38245	12.79	
C 1 teflon area	292.28	587.26299	17.84	32.918329	0.66	
C 1s teflon area	293.91	780.48126	17.839	43.751401	0.88	
C 1s teflon area	295.32	1259.8849	17.842	70.613439	1.42	
C 1s teflon area	296.43	1083.3215	17.824	60.778814	1.22	
Cu 2p Cu+	935.91	10489.694	425.92	24.628031	0.49	3.5
Cu 2p Cu2+	938.93	63823.168	425.48	150.00168	3.01	
Cu 2p sat	946.64	26595.727	424.65	0	0	
F 1s -CHF-CH2-)n	689.45	12024.893	77.105	155.95478	3.13	16.29
F 1s -CF2-CH2-)n	691.31	16907.959	77.134	219.20241	4.4	
F 1s -CF2-CHF-)n	692.9	24877.916	77.096	322.68751	6.48	
F 1s -CF2-CF2)n	694.21	8771.8950	77.125	113.73607	2.28	
Fe 2p Fe3+	714.23	46203.542	285.28	161.95800	3.25	3.49
Fe 2p Fe2+	711.63	3377.0316	285.14	11.843125	0.24	
Fe 2p sat	718.73	4224.5658	284.86	0	0	
Fe 2p sat	741.37	2160.6363	284.19	0	0	
N 1s NH3	400.38	2654.5263	31.979	83.008424	1.67	17.73
N 1s -CN	401.8	23647.460	31.979	739.46840	14.84	
N 1s -NO	406.73	1946.0235	31.978	60.855074	1.22	
O 1s	530.96	298.23489	51.737	5.7644412	0.12	4.47
O 1s carbonates	533.04	1307.1645	51.696	25.285602	0.51	
O 1s H2O	534.89	2372.0768	51.655	45.921533	0.92	
O 1s -CO	536.24	2768.1400	51.675	53.568263	1.07	
O 1s -NO	538.52	4752.9657	51.683	91.963813	1.85	

Concerning the –CN peak, the ratio between N 1s and C 1s is 1.2:1. For the $–CO_x$ peak the same idea expressed for AM1_F are valid.

The ratio for –NO between O 1s and N 1s is 1.5:1. The ratio between Fe and Cu is 1:1.

Moreover, also the ratio between N 1s and Fe2p fits is 4.6:1, again less than expected but really similar to AM1_F.

The ratio in the Teflon area is 3.8:1 in favour of fluorine, this can be considered acceptable.

4.2.3.3 Formulated materials with electrolyte

After the formulation, the materials have been soaked with electrolyte ($LiPF_6$ 1M in EC:PC:3DMC) and left there for three months. The addition of the electrolyte does not change drastically the nature of the surface in comparison to the formulated material: just spectra with remarkable differences are reported in this section.

4.2.3.3.1 AM1_E

A survey spectrum has been recorded in order to get elemental information. (Spectrum 23).

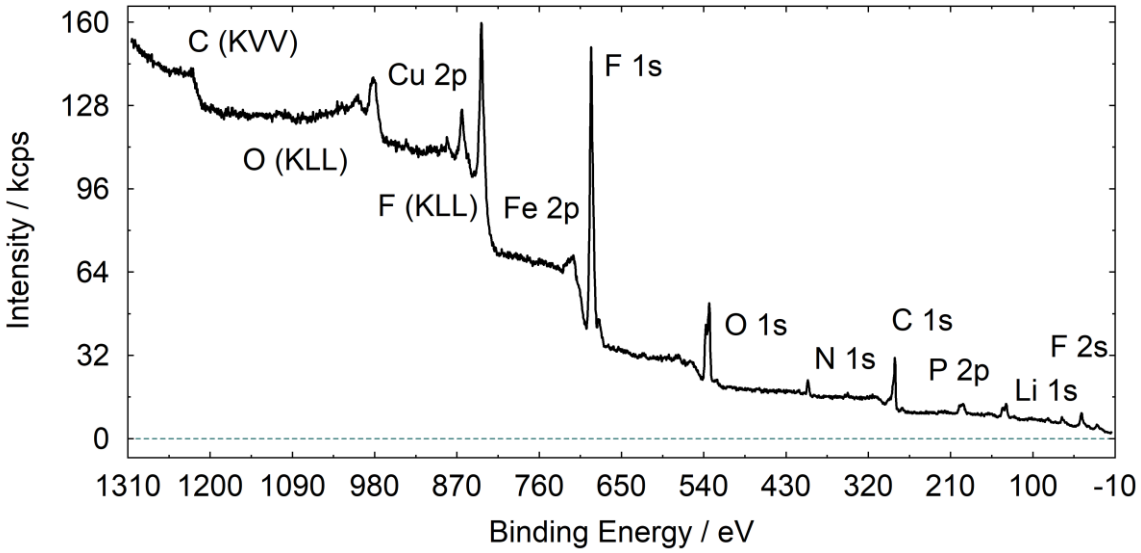

Spectrum 23: survey spectrum of AM1_E

As the electrolyte has been added Li 1s and P 2p were expected to appear.

Detailed spectra are recorded and fitted to gain information about the specimen and the oxidation states on the sample. C 1s, O 1s, N 1s and Cu 2p spectra are similar to AM1_F. Fe 2p spectrum was not evaluated due to a bad signal/noise ratio and also Cu 2p was not easy to process for the same reason; this probably means that a thick electrolyte layer is deposited on the top of the material.

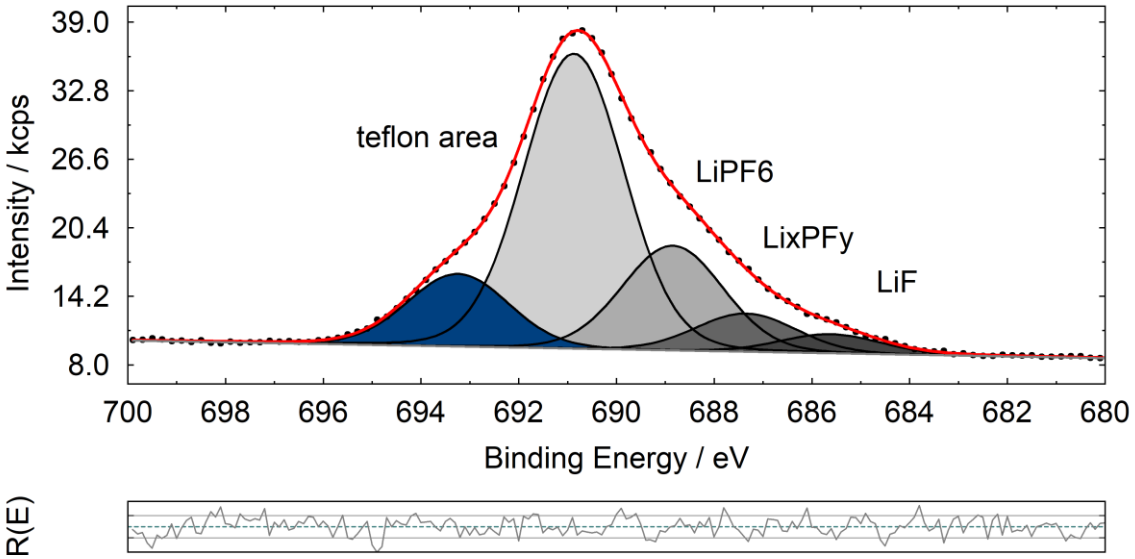

Spectrum 24: F 1s peak of AM1_E

Spectrum 24 shows an interesting feature: $LiPF_6$ has partly decomposed in two different components: Li_xPF_y and LiF. This property will be discussed in a specific section (4.2.7).

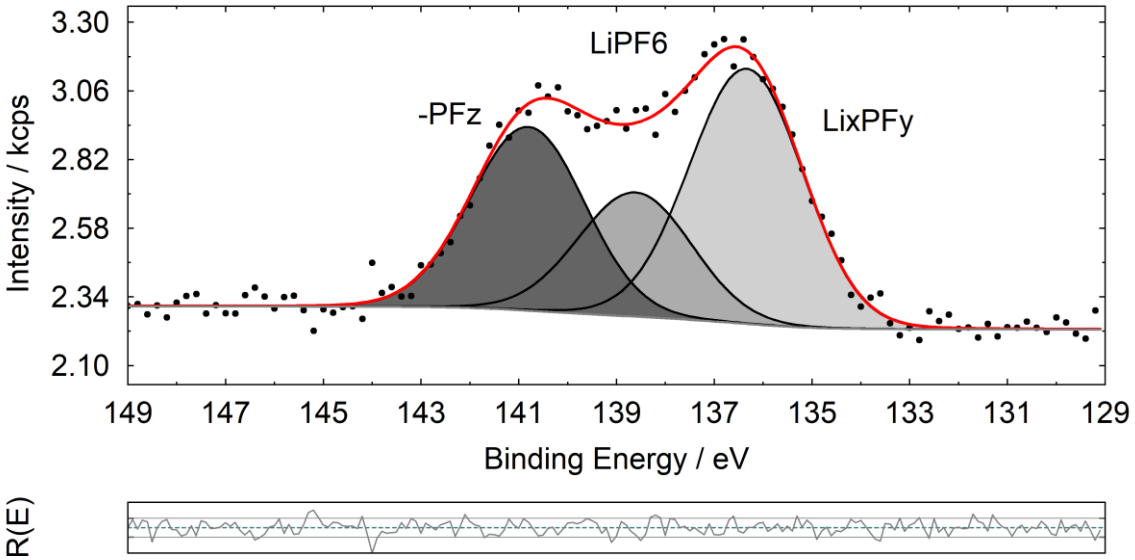

Spectrum 25: P 2p peaks of AM1_E

P 2p spectrum is dominated by the contribution of the electrolyte: $LiPF_6$ and Li_xPF_y are present, but also a peak at higher binding energy. This chemical shift might be explained by a phosphorous bonded to a fluorine with z>6 (but no literature can support this guessing).

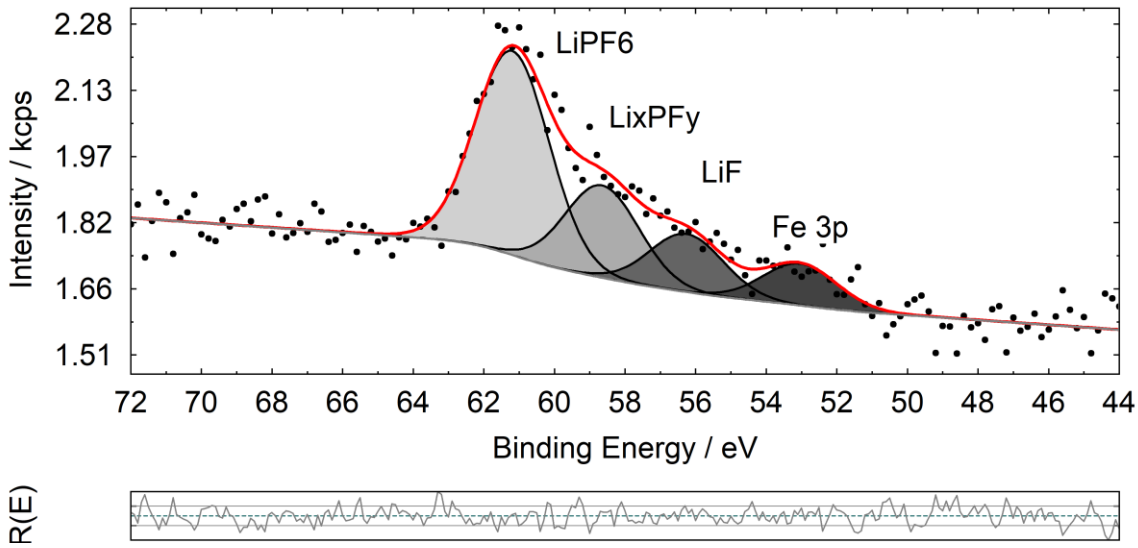

Spectra 26: Li 1s peak for AM1_E

As far as concern Li 1s, it's possible to distinguish again the three contribution of the electrolyte: $LiPF_6$ and Li_xPF_y and LiF. However, since the signal is quite broad, the Li 1s signal is overlapped to Fe 3p signal, this causing an increase of fitting error.

Quantification is summarised in table 17. The system is from now on really complex, the species fitted under a signal are a lot and therefore errors are easy to commit. The first thing that can be seen is the great unreliable amount of lithium: there is a high probability that the sensitivity factor is wrong or at least underestimated. Lithium is the lightest element that is possible to measure in XPS and therefore the determination of the sensitivity factor is kind of complex and in this case is wrong. More peaks are yet to come on cycled samples: quantification will be showed from now on to check the ratio between iron and copper when both are detectable.

Table 17: Quantification for AM1_E

Peak name	E_B /eV	Area/cps·eV	Sens. Fact.	Norm. Area	Quant./at.%	
C 1s CB	284.57	5654.8351	17.835	317.06392	5.46	14.49
C 1s -CH2-	285.85	2266.9362	17.846	127.02769	2.19	
C 1s -CO	287	1940.7820	17.829	108.85535	1.88	
C 1s -CN	288.12	1969.0011	17.84	110.37001	1.9	
C 1s -COOO	289.44	988.84610	17.843	55.419274	0.95	
C 1s teflon area	290.61	738.00072	17.834	41.381671	0.71	
C 1s teflon area	292	516.74278	17.837	28.970274	0.5	
C 1s teflon area	293.48	503.57430	17.839	28.228841	0.49	
C 1s teflon area	294.96	427.80395	17.821	24.005608	0.41	
Cu 2p Cu2+	938.12	6399.2598	425.28	15.046991	0.26	0.46
Cu 2p Cu+	934.97	3326.2306	425.72	7.8131334	0.13	
Cu 2p sat	946.05	1759.7760	424.75	4.1430768	0.07	
F 1s teflon area	690.87	71185.151	77.067	923.67877	15.92	28.58
F 1s LiyPFx	688.85	25297.093	77.09	328.15012	5.65	
F 1s LiyPFx	687.35	9215.7436	77.127	119.48790	2.06	
F 1s LiF	685.61	4601.9070	77.148	59.650374	1.03	
F 1s teflon area	693.24	17533.378	77.11	227.38138	3.92	
Li 1s LiPF6	61.19	1262.7111	1.016	1242.8259	21.41	37.28
Li 1s LiyPFx	58.65	574.72736	1.016	565.67653	9.75	
Li 1s LiF	56.25	360.99621	1.016	355.31123	6.12	
Fe 3p	53.05	260.23798	29.854	0	0	
N 1s -CN	401.37	2211.6383	31.996	69.122339	1.19	1.95
N 1s NH3	400.13	1269.4878	31.979	39.697545	0.68	
N 1s -NO	405.9	153.71876	31.995	4.8044619	0.08	
O 1s carbonates	533.02	11695.657	51.696	226.23912	3.9	12.53
O 1s H2O	534.64	8469.8406	51.685	163.87425	2.82	
O 1s CO	536.31	5821.2281	51.694	112.60935	1.94	
O 1s -COO	537.77	9733.5892	51.714	188.21961	3.24	
O 1s -NO	539.33	902.46976	51.672	17.465353	0.3	
O 1s -PO	530.81	995.19453	51.686	19.254624	0.33	
P 2p LixPFy	136.07	2624.4213	21.314	123.13133	2.12	4.68
P 2p LiPF6	138.35	1278.6855	21.321	59.973057	1.03	
P 2p -PFz	140.54	1892.1001	21.319	88.751824	1.53	

4.2.3.3.2 AM4_E

No spectra are shown for AM4_E since they are really similar to AM1_E. The species fitted are the same and no remarkable differences are detected. Cu 2p and Fe 2p signals are both detectable, also in this case with a bad signal to noise ratio. This makes the quantification (that gives a ratio of 2:1 in favour of iron) in table 18 not reliable.

Table 18: Quantification for AM4_E

Peak name	E_B /eV	Area/cps·eV	Sens. Fact.	Norm. Area	Quant./at.%	
Cu 2p Cu+	935.72	5988.0938	425.63	14.068546	15.25	32.5
Cu 2p Cu 2+	938.45	6772.3847	425.57	15.913605	17.25	
Cu 2p sat	946.39	3245.5734	424.37	0	0	
Fe 2p Fe 3+	713.36	10313.384	285.04	36.182109	39.21	67.51
Fe 2p Fe 2+	714.7	7465.3170	285.86	26.114651	28.3	
Fe 2p pre edge	711.11	3203.2949	285.10	0	0	
Fe 2p sat	717.95	3740.5639	284.23	0	0	
Fe 2p sat	720.37	4011.3689	284.95	0	0	

4.2.3.4 Cycled materials

Cycled materials are really similar to each other, the species are basically always the same and really a few differences are present between them and also in comparison to AM1_E and AM4_E. The samples that have been investigated by XPS and some information about the cycling itself are summarised in table 19.

Table 19: Cycled materials

	Sample ID	**State of charge**	**Number of electrochemical cycles**
AM 1	AM12	Charged	180
	AM14	Discharged	143
	AM17	Discharged	3
AM 4	AM41	Charged	64
	AM42	Charged	114
	AM43	Discharged	51
	AM44	Charged	22

The main difference in comparison to previous materials are:

a) Chemical shifts of the active material. As mentioned in section 4.2.2, position of all the species related to copper nitroprusside are shifted of about 4 eV toward lower and expected binding energies. This shift in particular affects the fitting of C 1s peak: the BE of –CN is now the same of the carbon black typical one so that it is not possible to distinguish the two contributions anymore.

b) Oxidation states of iron and copper: for charged and discharged materials, different oxidation states are expected. However, since a huge and fast change is happening due to the UHV ambient, no information can be gained about the initial state of the material. An attempt of calibration curve has been carried on in a diagram time VS percentage. All the details are present in paragraph 4.2.4.

c) N 1s peak: two species between –CN group and –NO groups have been appeared. This theme will be deeply discussed in a special section (4.2.5).

d) Decomposition of the electrolyte: peaks assigned to LiF in F 1s signals are used to acquire information about the relationship between number of cycles and deterioration of the surface. Also in this case, more details may be found in paragraph 4.2.6.

4.2.4 Oxidation states of iron and copper

4.2.4.1 UHV and X-ray aging

Due to the use of highly energetic photons for excitation of the sample, the risk of radiation damage exists. The highly energetic beam spot may lead to degradation of the components and may alter their chemical nature. [39] Moreover the UHV conditions may lead to additional damages if the material is not stable. AM1_F and AM4_F have been chosen as reference materials in order to understand whether these kind of damages occur or not: both of the samples show sensibility and damaging while measuring and exposing to UHV ambient.

The samples were exposed for a total of 111h to UHV and measured several times. Cu 2p and Fe 2p signals have been selected to show the effects.

4.2.4.1.1 AM1_F

AM1_F was the first to be investigated under the hope that no damage will be perpetrated: just four points have been measured – 2h, 3h, 16h and 111h.

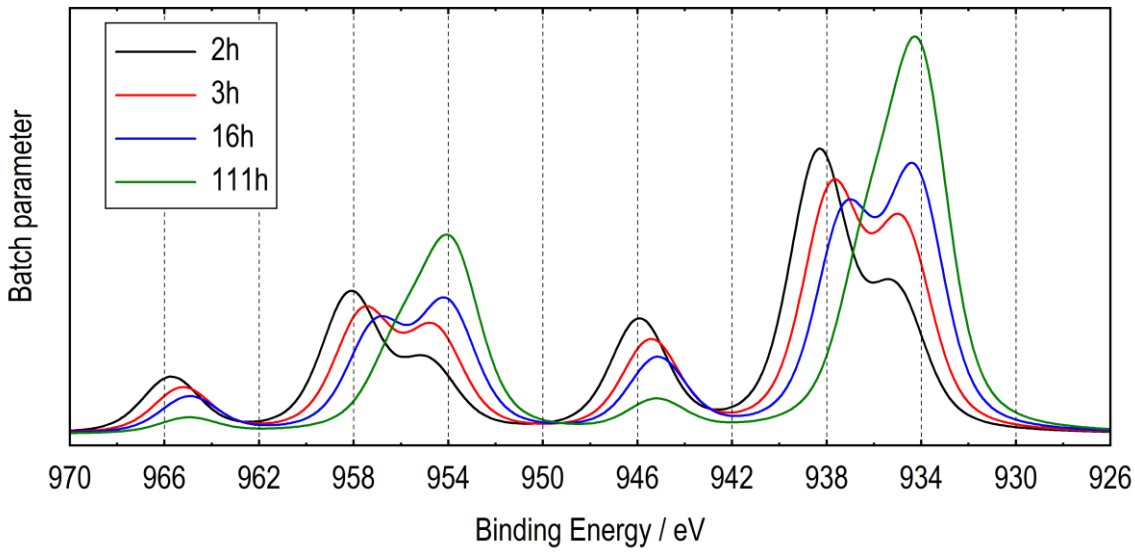

Spectrum 27: sum curve of Cu 2p peaks when aging in UHV for AM1_F

In spectrum 27 it's possible to observe that peaks at around 938 and 946 are going down with time while the peak at around 934 is rising. Moreover, a shift toward lower binding energy is visible. Cu 2p peaks have significantly split spin-orbit components and it's possible to distinguish copper oxidation states using satellite features of Cu 2p. Cu^{2+} (BE at 938eV) has observable collection of satellite features at 946 eV. In Cu^{+}, there is only a very weak satellite. The aging in UHV seems to end up in a reduction reaction on the metal that goes from a Cu^{2+} dominant species to a Cu^{+} one. An attempt of calibration curve has been made using the value of table 20, Cu^{+} and Cu^{2+} are expressed as atomic percentage and the values are gained as result of the fitting process.

Table 20: time aging value for Cu2p peaks of AM1_F

Time (h)	Cu^{+} (%)	Cu^{2+} (%)
2	31,76	68,24
3	45,34	54,66
16	54,77	45,66
111	92,08	7,92

Resulting in figure 13.

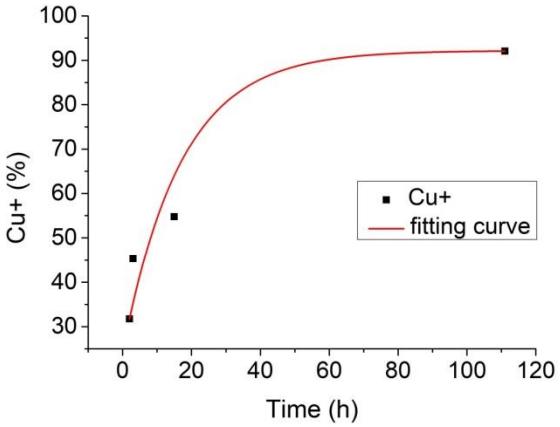

Figure 13: calibration curve of Cu^{+} for AM1_F

Parameters for the fitting curve are reported in table 21.

Table 21: Parameters of fitting curve for Cu^{+} in AM1_F

Equation	y = y0 + A1*(1 - exp(-x/t1)) + A2*(1 - exp(-x/t2))
y0	24,31606
A1	33,93574
t1	17,21601
A2	33,93574
t2	17,21601

From this calibration curve, it's possible to gain information at t=0h and suggest a percentage of Cu^{+} at the beginning of about 24%, resulting in 76% for Cu^{2+}.

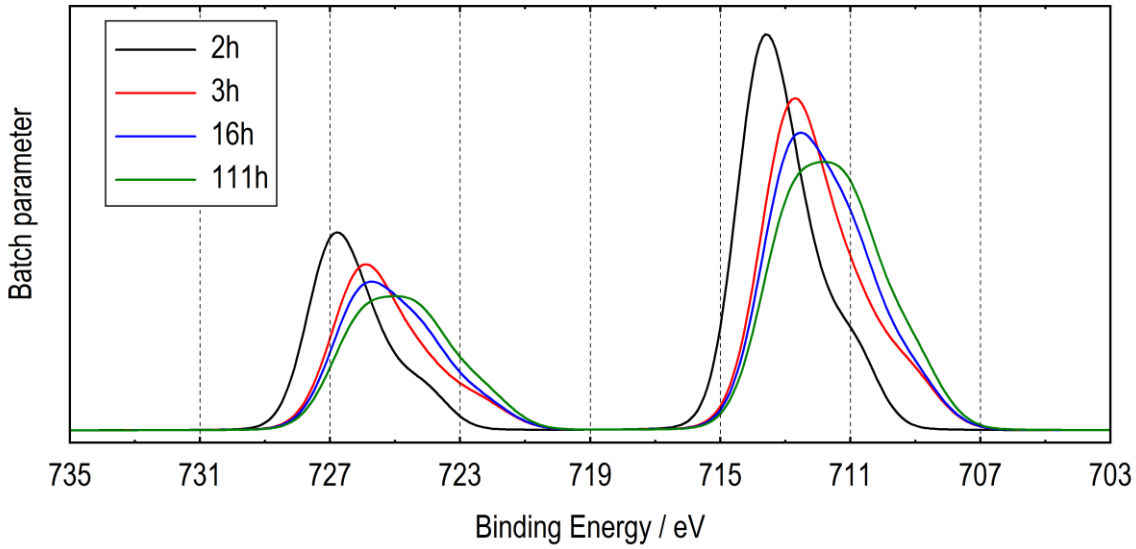

Spectrum 28: sum curve of Fe 2p peaks when aging in UHV for AM1_F

Iron shows the same trend of copper (spectrum 28). The peak around 714 eV, assigned to Fe^{3+}, is going down while the one at 711 eV (assigned to Fe^{2+}) is rising.

Table 22 summarises the quantitative values in atomic percentage that the fitting gives back for Fe 2p peaks.

Table 22: time aging value for Fe2p peaks of AM1_F

Time (h)	Fe^{2+} (%)	Fe^{3+} (%)
2	27,75	72,25
3	30,27	69,73
16	39,91	60,09
111	49,86	50,14

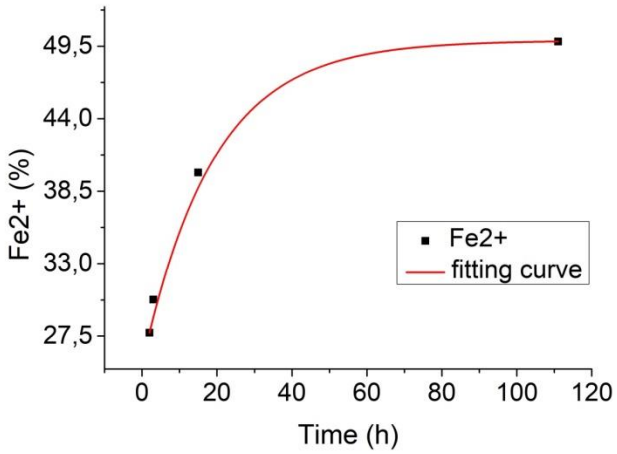

Figure 14: calibration curve of Fe^{2+} for AM1_F

Table 23: : Parameters of fitting curve for Cu^{+} in AM1_F

Equation	y = y0 + A1*(1 - exp(-x/t1)) + A2*(1 - exp(-x/t2))
y0	18,44922
A1	7,2706
t1	10,59789
A2	7,2706
t2	10,59789

From the calibration curve described in table 23 it's possible to gain information at t=0h and suggest a percentage of Fe^{2+} at the beginning of about 18%, giving also back a percentage of Fe^{3+} of 82%.

Since the whole curve for both copper and iron is quite hard to fit in a different way and surely for the majority of the samples no more than 4/5 hours were needed for measure the sample, point at 16 and 111 should have been excluded. A calibration curve with only two points is not reliable.

4.2.4.1.2 AM4_F

AM4_F has been investigated after processing AM1_F data. Five points have been measured – 1h, 2h, 3h, 4h and 5h: the typical interval of time that can be considered for the investigation of these kind of surfaces. This was made with the hope to be at the very beginning of the exponential curve in order to be able to approximate the exponential trend to an easier one, for example to a polynomial curve.

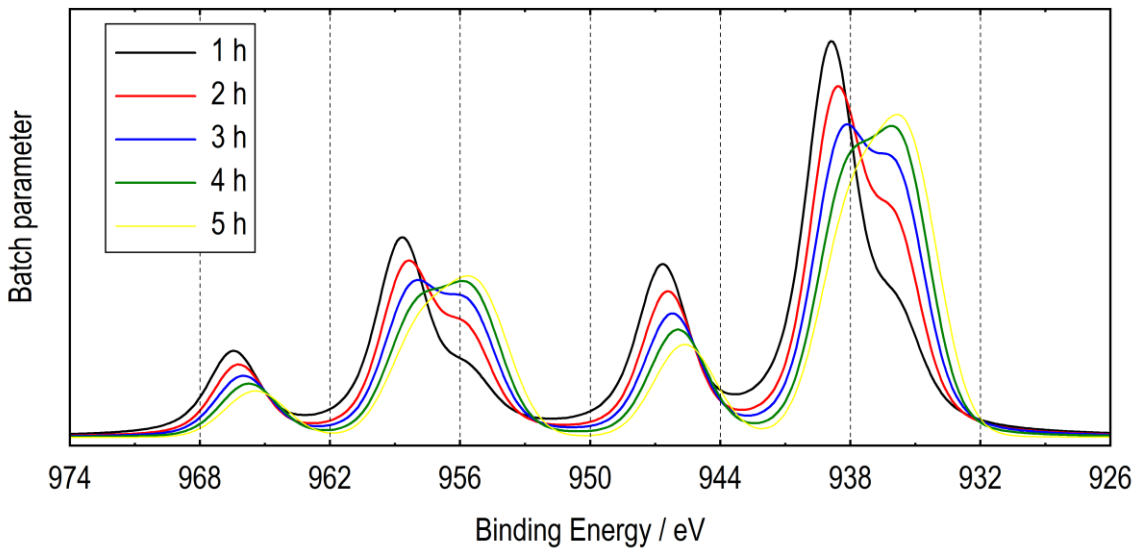

Spectrum 29: sum curve of Cu 2p peaks when aging in UHV for AM4_F

The same qualitative considerations done for AM1_F can be used for describing AM4_F trend. The values coming from the fitting of the spectra are summarised in table 24.

Table 24: : time aging value for Cu2p peaks of AM4_F

Time (h)	Cu^{+} (%)	Cu^{2+} (%)
1	19,21	80,79
2	35,73	64,27
3	45,81	54,19
4	53,09	46,91
5	57,1	42,9

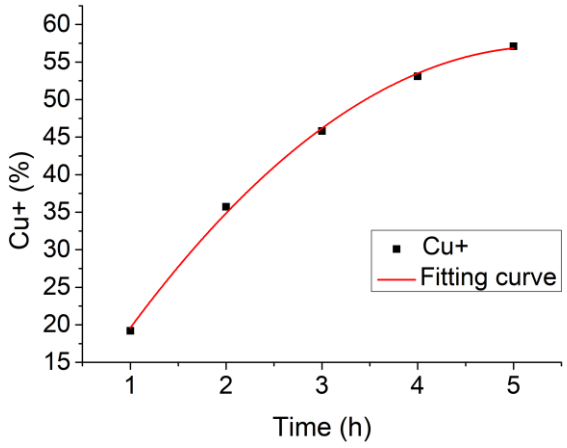

Figure 15: calibration curve of Cu^{+} for AM4_F

Parameters for the fitting curve are reported in table 25.

Table 25: Parameters of fitting curve for Cu^{+} in AM4_F

Equation	$y = Intercept + B_1*x + B_2*x^2$
Intercept	0,336
B_1	21,23686
B_2	-1,98714
Adj. R-Square	0,9973

For AM4_F it's possible to extrapolate a value for an hypothetic time 0 (time of the insertion of the sample in XPS) and have a rough idea of the ratio between Cu^{2+} and Cu^{+}. Inserting the value of 0 for x in the equation, it's possible to gain the value of 0.336 for the percentage of Cu^{+}. Of course, accepting this result, the atomic percentage for Cu^{2+} is 99.664.

Moreover, it's possible to make a cautious guess about the fact that probably also for AM1_F the result would have been similar since the value for 2 and 3h are really alike. In spectrum 30 it's possible to observe the iron trend.

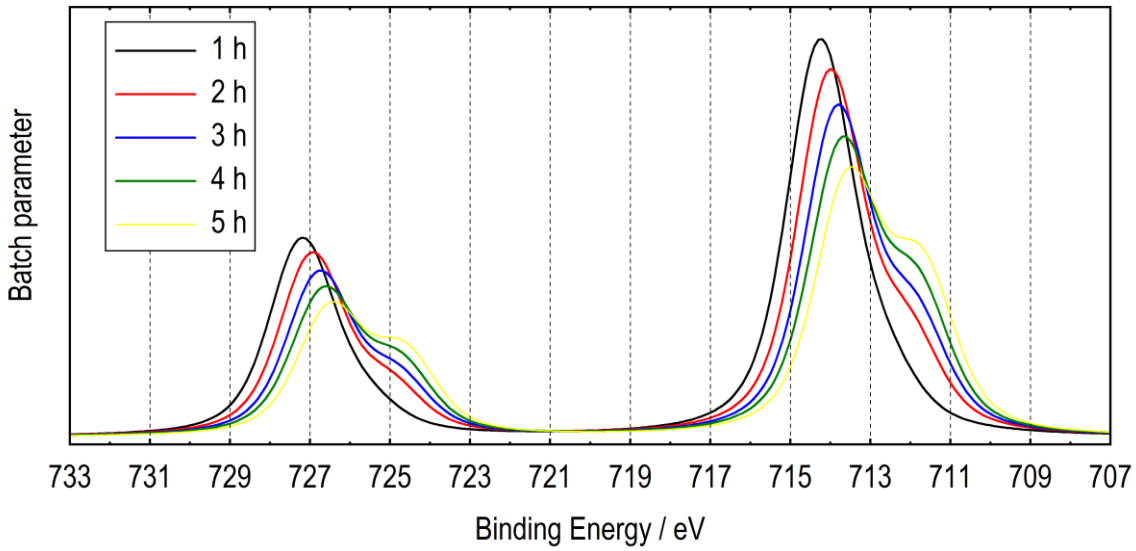

Spectrum 30: sum curve of Fe 2p peaks when aging in UHV for AM4_F

Also in this case it's possible to describe the spectrum in the same way of spectrum 28. The values coming from the fitting of the spectra are summarised in table 26.

Table 26: : time aging value for Fe2p peaks of AM4_F

Time (h)	Fe^{2+} (%)	Fe^{3+} (%)
1	11,07	88,93
2	19,48	80,52
3	24,8	75,2
4	31,89	68,11
5	38,39	61,61

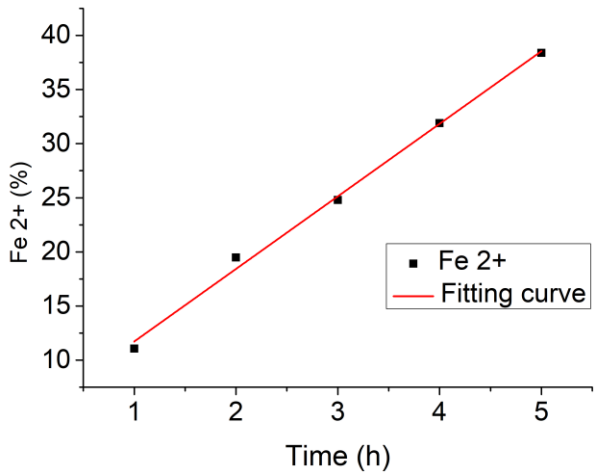

Figure 16: calibration curve of Fe^{2+} for AM4_F

Parameters for the fitting curve are reported in table 27.

Table 27: : Parameters of fitting curve for Fe^{2+} in AM4_F

Equation	$y = Intercept + B_1*x + B_2*x^2$
Intercept	3,986
B_1	7,58357
B_2	-0,14643
Adj. R-Square	0,99393

It's again possible to extrapolate a value for time 0 and guess the ratio between Fe^{2+} and Fe^{3+}. Inserting the value of 0 for x in the equation, it's possible to obtain the value of 4% for the percentage of Fe^{2+} (making $Fe^{3+} \approx$ 96%).

4.2.4.1.3 General considerations

From both the samples and the metals a deep impact on the materials has been noticed. All elements are affected by the ambient in which they've been measured. The process of modification is fast but for long times of exposition a sort of plateau is gained and no more changes are observable. The shrewdness in further XPS investigations was to measure as fast as the pressure was in the right interval: usually at least two hours are needed when the material contains electrolyte due to a degassing process. Just in two cases three days were needed to start the measure: for both the pristine samples with electrolyte and for AM16 (the only sample that was never exposed to air after the removal from the coin cell, section 4.2.7).

4.2.4.2 State of charge and oxidation states

With all the precaution of the case, table 28 reports the oxidation states of iron and copper for the cycled samples.

Table 28: Oxidation states percentage for cycled samples

Sample ID	State of charge	N of cycles	Current rate	Iron		Copper	
				2+	3+	1+	2+
AM44	Charged	22	C/40	62,69	37,31	-	-
AM41	Charged	64	C/5	66,39	33,61	62,3	37,7
AM42	Charged	114	C/10	70,42	29,58	66,53	33,44
AM12	Charged	180	C/10	73,4	26,6	-	-
AM17	Discharged	3	Voltammetry 0.1 mV/s	74,44	25,56	59,6	40,4
AM43	Discharged	51	C/20	56,85	43,15	-	-
AM14	Discharged	143	C/10	51,78	48,22	71,77	28,23

Copper data are incomplete: sometimes might happen that the electrolyte layer is so thick that some elements are not visible. The comparison is possible despite the UHV aging problem: all the samples were exposed basically for the same time to the ambient. The values are considered just relative one to the other and not as absolute.

It's possible to see a trend:

- For charged materials the content of Fe^{2+} and Cu^{+} tend to increase during cycle, while Fe^{3+} and Cu^{2+} decrease.
- For discharged materials the content of Fe^{2+} tend to decrease during cycle, while Fe^{3+} increase. Cu^{+} also in this case increase during cycle.

Some consideration must be done for this kind of result. With XPS just the surface is investigated (around 1% of the whole material): in particular the surface that was not exposed to the separator as summarised in figure 17 (the one in the opposite side respect to insertion process of lithium – this because on the right part mainly cellulosic element were detected.) The lithium diffusion is slow and the effect of that even more.

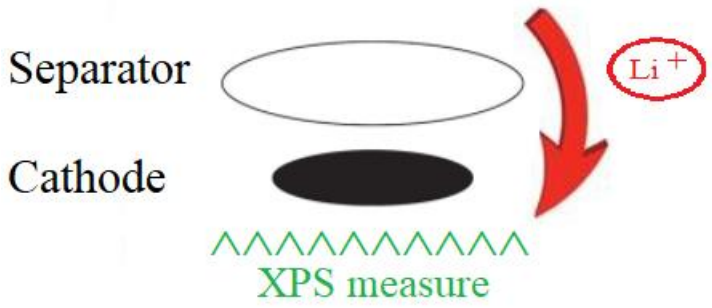

Figure 17: Experimental assets of XPS measure

There are differences in the density of current used for charging/discharging process. The slower the process was, the easier it was to gain the equilibrium point.

Probably the reason for the increase of reduced state of charge during cycling is due to a hysteresis on the ionic transfer in the material. As a matter of fact the capacity retention tends to be decreased with high number of cycles

4.2.5 N 1 evolution

As anticipated in section 4.2.3.4, N 1s signal for cycled samples shows great differences in comparison to pristine ones.

In spectra 31 and 32, it's possible to observe that two new peaks are now present between –CN and –NO ones. The trend is the same for all cycled samples but the ratio between peaks is always different.

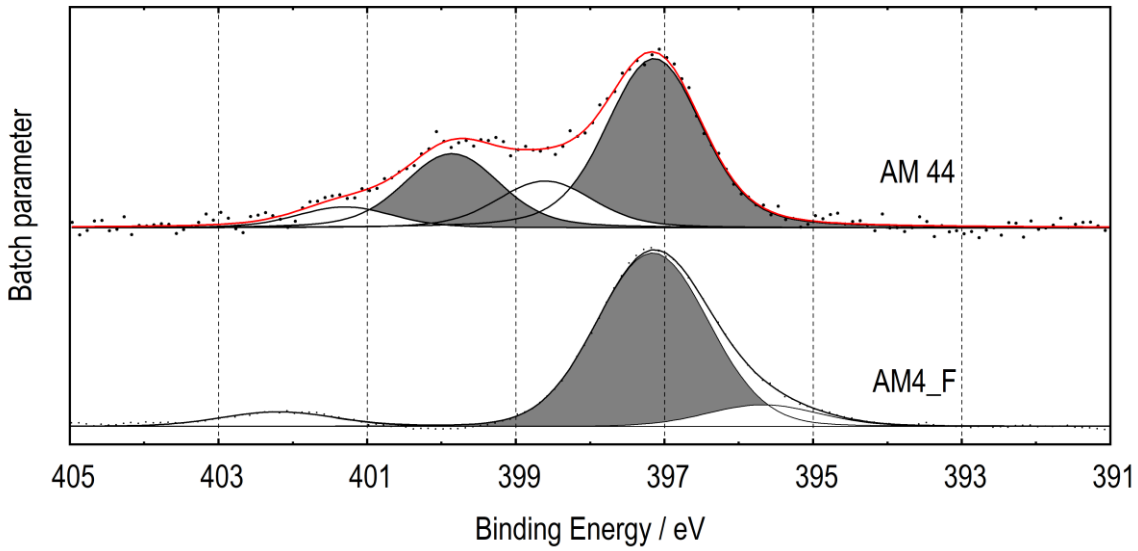

Spectrum 31: Comparison of N1s peaks of AM44 and AM4_F

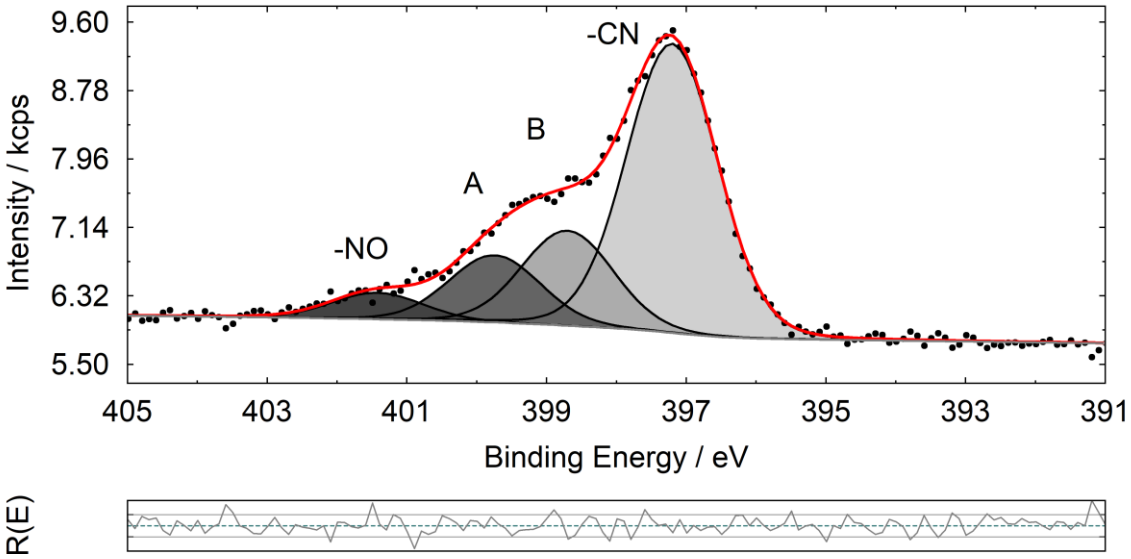

Spectrum 32: N 1s peak of AM41

In spectrum 31 a small shift on the BE of –NO in AM44 it's observable. For the comparison a subtraction of the background and a normalisation of the height of the main peak to 1 have been made. Moreover a charge correction to 397.2 eV of –CN group was necessary for a better visualisation of the new appearing peaks. As a matter of fact, it's not possible to assign these two peaks from literature reference. The most probable interpretation is the following:

Peak A. During the discharging process, NO linear undergoes a redox process that leads to NO bent. So the idea is that the peak at 400 eV is the bent form while the one at 402 eV is the linear form, present also in the uncycled material.

Peak B. The redox mentioned above is possible thanking the lithium insertion process. So this peak might be assigned to a nitrogen that interacts with Li^+.

In spectrum 33 all the N 1s signals of AM1 set are plotted in order to visualise the differences. Of course also in this case, normalisation and charge correction have been needed. In spectrum 34 all N 1s signals of cycled materials are displayed, the results of the quantitative analysis are the reported on tables 28.

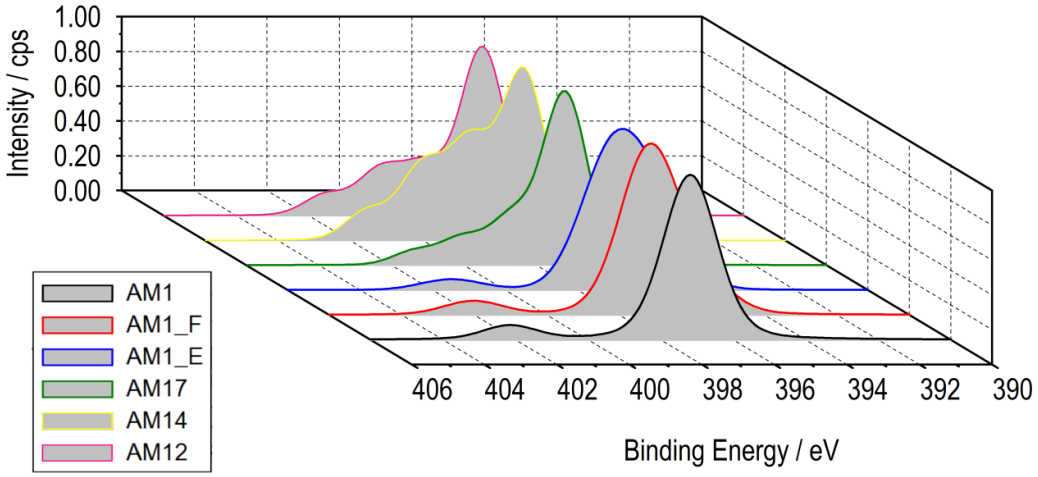

Spectrum 33: all N 1s signals of AM1 set

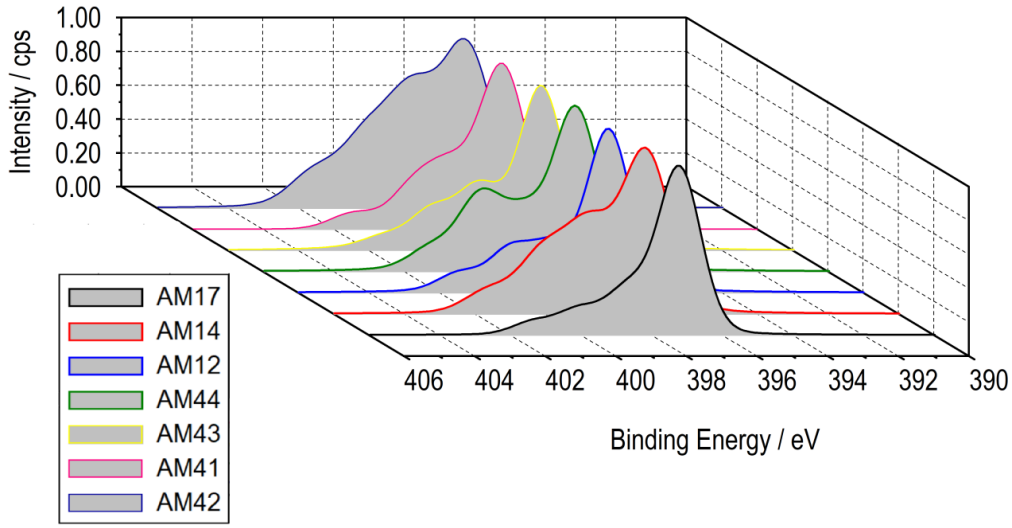

Spectrum 34: all N 1s signals of cycled materials

Table 29: quantification of N 1s for cycled samples

Sample ID	State of charge	N of cycles	-CN	B	A	-NO
AM44	Charged	22	54,66	14,99	23,83	6,52
AM43	Discharged	51	63,18	20,36	12,78	3,68
AM41	Charged	64	59,62	19,91	14,68	5,79
AM42	Charged	114	44,2	28,88	17,87	9,05
AM17	Discharged	3	67,94	17,35	9,63	5,08
AM14	Discharged	143	50,46	25,36	17,59	6,59
AM12	Charged	180	63,63	14,76	15,02	6,59

Since the tendency are not easily summarised by table 29, figure 18 has been provided.

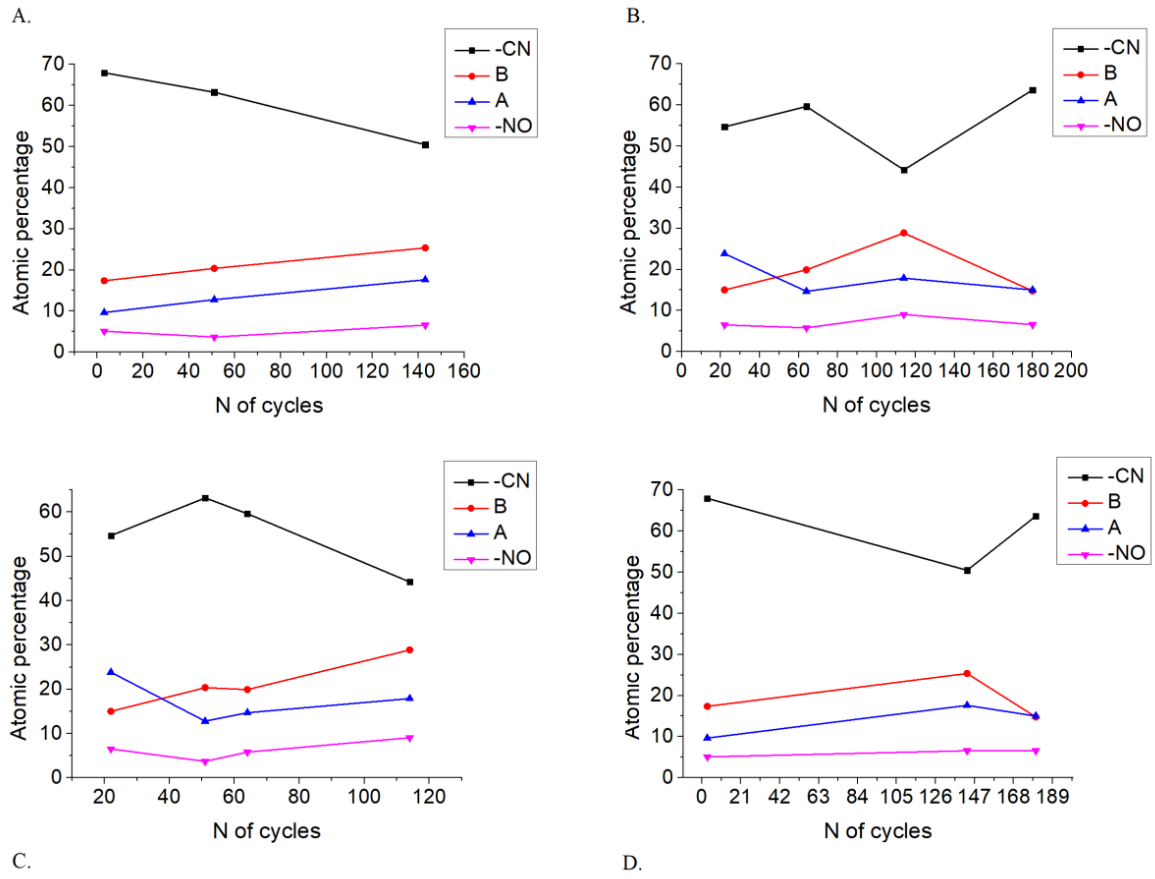

Figure 18: Tendency for table 28 with differences in focus:

A. focus on discharged samples
B. focus on charged samples
C. AM4 set
D. AM1 set

It's easy to observe from the curves the correlation between –CN and B trend. This is probably due to the fact that the nitrogen that interacts with lithium is from the –CN

group and not from –NO one. This idea is suggested also from the quantitative analysis that gives back a ratio of around 5/6 for –CN and 1/6 for –NO.

4.2.5.1 Sputtering process

Depth profiling uses an ion beam to etch layers of the surface, revealing bulk information. Combining a sequence of ion gun etch cycles with XPS analyses provides quantified information. Before removing material from the sample, a set of spectra is recorded from the surface of the sample. The surface is etched by impinging an ion beam over an area of the sample. After the etch cycle, the ion beam is blanked and another set of spectra is recorded. This sequence of etching and spectrum acquisition is repeated until profiling has proceeded to the required depth.

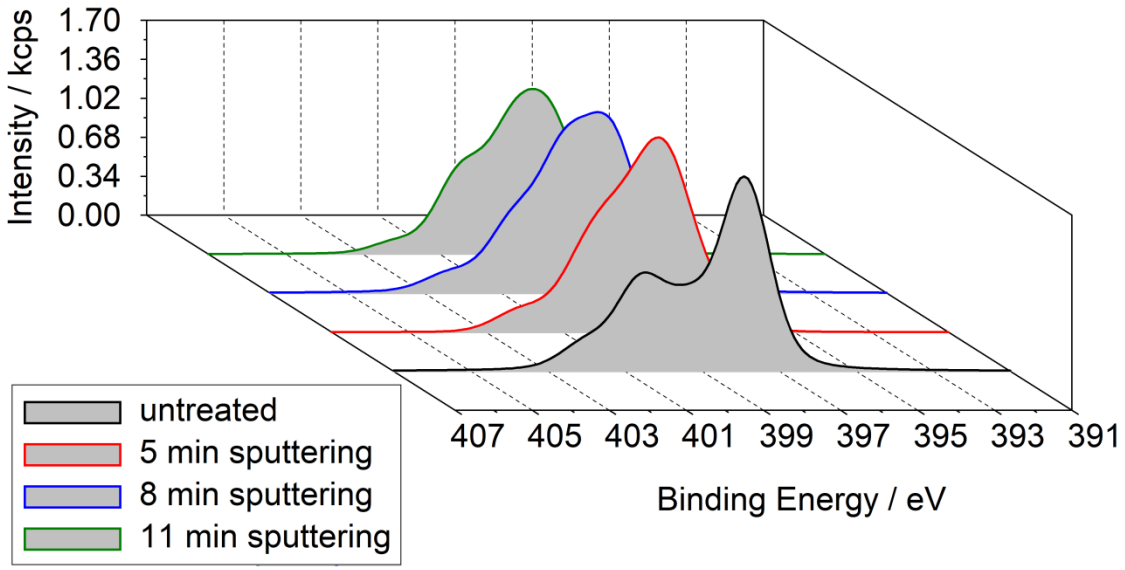

Spectrum 35: N 1s peaks for sputtering of AM44

In spectrum 35, it's possible to observe a deep modification of the signals during sputtering cycles. Peak A and B tend to grow in intensity.

In order to visualise how the different peaks are changing with the depth, figure 19 has been produced.

The reaction equation to be considered is:

$$Cu^{II}Fe^{III}(\mathbf{NO})_{\mathbf{linear}}L_5 + xe^- + xLi^+ \underset{\text{charge}}{\overset{\text{discharge}}{\rightleftarrows}} Li_xCu^{I}Fe^{II}(\mathbf{NO})_{\mathbf{bent}}L_5$$

Comparing the surface untreated and after 11 minutes the data are completely consistent for discharged samples. For AM17 and AM43 B tends to increase, A is basically stable in percentage while –CN and –NO groups decrease. For charged samples (AM12, AM41 and AM44), the behaviour is somewhat similar to discharged. This is still in good agreement considering the fact that the measure has been made on the opposite side with respect to the insertion process. Moreover, it's possible to think that, with high number of cycles (>100), the material has undergone an irreversible modification (a capacity loss is registered in previous work [38]).

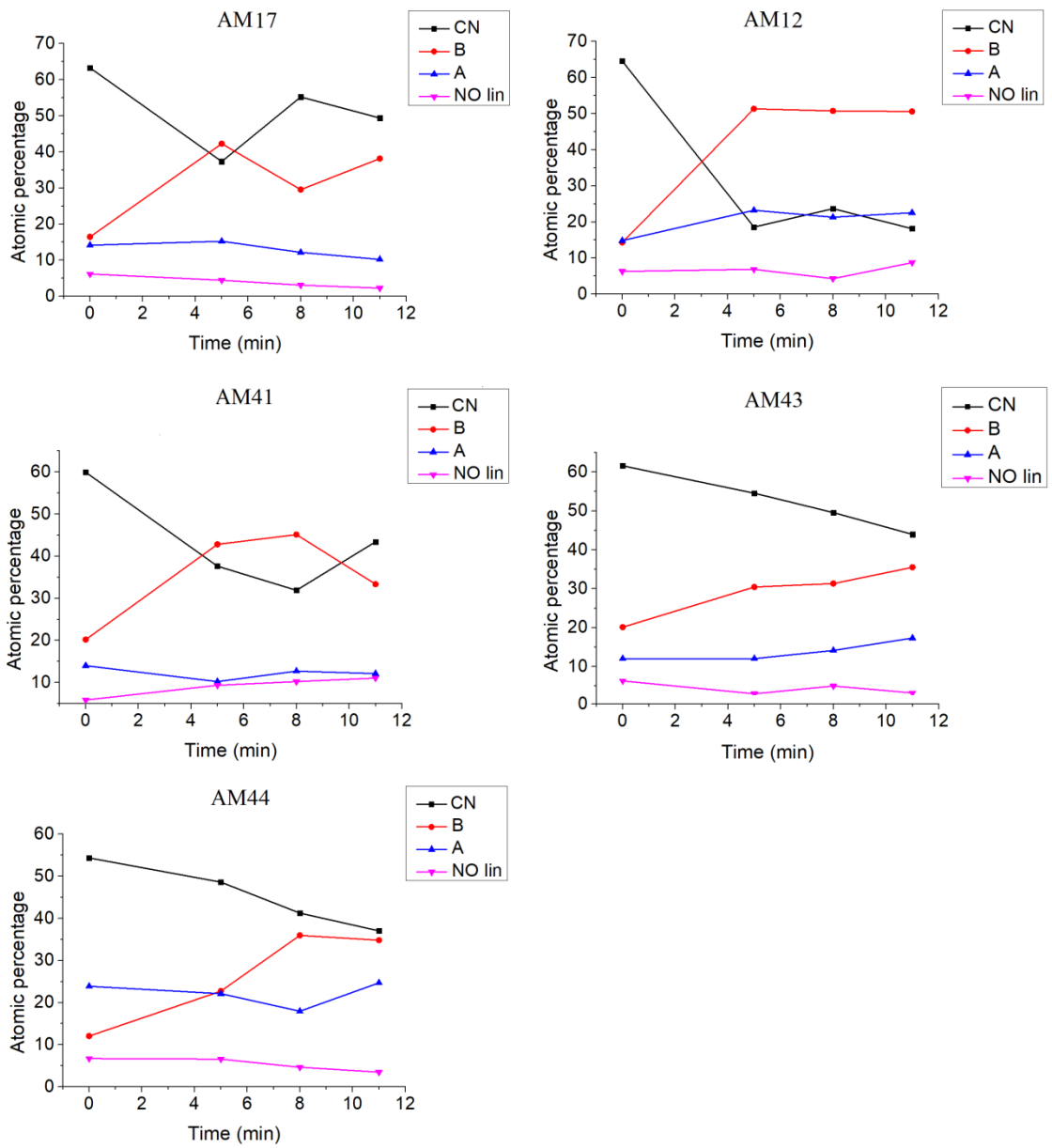

Figure 19: Depth profile trend for different samples from AM1 set and AM4 set

4.2.6 Depth profiling

A depth profiling has been made in order to gain information about the bulk conditions. N 1s has been excluded since it has already been analysed in section 4.2.5.1.

The trend is the same for all the investigated elements. One example from AM1 and one from AM4 are reported.

For both AM17 and AM41, Cu 2p has been chosen to represent the greatest changes (spectrum 36 and 37).

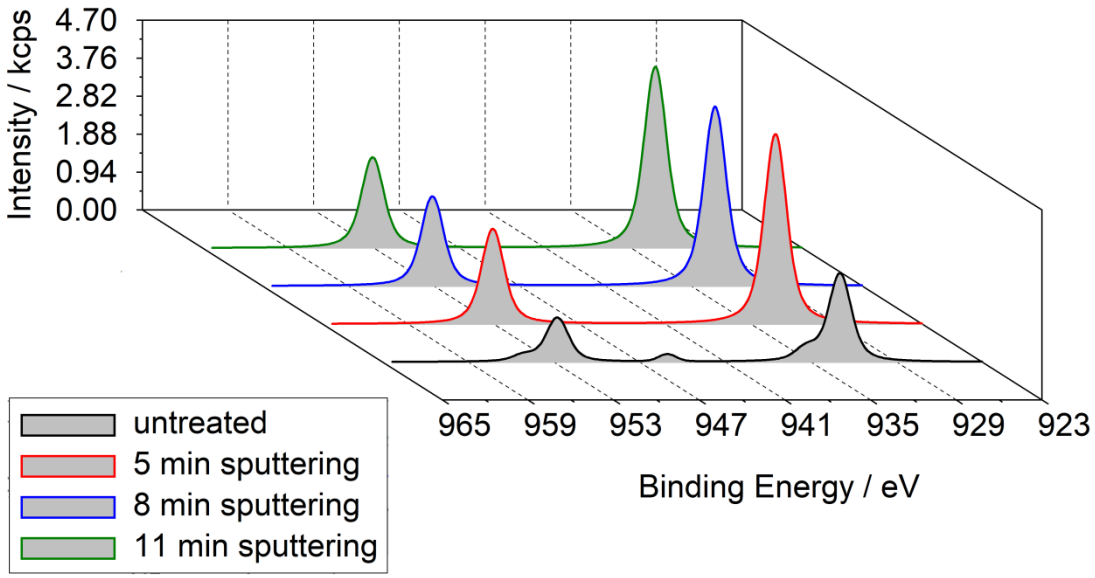

Spectrum 36: Cu 2p peaks for sputtering of AM17

Table 30: Depth profiling value for AM17

Time	C	O	Li	P	F	Cu	Fe
0	27,07	26,88	18,04	19,21	21,47	15,84	13,08
5	24,33	24,79	24,91	22,1	24,36	25,71	27,66
8	24,32	24,75	27,59	27,4	26,14	28,42	29,14
11	24,28	23,58	29,47	31,29	28,03	30,04	30,12
	100	100	100	100	100	100	100

For a better visualisation of the trend described in table 30, see figure 20.

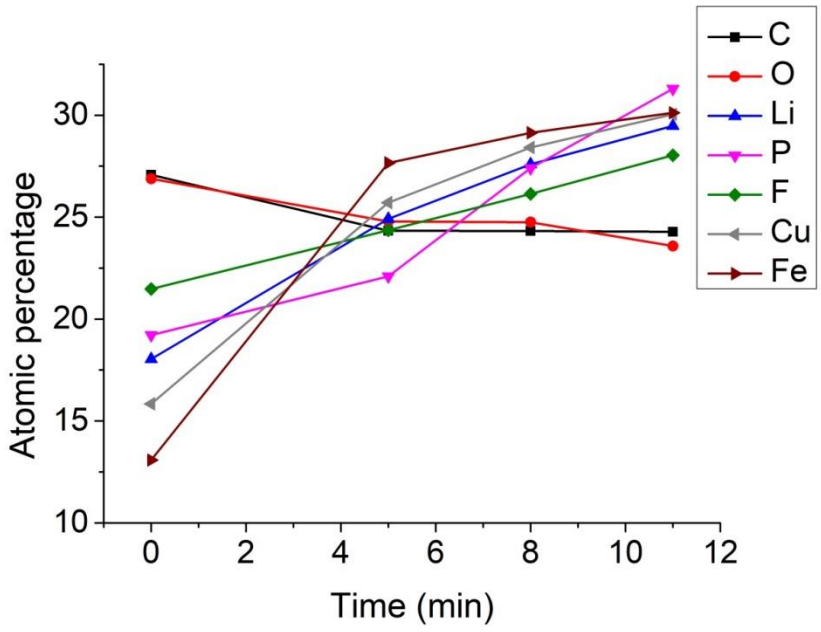

Figure 20: Depth profiling trends for AM17

From table 30 and figure 20, an increase in Li, F and P can be observed just below the surface, while the C and O content is decreasing. This indicates the existence of different layers in the surface film, where some species are formed closer to the electrode surface than others.

One could think that an higher concentration of lithium can be found deeper in the electrode. This feature can be explained thanks to the coexistence of two effect: a good insertion process and, as mentioned above, the measure has been made on the opposite side of the cathode with respect to the one that was in contact with the electrolyte (figure 17).

Fe and Cu increase as more of the bulk electrode is exposed. Moreover since AM17 is a discharged electrode, it's remarkable to notice that going deeper in the bulk just Cu^{+} is observable. Probably this might lead to the idea that the bulk is more likely Cu^{+} as my be expected on a discharged electrode, so that the changes observed are just superficial and not bulk.

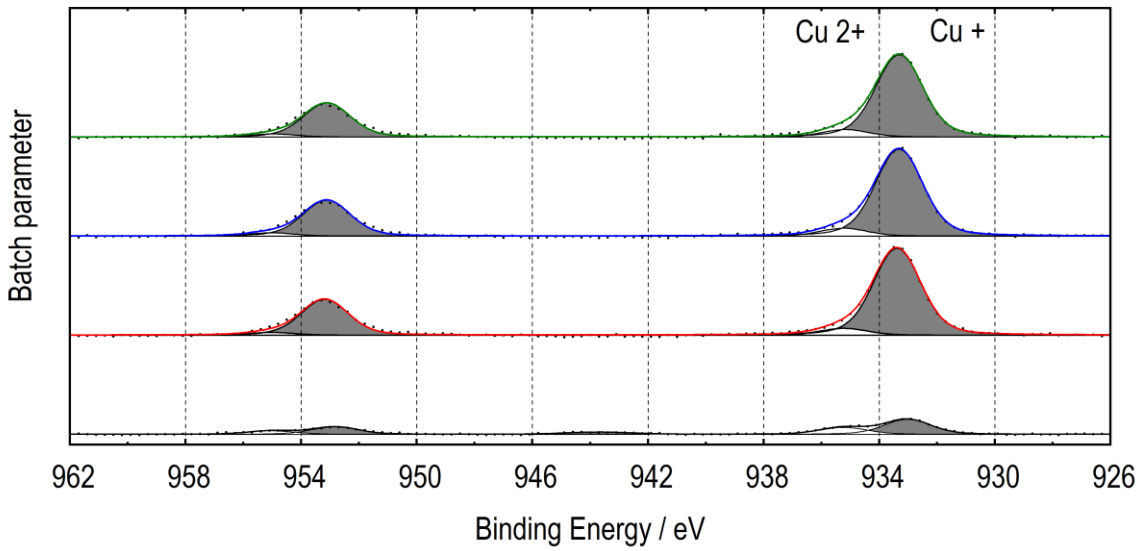

Spectrum 37: Cu 2p peaks for sputtering of AM41. Black curve is the sample untreated (=0min sputtering), the red curve is 5 min sputtering, the blue curve is 8min sputtering and, finally, the green curve is 11 min sputtering.

Table 31: Depth profiling value for AM41

Time	C	O	Li	F	Cu	Fe
0	26,14	28,72	12,54	21,95	8,31	10,97
5	25,36	24,94	28,19	25,41	30,9	29,82
8	24,83	23,46	29,06	26,27	31,22	30,25
11	23,67	22,88	30,21	26,37	29,57	28,96
	100	100	100	100	100	100

For a better visualisation of the trend described in table 31, see figure 21.

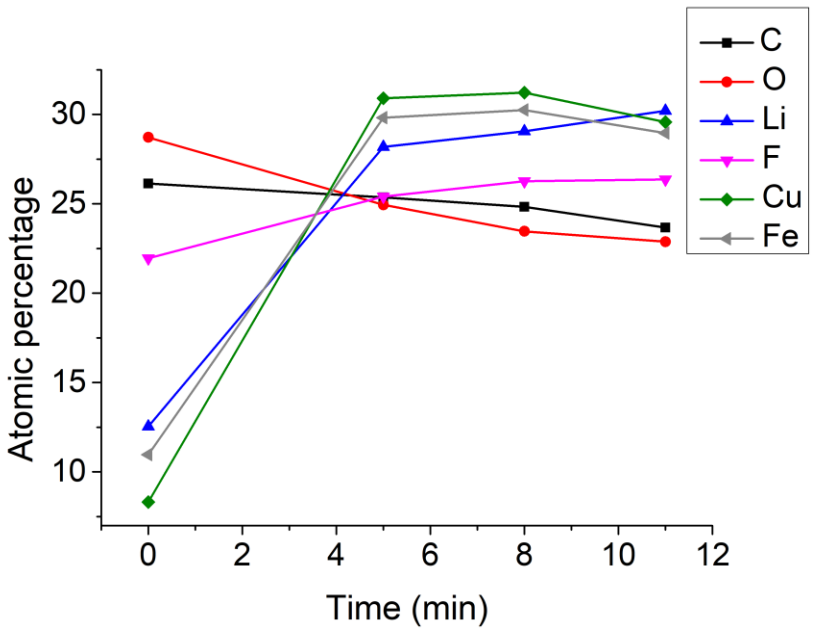

Figure 21: Depth profiling trends for AM41

The same considerations done for AM17 are valid. Observing spectrum 37, table 30 and figure 21, it's interesting to notice that for AM41, a charged material, after a great decrease in Cu^{2+} from the first layer to the second one, an increasing amount of Cu^{2+} is visible during sputtering, it would have been interesting to have sputtered more layer to verify the trend. Moreover, it's possible to see that the layer investigated with 11 min sputtering reveals a decrease in content of Cu and Fe, this might be another data to support the idea that different layers can be different in terms of composition, however that's also true that an error of 10% relative should be taken into account, reviling that this change could also be not relevant.

4.2.7 Decomposition of the electrolyte

Surface-film formation on cathodes and its influence on battery performance has also been studied. When using the $LiPF_6$ salt, these compounds are typically: LiF, Li_xPF_y and $Li_xPO_zF_y$. [44] The electrolyte solution is thermodynamically unstable at low and very high potentials. Hence, on first charge of the cell the electrolyte solution begins to reduce/degrade on the surface and forms the SEI. There are competing and parallel solvent and salt reduction processes, which result in deposition of a number of organic and inorganic decomposition products on the surface. [39]

The more probable reactions are [48] [49]:

- $LiPF_6 + xe^- + xLi^+ \rightarrow LiF + Li_xPF_y$
- $H_2O + LiPF_6 \rightarrow LiF + POF_3 + 2HF$
- $PF_6^- + 2e^- + 3Li^+ \rightarrow 3LiF + PF_3$
- $LiPF_6 \leftrightarrow LiF + PF_5$
- $H_2O + PF_5 \rightarrow POF_3 + 2HF$
- $PF_5 + 2xe^- + 2xLi^+ \rightarrow xLiF + Li_xPF_{5-x}$
- $POF_3 + 2xe^- + 2xLi^+ \rightarrow xLiF + Li_xPOF_{3-x}$
- <u>EC solvent:</u> $2\,(CH_2O)_2CO + 2e^- + 2Li^+ \rightarrow (CH_2OCO_2Li)_2 + C_2H_4$
  $(CH_2O)_2CO + 2e^- + 2Li^+ \rightarrow Li_2CO_3 + C_2H_4$
- <u>DMC solvent:</u> $CH_3OCO_2CH_3 + e^- + Li^+ \rightarrow CH_3OCO_2Li + CH_3\cdot$
  $CH_3OCO_2CH_3 + e^- + Li^+ \rightarrow CH_3OLi + CH_3CO_2\cdot$
- <u>PC solvent</u>: $2\,CH_3(CH_2O)_2CO + 2e^- + 2Li^+ \rightarrow (CH_2OCO_2Li)_2 + C_3H_7$
  $CH_3(CH_2O)_2CO + 2e^- + 2Li^+ \rightarrow Li_2CO_3 + C_3H_7$

O 1s, F 1s, P 2p and Li 1s signals are useful tools to observe qualitatively these products (see spectra from 38 to 41).

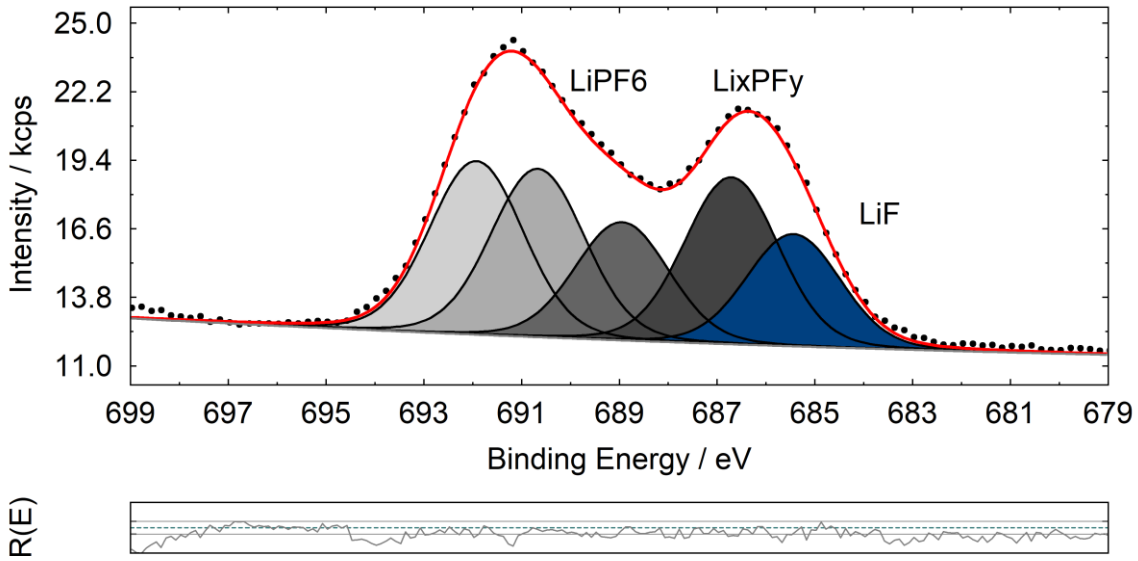

Spectrum 38: fitted F 1s signal for AM14

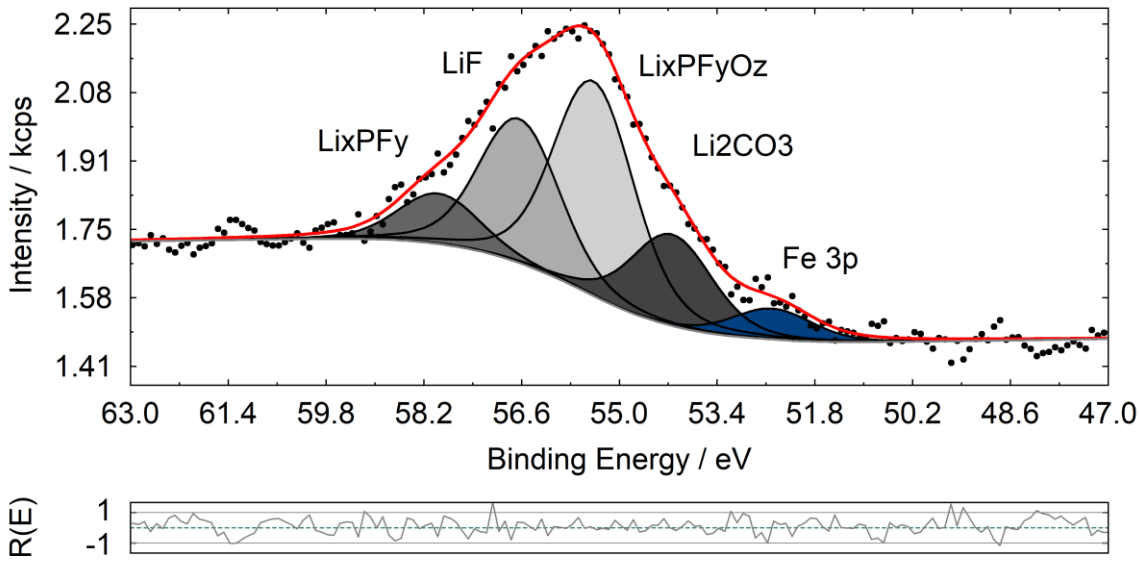

Spectrum 39: fitted Li 1s signal for AM14

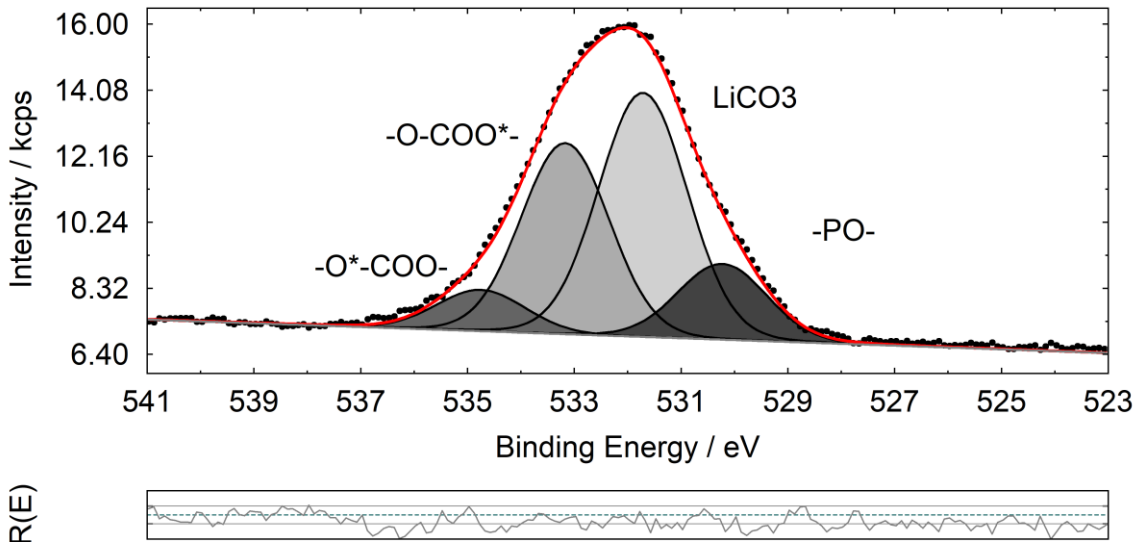

Spectrum 40: fitted O 1s signal for AM14

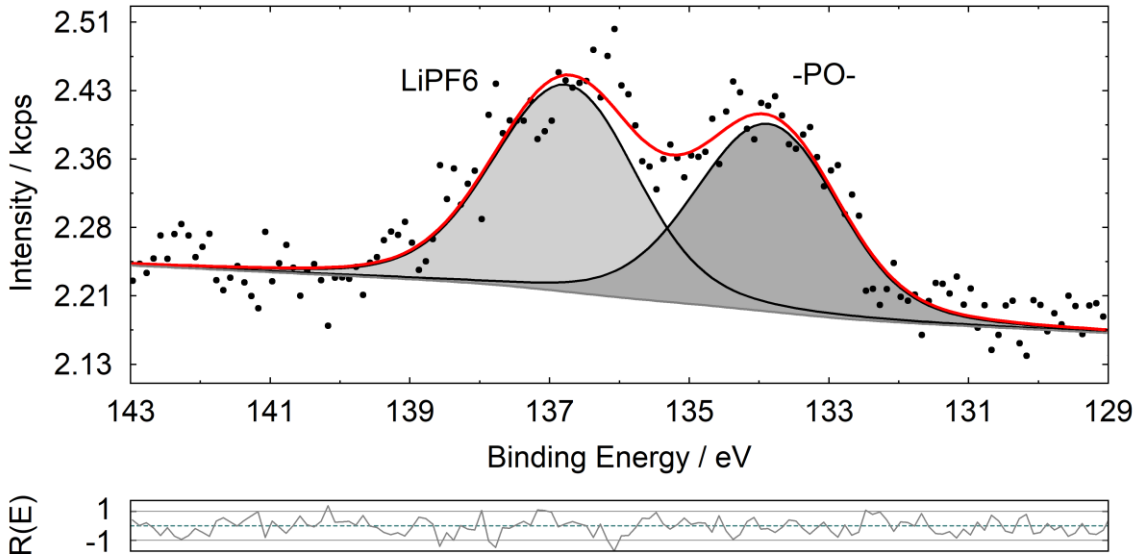

Spectrum 41: fitted P 2p signal for AM14

The amount of surface material tends to increase with cycles number as can be shown from LiF spectra from AM4 set of materials as presented in spectrum 42.

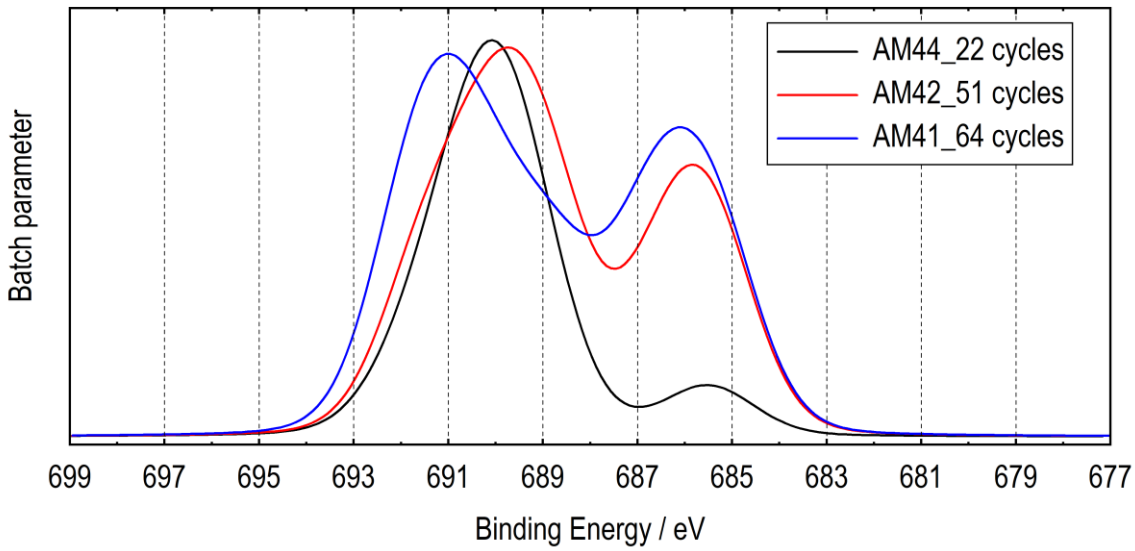

Spectrum 42: F 1s signals from AM4 set

This suggests that the layer formed on the cathode is not dense enough to serve as a sufficient barrier between electrolyte and the environment close to the cathode surface. Fresh electrolyte is transported to the electrode surface and oxidation continues with time, moreover the ratio of decomposition products are changing. This is in contrast to the typical SEI layer formed on anode, during the first discharge covers the electrode surface so as to prevent further reduction of the electrolyte in subsequent cycles.

The cathode surface layer could thus be termed Solid Permeable Interface (SPI) rather than an SEI, which implies a passivated surface. [49] The cathode/electrolyte interface can limit cell performance by consuming electrolyte as cycling progresses.

4.2.8 Air modification

All the samples except AM16 have been exposed to air, probably causing some modification of the surface. AM16 coin cell was disassembled in a glove box, transported with a schlenk and inserted on the XPS under N_2 flux. General information: 1000 cycles at C rate (not operating well), then 73 cycles at C/5 rate and the final state is charged.

Since the air exposure is supposed to modify the state of charge of the sample and also decomposition product of the electrolyte a comparison with AM12 and AM14 has been done.

While C 1s, O 1s, Fe 2p and Cu 2p seem to be really similar, P 2p and F 1s are not. As far as Li 1s is concerned, it's hard to properly say if any modification has happened due to a bad signal to noise ratio. Spectra 43 and 44 show the changes due to air contact.

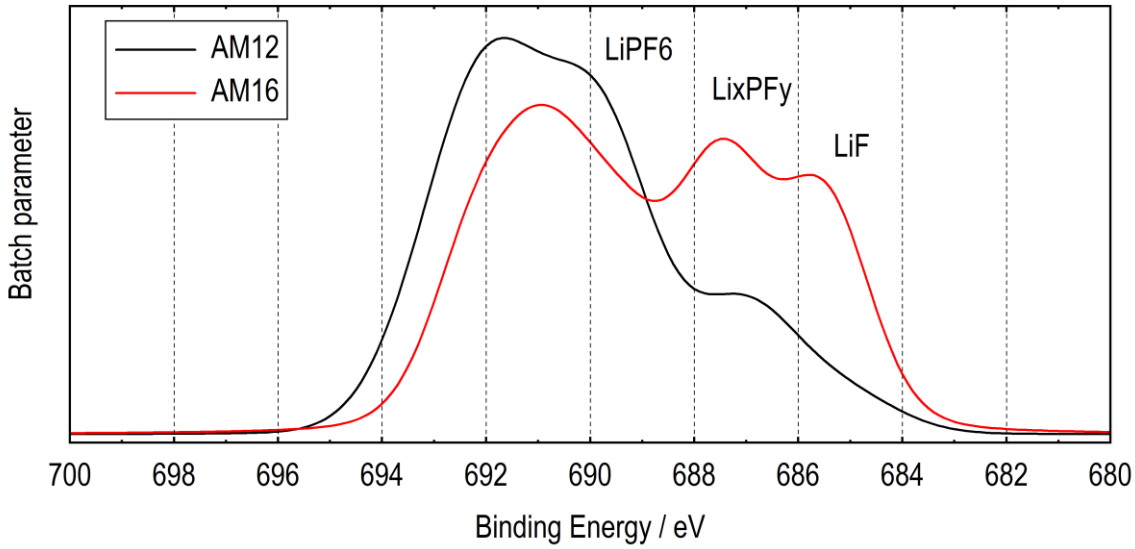

Spectrum 43: Comparison of F 1s peaks coming from AM12 and AM16

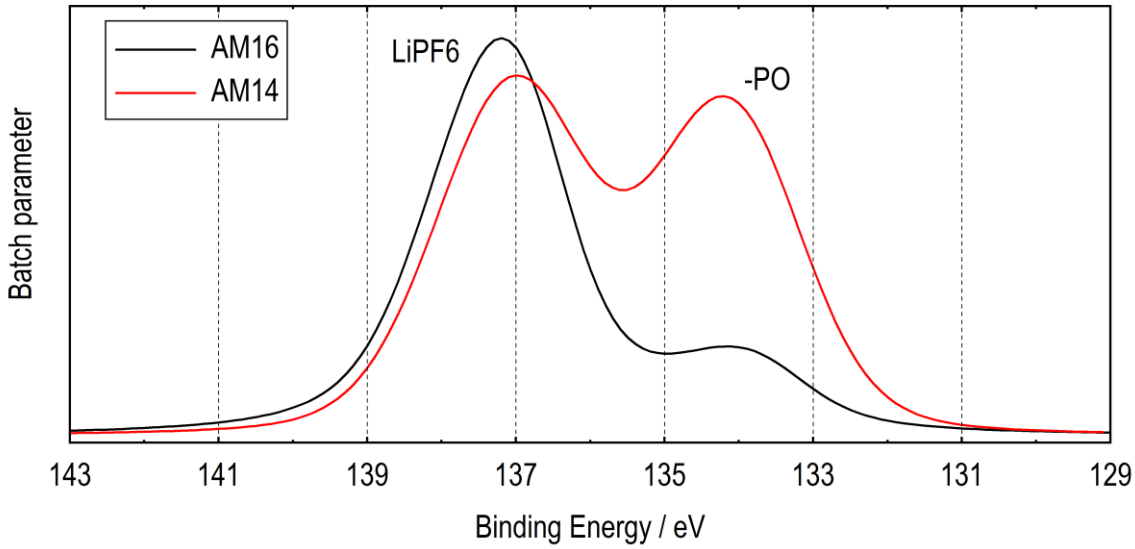

Spectrum 44: Comparison of P 2p peaks coming from AM14 and AM16

Two factors need to be considered while interpreting these spectra: AM16 went through a long degassing process (almost 3 days) in UHV before it was possible to measure. All the other cycled needed no more than 3 hours. This possibly was because of the storage: in two or three months of air contact there is a high possibility that the degassing process was already done before inserting in XPS. Moreover the air might have led to prevalent oxidised decomposition products such as –PO ones. (spectrum 44) Probably the increased percentage of decomposition products might also be due to the higher number of cycles done in spectrum 43.

4.3 SEM measurement

AM1 powder mainly comprises heterogeneous crystals: different in shape and size, probably due to co-precipitation method for synthesis. Crystals appear to be sharp, with clean break points. (figure 22, AM1)

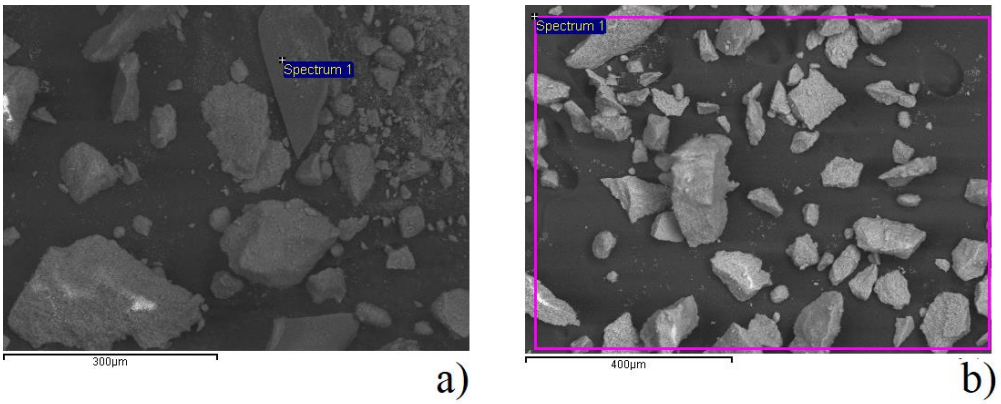

Figure 22: Typical SEM micrographs of AM1 . Zoom at a) 300 µm and b) 400 µm

Table 32: AM1 quantitative analysis

Element	Weight %	Atomic %
C K	21.71	43.63
N K	15.29	26.36
O K	3.98	6.00
Si K	0.26	0.22
Fe K	28.07	12.13
Cu K	30.69	11.66

From table 32, it's possible to notice that the ratio between iron and copper is 1.4/1. From XPS it was 1.1 and XRF [38] was 1.5. The data are in really good agreement. Silicon is present in low percentage. Oxygen seems to be less than expected, zooming on a crystal the percentage arise to the right ratio.

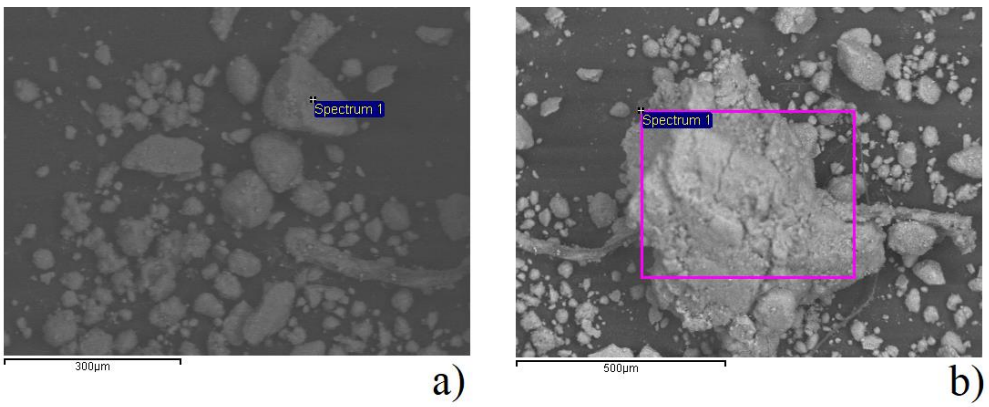

Figure 23: Typical SEM micrographs of AM4 . Zoom at a) 300 µm and b) 500 µm

AM4, instead, has spherical particles (see Fig. 23). These are irregular shaped with rounded edges.

Table 33: AM4 quantitative analysis

Element	Weight %	Atomic %
C K	33.88	65.21
N K	3.72	6.14
O K	4.06	5.86
Fe K	31.14	12.89
Cu K	27.21	9.90

From table 33, it's possible to notice that the ratio between iron and copper is 1.3/1. From XPS it was 1.1 and XRF [38] was 1.0. These results are consistent.

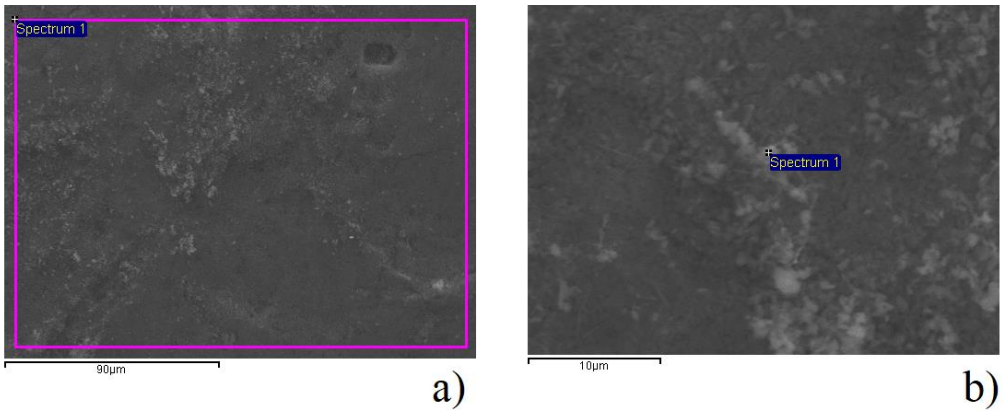

Figure 24: Typical SEM micrographs of AM1_F. a) Zoom at a) 90 µm and b) 10 µm

The first imagine of figure 24 shows cracks in the cathode. This is probably caused by the milling process. The material appears to be a compact structure.

Table 34 summarises the quantitative analysis for AM1_F.

Table 34: AM1_F quantitative analysis

Element	Weight %	Atomic %
N K	23.51	42.17
O K	8.31	13.05
F K	17.85	23.59
Fe K	23.86	10.73
Cu K	26.47	10.46

The ratio between iron and copper is basically 1:1. Also in this case in good agreement with XPS measurement.

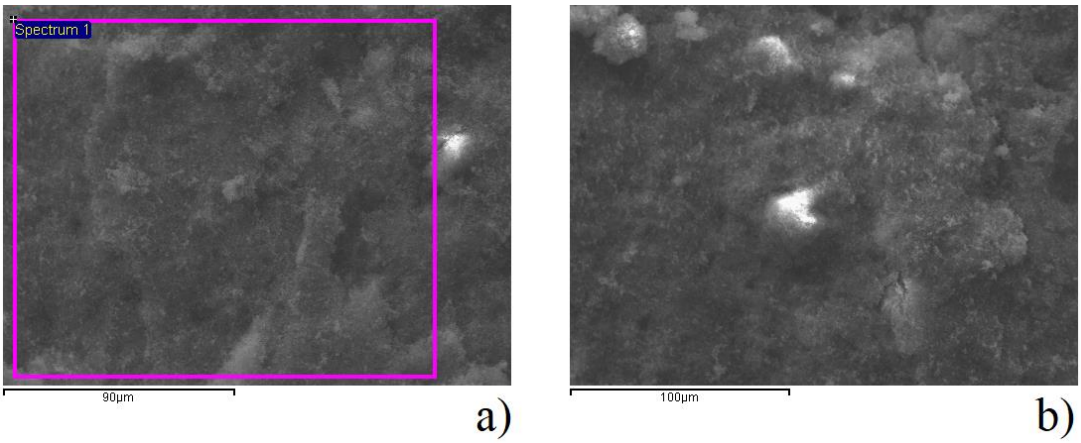

Figure 25: Typical SEM micrographs of AM4_F. a) AM4_F after XPS measurement b) AM4_F untreated

Both of the pictures in figure 25 are from AM4_F but there is a difference: the first imagine is a sample that was measured by XPS, the second was a totally untreated one. Morphologically speaking, not many differences are observed. Moreover these two samples are really similar to AM1_F one. Quantitative analysis is reported for both samples in table 35 and 36.

Table 35: AM4_F (XPS) quantitative analysis

Element	Weight %	Atomic %
C K	30.88	44.49
N K	27.05	33.42
O K	6.39	6.91
F K	7.77	7.08
Fe K	13.36	4.14
Cu K	14.53	3.96

Table 36: AM4_F (untreated) quantitative analysis

Element	Weight %	Atomic %
N K	22.66	48.58
O K	7.26	13.62
F K	2.31	3.65
Fe K	32.63	17.55
Cu K	35.13	16.60

From table 34 and 35 it's possible to notice that Fe/Cu ratio is 1:1 in both cases.

Basically, considering that carbon wasn't detected for AM4_F untreated, no main differences can be seen before and after XPS measurement, meaning that the modification of the material is just on oxidation state level, and no major damage is done at the material while measuring.

For cycled samples, all the measurements were recorded on the side that was in contact with the separator (soaked with electrolyte).

This was possible since SEM-EDX is more bulk technique (the escape depth is larger in comparison to XPS). (figure 26)

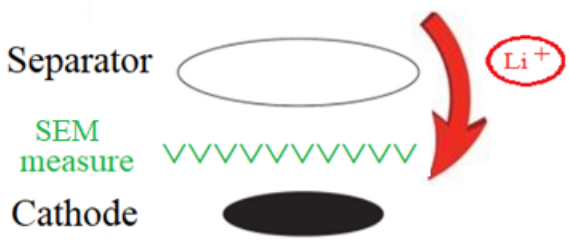

Figure 26: Experimental assets of SEM measure

In figure 27, micrographs from cycled samples are reported:

a) AM11: charged, beginning of cycling.
b) AM15: charged, several cycles
c) AM45: discharged, beginning of cycling
d) AM47: discharged, several cycles

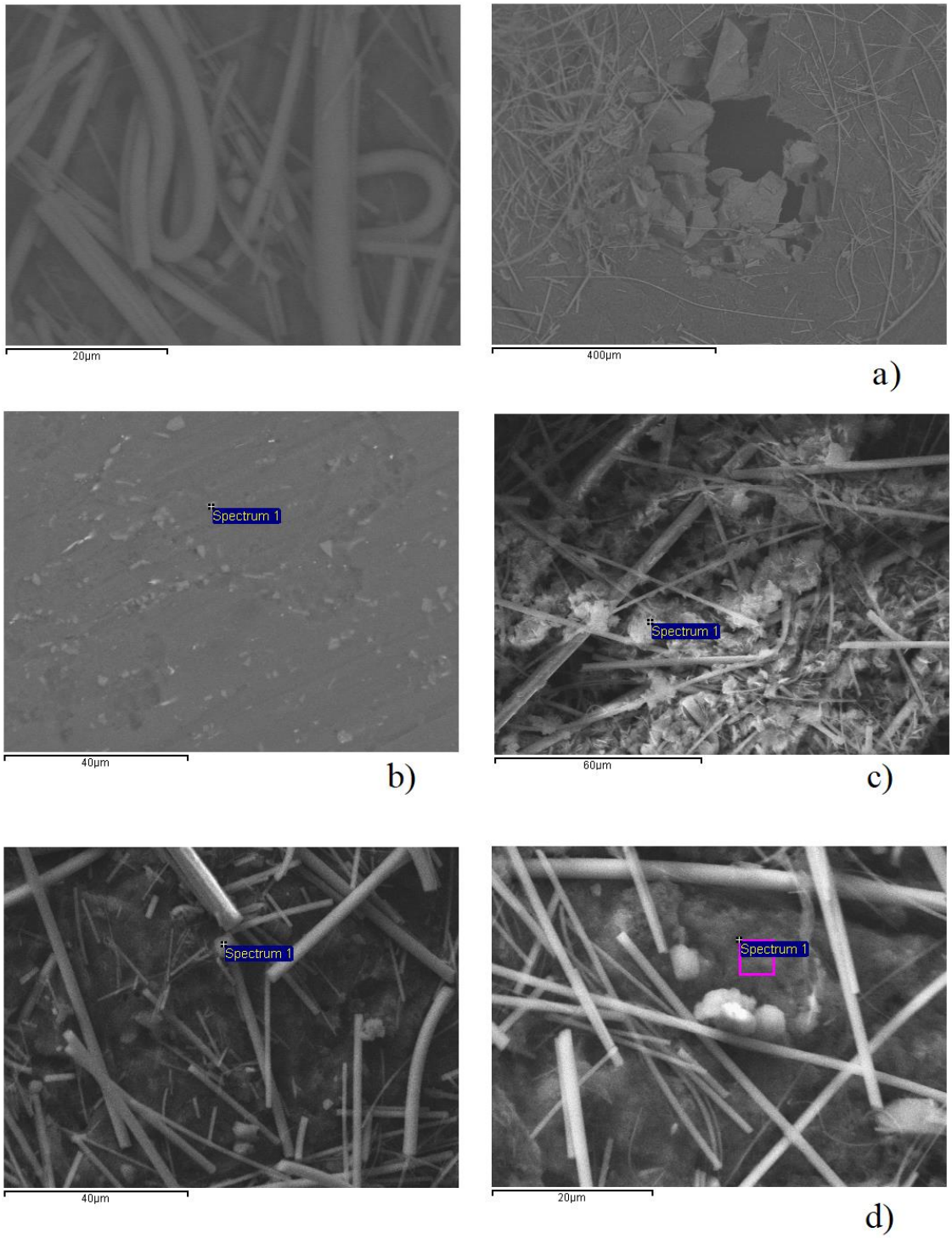

Figure 27: SEM micrographs of a) AM11 b) AM15 c)AM45 and d)AM47

As far as concern AM11, carbon fibers are really easy to notice. Glass fibers are also present, probably coming from the separator. AM1 seems to be homogenously distributed. In the second picture it's possible to observe a hole on the material, probably due to the removal process from the cathode. AM15 was disposed on the opposite side (same asset of XPS measurement) since it was stored with Kapton. A lot of cracks are

visible: probably caused by treatment after cycles. AM45 is similar to AM11; it's possible to notice the active material as spherical particles. Finally, AM47 resembles AM45: carbon fibers and spherical particles are present.

Table 37: Quantitative analysis for cycled samples

Sample	Element	Weight %	Atomic %
AM11	Al K	23.95	41.78
	Fe K	18.41	15.52
	Cu K	57.64	42.70
AM15	C K	34.17	58.86
	O K	14.00	18.11
	F K	4.42	4.81
	Mg K	0.14	0.12
	Si K	1.11	0.81
	P K	0.18	0.12
	S K	0.39	0.25
	Cl K	0.16	0.09
	Ca K	0.24	0.13
	Fe K	44.22	16.38
	Cu K	0.98	0.32
AM45	C K	31.61	41.94
	O K	37.07	36.93
	F K	18.69	15.68
	Na K	1.35	0.94
	Al K	0.34	0.20
	Si K	3.21	1.82
	P K	1.50	0.77
	K K	0.25	0.10
	Ca K	0.12	0.05
	Fe K	2.98	0.85
	Cu K	2.87	0.72
AM47	C K	31.07	39.28
	N K	6.32	6.85
	O K	45.51	43.19
	F K	9.60	7.68
	Na K	0.81	0.54
	Al K	0.16	0.09
	Si K	1.36	0.74
	P K	1.16	0.57
	K K	0.09	0.03
	Fe K	3.10	0.84
	Cu K	0.82	0.20

In table 37, it's possible to see the quantitative analysis for the for cycled samples mentioned above. For AM 11, Cu content is way higher than Fe one. Probably the area investigated was copper rich while F, P ($LiPF_6$) are present in low concentration, not easy to detect. In AM15, phosphorus is again signal of electrolyte presence ($LiPF_6$). In this case the investigated area was iron rich, while the content of copper is really low. Moreover for AM45 the ratio between iron and copper is basically 1:1. P and F are still detectable. Finally for AM47 an high content of elements related to the separator are present. It's possible that it was not removed properly. Copper is less than iron. Phosphorus is again present.

CHAPTER 5: CONCLUSIONS AND SUGGESTIONS FOR FUTURE WORK

This work has been an effort to obtain a deeper understanding of the chemistry of the surface of copper nitroprusside in its application as a positive electrode in a Li-ion battery: it has provided some insights into the chemical composition and morphology of surface film formed at ambient temperature and under air exposure.

XPS has shown to be a useful technique if used in a careful way, providing chemical information on the layers formed on electrode surfaces. Firstly, an accurate measure of the transmission function at the decided pass energy is necessary in order to avoid major errors, then peaks should be assigned using cautious selection of references.

A separation of the morphology information from the various surface layers could be achieved by careful peak assignment and sputtering calibration, showing a stratification of different layers with an univocal trend. The sputtering process was really useful since it has confirmed the expected fashion due to the insertion process. The methodology can be of course employed for other electrode and electrolyte systems.

UHV and X-ray beam convey modifications on the oxidation states of metals centres of the material. XPS measurement should be run as fast as possible in order to limit the greatness of these changes. The calibration done for this materials was also a powerful method to overcome this issue, allowing a rough idea of the initial material. In situ measurement might be the solution of this kind of problem or also near ambient pressure XPS.

Surface films are definitely formed on CuNP cathodes cycled and stored in a 1M $LiPF_6$, PC/EC/DMC electrolyte. This film of mostly electrolyte decomposition products, consists mainly of organic/polymeric species and LiF, increases with cycles. The simultaneous increase in organic layer thickness (this is just a guess justified by the fact that iron and copper disappear from the surface with an increased number of cycles) and in amount of LiF attached to the surface may be responsible, for at least in part, for the power-fade and capacity loss exhibited by Li-ion cells involving this cathode.

Moreover, air provokes some changes on the surface chemistry as far as concerns decomposition product of the electrolyte (-POF oxidised species are mainly formed) and can also have an impact on state of charge of the sample. For the future it might be

necessary to create a particular asset for XPS, for example to adjust a transfer chamber between XPS and the glove box where the coin cell is disassembled.

Surface phenomena are factors that definitely must be taken more into account in selecting materials for practical Li-ion batteries.

CHAPTER 6: BIBLIOGRAPHY

1. W. C. Rontgen, “On a new kind of rays,” Nature, vol. 1369, no. 53, pp. 274–276, 1896.
2. M. Giorgetti, “ A Review on the Structural Studies of Batteries and Host Materials by X-Ray Absorption Spectroscopy” ISRN Materials Science, Volume 2013 (2013), 22 pages.
3. D. M. Hercules and S. H. Hercules, “Analytical Chemistry of Surfaces” Journal of Chemical Education pp. 402-409.
4. Hofmann, Siegfried “Surface and Interface Analysis”. Kirk-Othmer Encyclopedia of Chemical Technology, 24, 71–118.
5. D. M. Hercules and S. H. Hercules, “Analytical Chemistry of Surfaces” Journal of Chemical Education pp. 483-489.
6. Watts, J. F. (1994). X-ray photoelectron spectroscopy. Vacuum, 45(6–7), 653–671.
7. R. Denecke, lecture notes.
8. Kiani, M. A., Mousavi, M. F., & Rahmanifar, M. S. (2011). “Synthesis of nano- and micro-particles of LiMn2O4: Electrochemical investigation and assessment as a cathode in li battery.” International Journal of Electrochemical Science, 6(7), 2581–2595.
9. Tarascon, J. M., & Armand, M. (2001). “Issues and challenges facing rechargeable lithium batteries.” Nature, 414(6861), 359–67.
10. V. Colin and B. Scrosati, Modern Batteries. 1997.
11. Dominey, L. A. “Current state of the art on lithium battery electrolytes” Industrial Chemistry Library Vol. 5 (ed. Pistoia, G.) 137–165 (1994).
12. M. Dahbi, F. Ghamouss, F. Tran-Van, D. Lemordant, and M. Anouti, “Comparative study of EC/DMC LiTFSI and LiPF6 electrolytes for electrochemical storage,” Journal of Power Sources, vol. 196, no. 22, pp. 9743–9750, 2011.
13. R. W. Schmitz, P. Murmann, R. Schmitz, R. M¨uller, L. Kr¨amer, P. Isken, P. Niehoff, S. Nowak, G. V. Röschenthaler, N. Ignatiev, P. Sartori, Passerini, M. Kunze, A. Lex-Balducci, C. Schreiner, I. Cekic-Laskovic, and M. Winter, “Investigations on novel electrolytes, solvents and SEI additives for use in

lithium-ion batteries: Systematic electrochemical characterization and detailed analysis by spectroscopic methods," Progress in Solid State Chemistry, vol. 42, no. 4, pp. 65–84, 2014.

14. R. Ruffo, C. Wessells, R. a. Huggins, and Y. Cui, "Electrochemical behavior of LiCoO2 as aqueous lithium-ion battery electrodes," Electrochemistry Communications, vol. 11, no. 2, pp. 247–249, 2009.
15. Verma, Pallavi, Pascal Maire, and Petr Novák. "A review of the features and analyses of the solid electrolyte interphase in Li-ion batteries." Electrochimica Acta 55.22 (2010): 6332-6341.
16. Peled, Emanuel. "The electrochemical behaviour of alkali and alkaline earth metals in nonaqueous battery systems—the solid electrolyte interphase model." Journal of The Electrochemical Society 126.12 (1979): 2047-2051.
17. Zaghib, Karim, Gabrielle Nadeau, and Kimio Kinoshita. "Effect of graphite particle size on irreversible capacity loss." Journal of the Electrochemical Society 147.6 (2000): 2110-2115.
18. Yazami, Rachid, and Yvan F. Reynier. "Mechanism of self-discharge in graphite–lithium anode." Electrochimica Acta 47.8 (2002): 1217-1223.
19. Novák, P., et al. "Advanced in situ methods for the characterization of practical electrodes in lithium-ion batteries." Journal of power sources 90.1 (2000): 52-58.
20. Ogihara, Nobuhiro, et al. "Disordered carbon negative electrode for electrochemical capacitors and high-rate batteries." Electrochimica acta 52.4 (2006): 1713-1720.
21. Park, Gumjae, et al. "The important role of additives for improved lithium ion battery safety." Journal of Power Sources 189.1 (2009): 602-606.
22. Edström, Kristina, Torbjörn Gustafsson, and John Oswald Thomas. "The cathode–electrolyte interface in the Li-ion battery." Electrochimica Acta 50.2 (2004): 397-403.
23. De Tacconi, N. R., Rajeshwar, K., & Lezna, R. O. (2003). Metal hexacyanoferrates: Electrosynthesis, in situ characterization, and applications. Chemistry of Materials, 15(16).
24. Wigley, P. W. R. (1959). Duncan and Wigley : The Electronic Structure of the Iron Atoms in Complex Iron Cyanides, (1120), 1120–1125.
25. M. Ware, "Prussian Blue: Artists' Pigment and Chemists' Sponge," Journal of Chemical Education, vol. 85, no. 5, p. 612, 2008.

26. M. Giorgetti, D. Tonelli, M. Berrettoni, G. Aquilanti, and M. Minicucci, “Copper hexacyanoferrate modified electrodes for hydrogen peroxide detection as studied by X-ray absorption spectroscopy,” J. Solid State Elec-trochem., vol. 18, no. 4, pp. 965–973, 2013.
27. M. Giorgetti, D. Tonelli, M. Berrettoni, G. Aquilanti, and M. Minicucci, “Copper hexacyanoferrate modified electrodes for hydrogen peroxide de-tection as studied by X-ray absorption spectroscopy,” J. Solid State Elec-trochem., vol. 18, no. 4, pp. 965–973, 2013.
28. H. Tokoro and S.-i. Ohkoshi, “Novel magnetic functionalities of Prussian blue analogs.,” Dalton transactions (Cambridge, England : 2003), vol. 40, no. 26, pp. 6825–6833, 2011.
29. J. Jiménez-Gallegos, J. Rodryguez-Hernàndez, H. Yee-Madeira, and E. Reguera, “Structure of porous copper prussian blue analogues: Nature of their high H2 storage capacity,” Journal of Physical Chemistry C, vol. 114, no. 11, pp. 5043–5048, 2010.
30. S. Liu, G. L. Pan, G. R. Li, and X. P. Gao, “Copper hexacyanoferrate nanoparticles as cathode material for aqueous Al-ion batteries,” J. Mater. Chem. A, vol. 3, no. 3, pp. 959–962, 2014.
31. J. P. Souza and D. R. Silvestrini, “Direct Preparation and Characterization of Copper Pentacyanonitrosylferrate Nanoparticles,” Journal of nanomaterials, vol. 2015, 2015.
32. A. B. Nikolskii, N. B. Batalova, and Y. I. Dyachenko, “Study of the nature of M-NO bond in nitroso complexes,” Teoeticheskaya i Eksperimental’naya Khimiya, vol. 15, no. 2, pp. 153–156, 1979.
33. Brown, “Nitrogen and Oxigen bonded Nitrosyl. Metal complexes of the nitroprusside ion.” Inorg. Chem., vol. 14, no. 10, pp. 2582–2584, 1975.
34. M. D. Carducci, M. R. Pressprich, and P. Coppens, “Diffraction studies of photoexcited crystals: Metastable nitrosyl-linkage isomers of sodium nitroprusside,” Journal of the American Chemical Society, vol. 119, no. 11.
35. P. Coppens, I. Novozhilova, and A. Kovalevsky, “Photoinduced linkage isomers of transition metal nitrosyl compounds and related complexes,” Chemical Reviews (Washington, D. C.), vol. 102, no. 4, pp. 861–883, 2002.

36. A. Gomez, J. Rodriguez-Hernandez, and E. Reguera, “Unique coordination in metal nitroprussides: The structure of $Cu[Fe(CN)_5NO]\cdot 2H_2O$ and $Cu[Fe(CN)_5NO]$,” J. Chem. Crystallogr., vol. 34, pp. 893–903, Dec. 2004.
37. A. C. de Sà, L. L. Paim, U. D. O. Bicalho, and D. R. do Carmo, “Determination of N-acetylcysteine by cyclic voltammetry using modified carbon paste electrode with copper nitroprusside adsorbed on the 3-aminopropylsilica,” International Journal of Electrochemical Science, vol. 6, no. 9, pp. 3754–3767, 2011.
38. Mullaliu, Angelo. Synthesis, characterization and formulation of a cathode active material: Copper nitroprusside. Diss.
39. Verma, Pallavi, Pascal Maire, and Petr Novák. "A review of the features and analyses of the solid electrolyte interphase in Li-ion batteries." Electrochimica Acta 55.22 (2010): 6332-6341.
40. Hesse, R., P. Streubel, and R. Szargan. "Improved accuracy of quantitative XPS analysis using predetermined spectrometer transmission functions with UNIFIT 2004." Surface and interface analysis 37.7 (2005): 589-607.
41. Seah, M. P. "XPS reference procedure for the accurate intensity calibration of electron spectrometers - results of a BCR intercomparison co-sponsored by the VAMAS SCA TWA." Surface and Interface Analysis 20.3 (1993): 243-266.
42. Yatsimirskii, K. B., et al. "Use of X-ray photoelectron and Mössbauer spectroscopies in the study of iron pentacyanide complexes." Journal of Electron Spectroscopy and Related Phenomena 10.3 (1977): 239-245.
43. Andersson, A. M., et al. "Surface characterization of electrodes from high power lithium-ion batteries." Journal of The Electrochemical Society 149.10 (2002): A1358-A1369.
44. Ensling, David, et al. "A comparative XPS surface study of Li2FeSiO4/C cycled with LiTFSI-and LiPF6-based electrolytes." Journal of Materials Chemistry 19.1 (2009): 82-88.
45. Burrell, Michael C., and John J. Chera. "Charge correction of the binding energy scale in XPS analysis of polymers using surface deposition of PDMS." Surface and interface analysis 27.9 (1999): 811-815.
46. Y. Nanba, D. Asakura, M. Okubo, H. Zhou, K. Amemiya, K. Okada, P.-A. Glans, C.A. Jenkins, E. Arenholz, J. Guo, Anisotropic charge-transfer effects in the asymmetric Fe(CN)5NO octahedron of sodium nitroprusside: a soft X-ray

absorption spectroscopy study., Phys. Chem. Chem. Phys. 16 (2014) 7031–7036. doi:10.1039/c3cp55471f.

47. Duraud, J. P., A. Le Moël, and C. Le Gressus. "Aging of fluoropolymers irradiated by X-Rays, low energy electrons and energetic heavy ions." *Radiation effects* 98.1-4 (1986): 151-157.
48. Andersson, Anna. “Surface phenomena in Li-ion batteries.” Diss. Acta Universitatis Upsaliensis, 2001.
49. Eriksson, Tom “LiMn2O4 as a Li-Ion Battery Cathode” Comprehensive Summaries of Uppsala Dissertations from the Faculty of Science and Technology 651. Acta Universitatis Upsaliensis, 2001.